Magnetic and Interatomic Forces Measured by Low Temperature Scanning Force Microscopy

Inauguraldissertation

zur

Erlangung der Würde eines Doktors der Philosophie

vorgelegt der

Philosophisch-Naturwissenschaftlichen Fakultät

der Universität Basel

von

Regina Hoffmann

aus Karlsruhe (Deutschland)

Basel, 2001

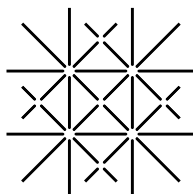

UNI
BASEL

Genehmigt von der Philosophisch-Naturwissenschaftlichen Fakultät
auf Antrag der Herren Professoren:

Prof. Dr. H.-J. Güntherodt
Prof. Dr. H. J. Hug
Prof. Dr. E. Meyer

Basel, den 20. November 2001

Prof. Dr. A. Zuberbühler, Dekan

Contents

1 **Introduction** 1
1.1 Outline of the thesis . . . 3

2 **Introduction to Scanning Force Microscopy** 5
2.1 The scanning force microscopes . . . 6
2.2 Ultra-high vacuum system . . . 7
2.3 Cantilever . . . 9
2.4 Dynamic SFM mode . . . 10
2.4.1 The equation of motion of the cantilever . . . 10
2.4.2 Conversion of frequency shift to force . . . 11
2.4.3 Frequency demodulation technique . . . 12
2.4.4 Non-conservative tip-sample interactions . . . 12
2.5 Detection electronics . . . 13
2.5.1 RTSFM Electronics . . . 13
2.5.2 LTSFM Electronics - PLL . . . 14
2.6 Forces . . . 15
2.6.1 Distance dependence of conservative forces . . . 16
2.6.2 Mechanisms of energy dissipation in dynamic mode SFM . . . 19
2.7 Magnetic contrast formation . . . 20
2.7.1 Contrast mechanisms and force acting on the tip . . . 21
2.7.2 The tip equivalent magnetic charge distribution . . . 21
2.7.3 The stray field of a perpendicularly magnetized sample . . . 22
2.7.4 Conversion of frequency shift to force . . . 23
2.7.5 Distance dependence of the frequency shift . . . 24

3 **Magnetic domains of a thin Ag/Fe/Ag film** 25
3.1 Introduction . . . 25
3.2 Tip and sample preparation . . . 26
3.3 Magnetic Force Microscopy images . . . 28
3.4 Analysis of the domain size . . . 29
3.5 Analysis of the domain shape . . . 30
3.6 Conclusions . . . 31

4 **Quantitative magnetic force microscopy** 33
4.1 Introduction . . . 33
4.2 Tip and sample preparation . . . 34

4.2.1 Tip preparation 34
4.2.2 Calibration procedure and choice of the test sample 35
4.3 Calibration of ultralow strayfield tips 37
4.3.1 Iron coated tips 37
4.3.2 Comparison of tip equivalent charge distributions obtained using different image sizes and using images obtained on different test samples 41
4.3.3 Nickel coated tips 43
4.3.4 Conclusions 47
4.4 Ultrasharp tips 47
4.4.1 Calibration of an ultrasharp tip and comparison to a Nanosensor tip . . . 48
4.4.2 Conclusions 52
4.5 Signal to noise ratio as a function of oscillation amplitude 53
4.5.1 MFM images acquired at different oscillation amplitudes 54
4.5.2 Evaluation of the noise 55
4.5.3 Evaluation of the signal to noise ratio 55
4.6 Conclusions 56

5 Atomic resolution imaging on KBr **57**
5.1 Introduction 57
5.2 Tip and sample preparation 58
5.3 Large scale images 58
5.4 Atomic resolution images 58
5.4.1 Constant frequency shift contours 58
5.4.2 Tip instabilities 59
5.4.3 Energy dissipation 60
5.5 Frequency versus distance measurements 62
5.5.1 Analysis of the frequency versus distance data 63
5.5.2 Short-range forces 64
5.5.3 Conclusions 65
5.6 Atomistic simulations of the KBr (001) surface 66
5.6.1 Simulation program, tip and sample models 66
5.6.2 Force versus distance and relaxation versus distance data 68
5.6.3 Frequency versus distance data 70
5.6.4 Constant frequency shift images 73
5.6.5 Conclusions 75
5.7 A point defect on the KBr (001) surface 76
5.7.1 Atomic resolution image of an atomic scale defect on KBr (001) 76
5.7.2 Conclusions 78
5.8 Water on KBr (001) 79
5.9 Conclusions 79

6 Atomic resolution imaging on NiO **81**
6.1 Introduction 81
6.2 Antiferromagnetic materials and magnetic imaging 82
6.2.1 Antiferromagnets 82

6.2.2 Overview of the literature on atomic scale imaging of antiferromagnetic samples . . . 82
6.2.3 The antiferromagnetic structure of NiO . . . 83
6.3 Tip and sample preparation . . . 84
6.4 Large scale images . . . 84
6.5 Atomic resolution images . . . 86
6.6 Tip instability . . . 87
6.7 Frequency versus distance measurements . . . 87
6.7.1 Analysis of the frequency versus distance data . . . 88
6.7.2 Short-range forces . . . 90
6.8 Energy dissipation . . . 91
6.9 An atomic scale defect . . . 93
6.10 Conclusions . . . 93

7 General conclusions 95
7.1 MFM measurements on Ag/Fe/Ag sandwiches . . . 95
7.2 Quantitative Magnetic Force Microscopy . . . 95
7.3 Atomic resolution measurements on KBr . . . 96
7.4 Atomic resolution measurements on NiO . . . 97

A Magnetic contrast formation 99
A.1 Definition of the scalar magnetic potential and related quantities . . . 99
A.2 The stray field of a magnetic sample . . . 99
A.3 The tip equivalent charge distribution . . . 100
A.4 Conversion of frequency shift to force . . . 101

Bibliography 111

Publications 114

Curriculum Vitae 116

Acknowledgements 118

Zusammenfassung 121

Abstract 123

List of Figures

2.1 Principle of the scanning force microscopes used in this thesis 5
2.2 Photograph of the SFM used in this thesis 6
2.3 Overview of the UHV system containing the LTSFM 7
2.4 Sideview of the cryostat 8
2.5 Resonance curve of a cantilever 10
2.6 Schematic overview of the dynamic SFM setup 13
2.7 Details of the electronic system used for FM-detection and cantilever excitation in the RTSFM 14
2.8 Details of the electronic system used for home-built FM-detection, cantilever excitation and z control in the LTSFM 15
2.9 Tip model used for describing the van-der-Waals and electrostatic forces 17
2.10 Image interaction on insulating surfaces 17
2.11 Tip models used to describe magnetic tips 22
2.12 Determination of the sample stray field from a MFM measurement 23

3.1 MFM images of magnetic domains for different Fe thicknesses on a Ag/Fe/Ag sandwich 28
3.2 Domain size as a function of the Fe film thickness on the Ag/Fe/Ag sandwich . . 30

4.1 Sketch of the evaporation direction of the magnetic layer deposited on the tip . . 34
4.2 Sketch of the charge distribution for a pyramidal Nanosensor 35
4.3 Determination of the sample stray field from a MFM measurement 36
4.4 SEM image of a Nanosensor tip 37
4.5 Images obtained with Nanosensor tips coated with Fe 38
4.6 σ_{tip} of Fe coated tips 39
4.7 Magnetic field distribution of the tip Fe-2.2 40
4.8 Magnetic field generated by the Fe coated tips 41
4.9 σ_{tip} obtained on different samples and with different image sizes 42
4.10 Images acquired with Nanosensor tips coated with Ni 44
4.11 The spectra of an Fe coated tip and two Ni coated tips as a function of the tip-sample distance. 45
4.12 σ_{tip} for a Ni coated tip 46
4.13 Magnetic field distribution of tip Ni-9.6 47
4.14 SEM image of an ultrasharp tip 48
4.15 Comparison of images obtained with an ultrasharp tip and with a Nanosensor tip 49
4.16 σ_{tip} of the ultrasharp tip 50
4.17 Model of a magnetic monopole tip 50

4.18 Images obtained with an ultrasharp tip compared with simulated images using a monopole model 52
4.19 Magnetic field distribution for the ultrasharp tip 53
4.20 Images obtained with an ultrasharp tip for different oscillation amplitudes 54
4.21 Noise as a function of the amplitude 55
4.22 Signal to noise ratio for different oscillation amplitudes as a function of k-vector 56

5.1 Large scale image of a freshly cleaved KBr surface 58
5.2 Atomic resolution image of a KBr surface 59
5.3 Atomic resolution image of a KBr surface with a tip change 60
5.4 Dissipated energy shown together with the corresponding topographic atomic resolution images 61
5.5 Image before the frequency versus distance measurements 62
5.6 Long-range frequency shift on a KBr surface and force obtained after conversion 63
5.7 Short-range frequency shift on a KBr surface and force obtained after conversion 64
5.8 Tip and sample model used for the atomistic simulations 67
5.9 Positions where the force versus distance data were calculated 68
5.10 Force versus distance data calculated for the K^+- and the Br^--terminated tip above three atomic sites 69
5.11 Relaxation of the frontmost tip atom for the Br^- and K^+-terminated tip above three different sites. 70
5.12 Comparison of measured frequency shifts with calculated ones 71
5.13 SFM images calculated from the force versus distance data 74
5.14 Images of an atomic scale defect on KBr 77
5.15 Averaged image of the KBr surface excluding the defect and difference of the averaged image and the defective unit cell 78
5.16 Large-scale and atomic-resolution images for a cleaved KBr crystal covered with water 80

6.1 Sketch of the full magnetic unit cell of the NiO crystal 83
6.2 Large scale image of a NiO crystal that has not been annealed 85
6.3 Bias dependence of a large scale image on NiO 85
6.4 Images obtained on the NiO crystal before and after measuring frequency versus distance data 86
6.5 Long-range frequency and force versus distance data on NiO 88
6.6 Short-range frequency and force versus distance data on NiO 89
6.7 Dissipated energy per oscillation cycle on NiO 92
6.8 Dissipated energy per oscillation cycle versus distance measurements 92
6.9 Defect observed on the NiO surface 93

List of Tables

2.1 Properties of the cantilever used in this thesis 10

4.1 Nanosensor tips coated with Fe 38
4.2 Nanosensor tips coated with Ni 43
4.3 Magnetic properties of all Ni coated tips 45
4.4 Ultrasharp tips coated with Fe 48
4.5 Comparison of the imaging properties of all calibrated tips 56

5.1 Parameters used for the calculation of the force on KBr 67
5.2 Possible defects in ionic crystals of the NaCl type 75

6.1 Possible directions of the spins within one T-domain in NiO 84

List of Symbols

a_{KBr}	K^+ Br^- distance
A_{exc}	excitation amplitude
A_{max}	oscillation amplitude of the cantilever at resonance
A, A_{osc}	measured cantilever oscillation amplitude
b	bandwidth
$\vec{B}$	magnetic flux density
c_L	cantilever longitudinal spring constant
c_{pol}	spring constant associated with the polarizability of an ion
$c(\theta)$	$c(\theta) = 1/\ln(\cot(\theta/2))$ function of the tip opening angle θ
C_H	Hamaker constant
C_1, C_2, C_3	constants used for the Buckingham potential
C_{exc}	magnetic exchange constant
C_{pattern}	constant used to describe the domain size that depends only on the domain pattern
d_{lever}	cantilever thickness
$d_{\mathrm{film,\ nom}}$	nominal magnetic film thickness
$d_{\mathrm{film,\ Quartz}}$	film thickness deposited on the quartz microbalance during evaporation
d_{Fe}	iron film thickness
D	domain size
e	electron charge
E	Young's modulus
$\vec{E}$	electric field strength
f_0	unperturbed resonance frequency of the cantilever
Δf	measured frequency shift
δf_{rms}	thermal frequency noise
$\vec{f}$	an arbitrary function
$\vec{F}$	interaction force
F_n	interaction force component in direction of the cantilever canting
F_{exc}	driving force of the cantilever
F_{el}	capacitive interaction force
F_{vdW}	van-der-Waals force
$\vec{H}$	magnetic field strength
$I_n(z)$	Bessel function
$\vec{k}$	$\vec{k} = (k_x, k_y, k_z)$, $k = \lvert\vec{k}\rvert = 2\pi/\lambda$ wave vector
$\vec{k}_{\parallel}$	$k_{\parallel} = (k_x, k_y)$ in plane component of the wave vector

k_B	Boltzmann's constant
K_u	total magnetic anisotropy
K_{V}	volume magnetic anisotropy
K_{S}	surface magnetic anisotropy
l_{tip}	tip length
l_{lever}	cantilever length
l_{dipolar}	$l_{\mathrm{dipolar}} = \sigma_{\mathrm{W}}/(1/2\mu_0 M_S^2)$ magnetic dipolar length
m_{eff}	effective mass of the cantilever
$\vec{M}$	magnetization
M_S	saturation magnetization
$\vec{n}$	direction of the cantilever canting
$\vec{P}$	electric polarization of the sample
$\vec{p}$	polarization of an ion
$q_{\mathrm{M,\ tip}}$	magnetic charge of a monopole tip
Q	quality factor of the cantilever
Q_{shell}	shell charge used for the simulation program
r	distance, absolute value of $\vec{x}$
r_0	characteristic distance for the Buckingham potential
R	tip radius
$\vec{S}$	spin direction
t	time
T	temperature
u	complex number
$U_{\mathrm{tip/sample}}$	interaction potential
U_{B}	Buckingham potential
$V_{\mathrm{tip}}, V_{\mathrm{sample}}$	tip and sample volume
ΔV	voltage between tip and sample
w_{lever}	cantilever width
$\vec{x}$	position
$x,\ y,\ z$	components of $\vec{x}$
x_n	component of $\vec{x}$ in the direction of the cantilever canting, $\vec{n}$

α	tip opening angle
α_{pol}	polarizability of an ion
β	azimuth describing the orientation of a pyramidal facet of a Nanosensor tip
γ	damping coefficient for velocity dependent damping
γ_0	intrinsic damping coefficient of the cantilever
Γ	$\Gamma = \Delta f c_L A_{\mathrm{osc}}^{3/2}/f_0$ normalized frequency shift
θ	evaporation direction
$\Theta(\omega \to 0)$	$\Theta(\omega \to 0) = N(\omega)/\omega^2$, $N(\omega)$ phonon density of states
λ	wavelength
ρ_{mass}	mass density of the cantilever material
$\rho_{\mathrm{resistivity}}$	electrical resistivity of the sample
ρ_{M}	magnetic charge density

σ_{M}	magnetic surface charge density
σ_{tip}	magnetic surface charge density generating a field equivalent to the tip field
σ_{W}	domain wall energy per unit of surface area
φ	phase of the cantilever oscillation
Φ	magnetic scalar potential
ω	$\omega = 2\pi f$ angular frequency

Chapter 1

Introduction

Today, smaller and smaller magnetic structures are extensively studied both from an applied and from a fundamental point of view. The need for larger capacities of magnetic data storage devices at a constant price creates demand for research on small magnetic structures. The magnetic storage media as well as the read and write techniques need to be constantly improved in order to achieve an exponential decrease of the bit size by about 30 % in only two years. Magnetic storage media are granular materials with grain sizes on the order of one nanometer. One important limitation of the bit size today is the superparamagnetic limit. As the bit size decreases, the number of grains per bit decreases if their diameter remains constant. Thus, in order to improve the signal to noise ratio during read-out, the grain size has to be decreased, too. However, as the grain size becomes smaller, the anisotropy energy of a single grain approaches the thermal energy and the information stored can be lost. Research is now focussing on ways to overcome this superparamagnetic limit. As the bit size is decreased, also the techniques used for writing and reading the information need to be improved. The discovery of the giant magnetoresistance effect has helped to improve read and write heads and to accelerate the growth of data capacity. However, a technique capable of measuring local magnetic fields on the nanometer scale in a quantitative way is needed to further improve the storage media as well as read and write heads. A fundamental limit of the size of a bit is certainly reached, when the bit size approaches the size of an atom. Alternating magnetic moments on neighbouring atoms are realized in antiferromagnets. The antiferromagnetic order is determined by the exchange coupling between the spins. Experimental methods to study the exchange coupling between spins as a function of their distance are needed.
Fundamental research on small magnetic structures provides important background information needed to improve magnetic data storage. Magnetic domains of submicron size occur in thin magnetic films with perpendicular magnetization made from elements, for example Cobalt [1], magnetic alloys, such as CoPt or FePd [2] and thin film sandwiches with interface anisotropy, for example Cu/Ni/Cu [3] or Ag/Fe/Ag. The contribution of surface and interface atoms to the magnetism strongly influences the magnetic properties of a thin film, for example changing its direction of magnetization from in the sample plane to out of the sample plane. Giant magnetic moments have been observed in Rhodium clusters containing 12 to 32 atoms [4]. Recently, the strong influence of edge ions on the properties of magnetic clusters of Co deposited on a Pt(111) surface have been studied by X-ray magnetic circular dichroism [5]. Magnetic moments of single atoms or ions are known to be much larger than those of solids. One of the main questions is therefore how the magnetism of small objects changes with size, finding a link between the atom

and the solid.

From both the applied and the fundamental point of view, techniques to characterize the magnetic properties locally are important. The first technique capable of resolving local magnetic patterns, and therefore proving that magnetic domains do exist, was the Bitter technique [6]. With a magnetic fluid or powder, magnetic structures are decorated and the structures in the powder or fluid created by the magnetic field are imaged by a conventional microcopy technique. Magneto-optical Kerr effect imaging is a technique limited in resolution by the wavelength of the laser light. Scanning electron microscopy with polarization analysis (SEMPA) is able to resolve magnetic domains up to submicron resolution [7, 8], but for better resolution, high acceleration energies and large instruments are needed. These two techniques allow a reconstruction of the full magnetization vector. Atomic size magnetic structures can be analysed if they are repeated periodically in a crystal by diffraction techniques such as neutron diffraction. Neutron diffraction has been particularly successful in resolving the magnetic structures of antiferromagnetic materials. This technique can also be used for imaging [9], but in this case a high neutron flux is needed that can only be supplied by expensive and large nuclear reactors.

Alternative local magnetic characterization techniques are based on scanning probe microscopy. In scanning force microscopy, the interaction between a sample surface and a microscopic tip is measured during fine scanning of the probe, mostly by use of a piezo-electric material. The field of scanning probe microscopy (SPM) was opened with the invention of the scanning tunnelling microscope (STM) by G. Binnig et al. in 1982 [10]. Since then, many other representatives of the SPM-family have been developed. Today, mainly two magnetic characterization techniques based on scanning probe microscopy are used: magnetic force microscopy (MFM) and spin polarized scanning tunnelling microscopy (STM). This thesis focusses on magnetic force microscopy which is based on one of the most versatile instruments of the scanning probe family, the scanning force microscope (SFM). The SFM was invented by G. Binnig et al. in 1986 [11]. A microscopic flexible cantilever is approached carefully to the surface of the sample, and its deflection by the forces near the surface is measured. True atomic resolution of the silicon (111) 7×7 surface has first been achieved with a SFM in 1995 by Giessibl et al. [12]. True atomic resolution on insulating ionic crystals has first been achieved in 1997 by Bammerlin et al. [13]. The imaging mechanism and the tip to sample interaction on these surfaces are intensively studied today. In this thesis, atomically resolved images, frequency measurements as a function of the tip to sample distance and atomistic simulations of the tip sample interaction on KBr are shown. The SFM cantilever can be made sensitive to various kinds of forces by a coating specific to this force and the technique can be used in various environments such as the ambient, fluids, ultra high vacuum (UHV), high pressure, high and low temperatures, magnetic or electrostatic fields and others.

Shortly after the first demonstration of the SFM by Binnig et al. it has been used to map the magnetic stray field emanating from a ferromagnetic sample [14, 15]. For that purpose, the tip is made sensitive to magnetic stray fields either by making the tip from a ferromagnetic material or by coating the non-ferromagnetic tip with a thin ferromagnetic film. The development of the MFM has made it possible to image magnetic domains of sub-micron size in various materials in the following years by applying a technique of the SPM-family. Magnetic domains in magnetic recording media, ultrathin films and wires are widely studied today by MFM. In this thesis, the domains of an Ag/Fe/Ag film have been studied as a function of the Fe film thickness. These first results, obtained by an MFM, have created a need for a better understanding of the interaction of the magnetic tip with the stray field produced by the sample. Recently, quantitative magnetic force microscopy (QMFM), a method how to measure magnetic fields in a quantitative way, has

been proposed [16]. This method is applied in this thesis to characterize MFM tips prepared by evaporation of a magnetic film of varying film thickness and material on several types of SFM tips made out of Silicon.
However, magnetic imaging on the atomic scale remains a challenge for the SFM as well as the spin polarized STM. Antiferromagnetic metallic elements, Cr and α-Mn, have been studied by spin polarized STM. The Cr(001) surface shows a ferromagnetic arrangement of the moments within one Cr terrace, but an antiferromagnetic arrangement of the moments on alternating terraces. The antiferromagnetic contrast across steps on a thin Cr(001) film deposited on Fe(001) has been studied by spin-polarized STM [17]. Recently, antiferromagnetic Manganese has been stabilized on a W(110) surface and a variation of magnetic moments has been measured on the atomic scale by spin-polarized STM [18].
On antiferromagnetic materials, short range magnetic forces, the exchange forces, are expected to be of a measurable magnitude [19, 20]. Attempts by several groups to measure an atomic scale magnetic contrast on an antiferromagnetic insulator, NiO, by SFM have not been successful to date [21, 22]. This thesis will discuss possible reasons for this failure.

1.1 Outline of the thesis

The thesis is organized in the following way: first, a short introduction to scanning force microscopy is given. In the second chapter, a study of the shape and size of the magnetic domains of a Ag/Fe/Ag wedge shaped sample as a function of film thickness is presented. In the third chapter, our efforts to optimize magnetic force microscope tips for lateral resolution and for the measurement of samples with a low coercive field are summarized.
The fourth chapter deals with results obtained in the regime of short range forces on a non-magnetic sample (KBr) with true atomic resolution. The first site-specific force versus distance measurements on an insulating sample are compared with the results of a simulation. In the fifth chapter, atomic resolution measurements on NiO and first experiments towards the measurement of exchange forces are shown.

Chapter 2

Introduction to Scanning Force Microscopy

In a scanning force microscope (SFM), the force between a microscopic tip and a surface is measured as a function of the position of the tip relative to the sample. For this purpose, the tip is attached to a cantilever, and the deflection of this cantilever of known longitudinal force constant is measured. The lateral position of the tip relative to the sample can be scanned to produce an image of the surface. In addition, the vertical position can be changed to measure the force as a function of the distance to the sample (figure 2.1).

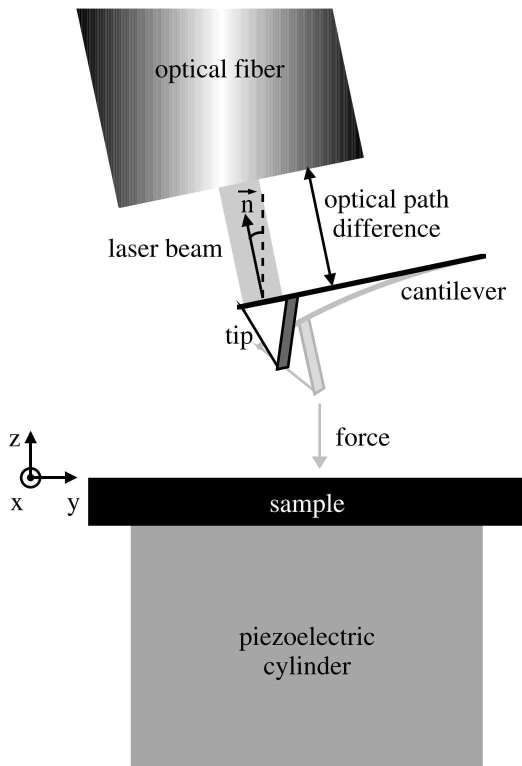

Figure 2.1: Principle of the scanning force microscopes used in this thesis: The cantilever deflection caused by interaction of the tip with the sample is measured by an interferometer. The sample is scanned using a piezo-electric cylinder. In this thesis, z is the direction perpendicular to the sample, x and y lie in the sample plane. The cantilever is tilted with respect to the sample by 12° in our instrument, such that the direction $\vec{n}$ is not parallel to the z-direction.

In this thesis two SFMs were used. One is a low temperature SFM (LTSFM) operating in ultra-high-vacuum (UHV) and the other one is its prototype, operating at room temperature and

in high vacuum (called RTSFM). The design of the two instruments is similar. The RTSFM was used for the measurements shown in chapters 3 and 4 and the LTSFM was used for the measurements shown in chapters 5 and 6. The LTSFM used in this thesis has been described in detail in references [23] and [24].
For moving precisely small distances, in our instruments, the sample is scanned by applying a voltage to a piezo-electric cylinder. As the motion of this cylinder is a nonlinear function of the applied voltage, and depends on temperature, the scanner was carefully calibrated and linearized at different temperatures [23, 24]. The measurements shown in chapters 5 and 6 were done at 8 K. The deflection of the cantilever is detected by an interferometric system. A laser beam is conducted by an optical fiber to the vicinity of the cantilever backside. It is reflected from this surface and an interference evolves inside the optical fiber between the beam reflected from the cantilever and the one reflected from the fiber end. An additional piezo-cylinder is used to adjust the fiber-cantilever distance to be at the point most sensitive to changes of the cantilever position.

2.1 The scanning force microscopes

A photograph of the LTSFM used in this thesis is given in figure 2.2. The macroscopic position on the sample as well as the macroscopic distance to the sample surface can be changed using a coarse approach motor. The sample (tip) is mounted on a sample (tip) holder that can be moved in and out of a precision positioning sample stage. This allows in situ tip and sample change (for the LTSFM).

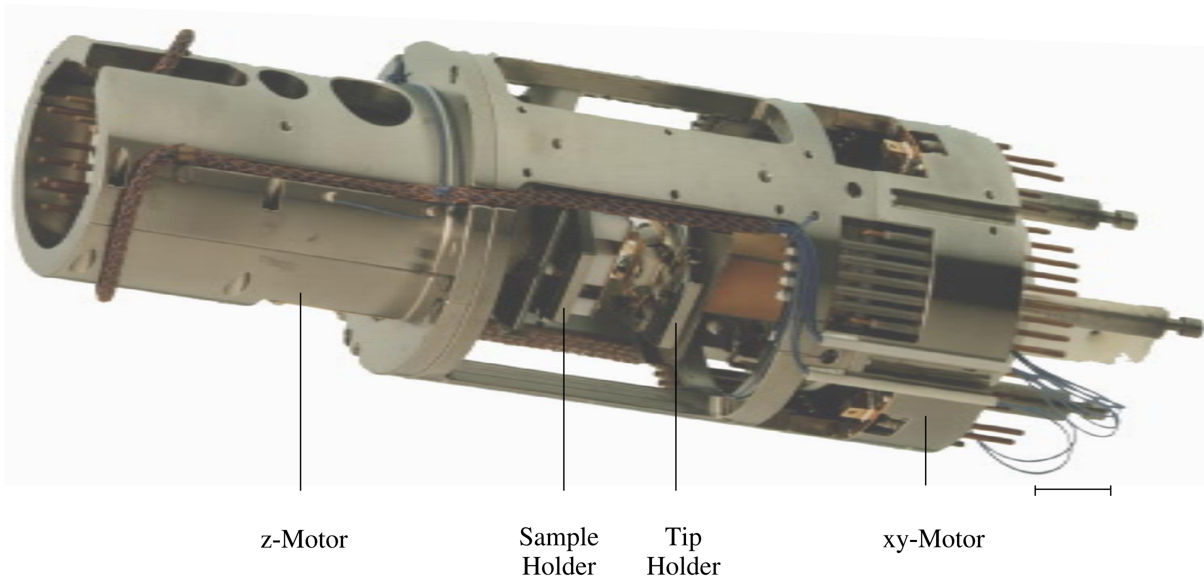

Figure 2.2: Photograph of the SFM used in this thesis.

During the design of the microscope, special care has been taken to avoid drift problems when large temperature changes are applied to the microscope. Lateral drift can be significantly reduced by a symmetric instrument design. Vertical drift is reduced by choosing materials for the body and parts that have a similar thermal expansion coefficient. The instrument is stable

enough to allow imaging an area of 3 nm $\times$ 3 nm for several hours with negligible drift. It also allows to move the tip to one position on the sample surface selected from an atomic scale image and to perform a vertical scan precisely above this position and thus obtain site-specific information.
The choice of materials was further restricted by the requirement that the microscope should support high magnetic fields. No ferromagnetic materials were used for the construction of the microscope. Applying a magnetic field to the microscope makes it possible to magnetize the tip or to perform measurements on magnetic samples during the hysteresis cycle. During all measurements shown in this thesis, no magnetic field was applied.
Cantilever, sample and the gold-coated optical fiber are electrically isolated from one another and from the UHV system. A voltage can be applied separately to each of the three. Moreover, the sample has four independent electrical connections. In this thesis, only one connection to the sample was used to minimize the electrostatic forces on insulating surfaces in chapters 5 and 6.

2.2 Ultra-high vacuum system

The LTSFM is build into a UHV system. An overview of the UHV system is shown in figure 2.3. It consists of two chambers - the microscope chamber consisting of the microscope, the sample exchange chamber, the cryostat and the feedthrough chamber (top chamber). The second chamber serves for preparation and surface analysis of tips and samples and is called preparation chamber. It is connected to a fast entry air lock. A transport system links the two chambers.

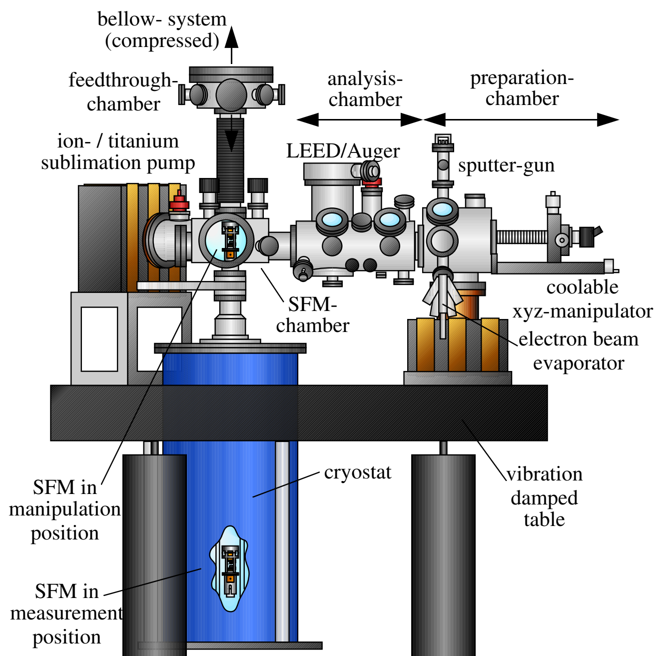

Figure 2.3: Overview of the UHV system containing the LTSFM. The fast entry air lock mentioned in the text is behind the preparation chamber in this view.

The UHV system is built on an active damping table to isolate it from floor and building vibrations. During measurements, the system is only pumped by ion pumps in order to avoid vibrations and electrical noise induced by turbo pumps.

Microscope chamber

The microscope is connected via a steel insert to the top chamber (figure 2.3). By moving the top chamber up and down, the microscope can be moved from the position where the tip and the sample can be changed, to the measurement position inside the cryostat. In the first position, tip and sample can be transferred from the transport system into the microscope with the help of a mechanical hand. In the second position, the measurement position, a cone mounted on the insert touches a hollow cone inside the cryostat to form a heat flow connection for cooling the microscope. After tip or sample exchange, the microscope is cooled during one hour until it reaches a stable temperature of 8 K. An eddy current damping system filters any vibrations transmitted to the insert.

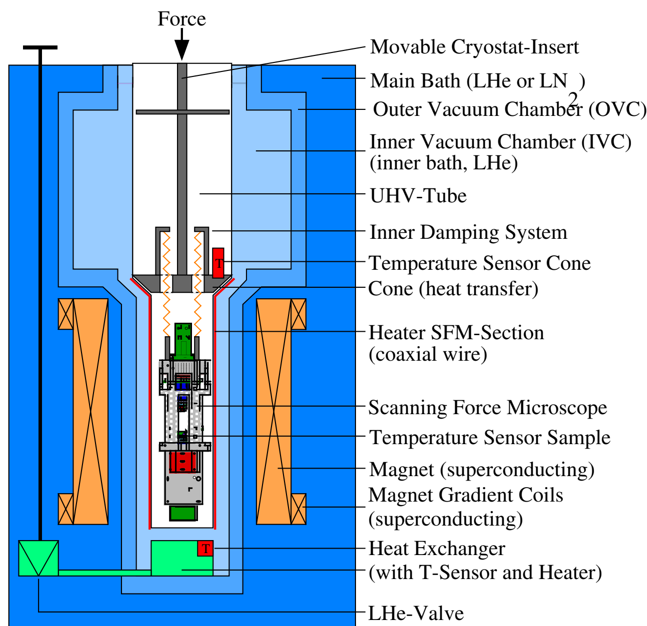

Figure 2.4: Sideview of the cryostat.

The cryostat is a variable temperature bath cryostat (figure 2.4). It can be operated in various modes, but here only the one mainly used in this thesis will be described. The cryostat contains a main bath that is filled with liquid Helium, an outer vacuum chamber (OVC), and an inner vacuum chamber (IVC), adjacent to the UHV tube. From the main bath, liquid helium is transferred through a capillary and a needle valve into the IVC. A pump is directly connected to the IVC in order to adiabatically expand the liquid Helium at the point where it leaves the capillary, the heat exchanger, and thus lower its temperature below the boiling point at room pressure, 4.2 K. In this operation mode, a temperature of 1.7 K can be reached at the heat exchanger and, if the gas pressure in the IVC is about 10 mbar, about 6 K are reached at the position of the sample in the microscope. The temperature at the position of the sample is controlled to a precision of more than 1 mK by an analogue feed back loop in order to avoid influences of temperature changes on the SFM measurements. The cryostat contains a superconducting magnet that produces magnetic fields of up to 7 T in the perpendicular direction. Cooling down the cryostat including the magnet from room temperature takes about one day. The cryostat consumes about 20 l of liquid Helium in 24 hours; the main bath contains about 36 l of liquid Helium.

Preparation chamber

The preparation chamber contains a heatable and coolable stage where the tip and sample holders can be inserted. By flowing liquid nitrogen through a capillary attached to the preparation stage the tip or sample can be cooled while it is in the preparation stage. Tips and samples can be heated in this stage in three different ways: with a heater element included in this preparation head or a heatable sample holder containing a heater element or by direct current heating. With the last method, Silicon can be heated to 1300° C. In this stage, several surface preparation techniques can be applied to a sample or to a tip: thin films can be prepared with an electron beam evaporator. This electron beam evaporator was used to prepare the magnetic tips shown in chapters 3 and 4. The film thickness can be monitored with a quartz microbalance thickness monitor. A sputter gun can be used to clean the tip or sample and a crystal sample can be cleaved by a crystal cleaver. In this thesis, the KBr and NiO single crystals were cleaved with this crystal cleaver and heated using the heater element located in the preparation head in order to remove charge resulting from the cleavage process.
In another position in the same chamber, accessible via the transport system and a mechanical hand, LEED (low energy electron diffraction) and Auger analysis can be applied for surface analysis.

2.3 Cantilever

The sensor used in our SFM is a microfabricated tip attached to a cantilever. The sensitivity of the static cantilever to an applied force is given by its longitudinal spring constant, c_L, as Hooke's law applies for deflections small compared to the cantilever length:

$$F_n = c_L \Delta x_n \qquad \text{where} \qquad F_n = \vec{n}\vec{F} \qquad \text{and} \qquad \Delta x_n = \vec{n}(\vec{x} - \vec{x}_0) \tag{2.1}$$

where $\vec{n}$ is a unit vector along the easy deflection direction (see figure 2.1), Δx_n is the position of the tip apex relative to the equilibrium position in the absence of interactions, $\vec{x}_0$. The smaller the longitudinal spring constant, the larger the cantilever deflection for a given force. The longitudinal force constant of the cantilever can be calculated from its dimensions (width w_{lever}, thickness d_{lever} and length l_{lever}) and from its Young's modulus, E:

$$c_L = \frac{E w_{\text{lever}} d_{\text{lever}}^3}{4 l_{\text{lever}}^3} \tag{2.2}$$

Therefore the cantilever dimensions can be designed to provide a certain force constant. The fundamental resonance frequency of the cantilever is given by [25]:

$$f_0 = \frac{1.873^2 d_{\text{lever}}}{4\sqrt{3}\,\pi l_{\text{lever}}^2} \sqrt{\frac{E}{\rho_{\text{mass}}}} \tag{2.3}$$

Here, ρ_{mass} denotes the density of the cantilever material.
In this thesis, four different types of cantilevers are used (table 2.1). They can be divided in two groups - soft cantilevers for sensitive measurements of weak long-range magnetic forces (chapters 3 and 4) and hard cantilevers to avoid a snap to surface during the measurement of strong short-range chemical forces (chapters 5 and 6). The cantilevers are made from doped silicon or silicon nitride. The doping is high enough that the cantilevers are still conducting at

name	material	doping [Ωcm]	c_L [N/m]	f_0 [kHz]	l_{lever} [μm]	w_{lever} [μm]	d_{lever} [μm]	chapter
microlevers (Park Sci. Instr.)	SiN_x		0.03	16.5		triangular		3
contact mode (Nanosensors)	Si	n-type 0.01-0.02	0.2	13	439	48	2.13	4
ultrasharp (Team Nanotec)	Si	n-type 0.01-0.5	2	81	230	32	2.3	4
non-contact mode (Nanosensors)	Si	n-type 0.01-0.02	40	175	223	34	6.9	5 and 6

Table 2.1: Properties of the cantilevers used in this thesis. For Si $E = 1.25 \cdot 10^{11}\text{N/m}^2$ and $\rho_{\text{mass}} = 2.33 \cdot 10^3\text{kg/m}^3$ [26].

low temperatures. However, when initially introduced into vacuum, they are covered with native oxide. This oxide has insulating properties. The details of their preparation will be described in the chapters in which they are used.

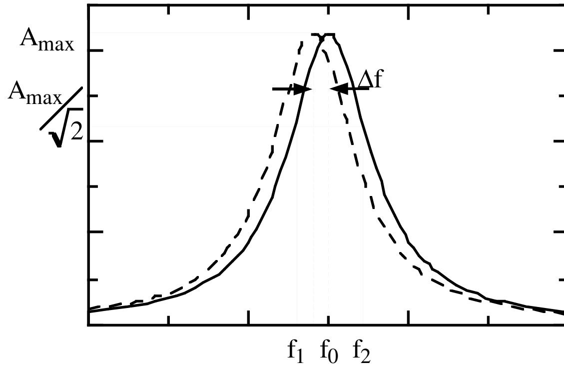

Figure 2.5: Resonance curve of a cantilever, change in resonance frequency induced by the surface force.

2.4 Dynamic SFM mode

2.4.1 The equation of motion of the cantilever

The SFMs used in this thesis are well suited for various operation modes. As all measurements shown in this thesis were done in dynamic modes, only this mode is described here. In this mode the cantilever is excited by the oscillation of a small piezo actuator mounted directly under the cantilever on its holder. The equation of motion of the driven oscillation is:

$$c_L x_n(t) + \gamma_0 \dot{x}_n(t) + m_{\text{eff}} \ddot{x}_n(t) = F_n(\vec{x}) + F_{\text{exc}} \cos(\omega t) \qquad (2.4)$$

where $f_0 = 1/2\pi\sqrt{c_L/m_{\text{eff}}}$ is the resonance frequency of the unperturbed cantilever, equation 2.3 defines its effective mass, m_{eff}, F_{exc} is the driving force and $F_n(\vec{x})$ is the interaction force to be measured. γ_0 is the damping coefficient of the free cantilever related to its quality factor Q_0 and to the width of the resonance curve (see figure 2.5)

$$Q_0 := \frac{2\pi f_0}{\gamma_0} \approx \frac{f_0}{|f_1 - f_2|} \qquad (2.5)$$

At resonance, the energy dissipation per oscillation cycle is E_0/Q_0, where $E_0 = 1/2c_L A_{\max}^2$ is the energy stored in the oscillating cantilever and $A_{\max}$ is the oscillation amplitude.
Furthermore, the excitation amplitude, $A_{\text{exc}} = F_{\text{exc}}/c_L$, becomes equal to

$$A_{\text{exc}} = \frac{A_{\max}}{Q} \tag{2.6}$$

at resonance.

2.4.2 Conversion of frequency shift to force

The resonance frequency of the oscillator changes under the influence of the interaction force to be measured (figure 2.5). In the case of a weak conservative perturbation, the change of the resonance frequency is given by [27]:

$$f - f_0 = \Delta f = -\frac{f_0}{2\pi c_L A_{\text{osc}}} \int_{-\pi}^{\pi} F_n(\vec{x}(\varphi)) \cos\varphi d\varphi \quad \text{where} \quad \vec{x} = \vec{x}_0 + \vec{n} \cdot A_{\text{osc}} \cos\varphi \tag{2.7}$$

where $\vec{x}_0$ is the time-averaged tip apex position and A_{osc} is the tip oscillation amplitude and $\varphi = \omega t$ [27]. In the small amplitude limit (neglecting the cantilever canting)

$$f = \frac{1}{2\pi}\sqrt{\frac{c_L - F'(z)}{m_{\text{eff}}}} = f_0\sqrt{1 - F'(z)/c_L} \approx f_0(1 - \frac{1}{2c_L}F'(z)) \tag{2.8}$$

The quantity $f_0/2c_L$ will in the following be called force sensitivity.
Equation 2.8 is only valid if the force can be approximated by a linear function in the region where the integration is performed. However, the amplitudes used in this thesis rarely fulfil the small amplitude approximation. The reason is that the spring constant, c_L, is small compared to the stiffness of chemical bonding forces, and that therefore a snap to the surface can in principle occur. Such a snap to contact can cause severe damage of the tip; it is avoided by using large amplitudes, such that $c_L A_{\text{osc}}$ exceeds the maximal interaction force.
For large amplitudes, in the case of an exponentially decaying force, such as a magnetic force, the equation can be inverted analytically. The result will be given in section 2.7.4 and appendix A. In order to invert this equation for a force with an arbitrary distance dependence, numerical methods are used. Two methods were proposed recently, both based on the linearity of the operation [28, 29]. In this thesis, one proposed by Dürig [28] has been used.
In the large amplitude regime, the frequency shift is dominated by the strong variation of the force near the point of closest approach and is inversely proportional to $A_{\text{osc}}^{3/2}$. In order to compare interaction forces without converting the frequency shift to force, the normalized frequency shift

$$\Gamma = \frac{\Delta f c_L A_{\text{osc}}^{3/2}}{f_0} \tag{2.9}$$

first introduced by Giessibl [27] is therefore sometimes used.

2.4.3 Frequency demodulation technique

In order to drive the cantilever always at its resonance frequency and to measure the latter, the phase of the excitation has to be always 90° with respect to the cantilever oscillation. This means that the frequency of the excitation has to be changed accordingly. The resonance frequency of the cantilever can be measured with a relative accuracy exceeding 1 ppm (parts per million) using the frequency demodulation technique (FM-detection) described in reference [30].
The smallest frequency shift detectable in this measurement mode due to thermal noise has been calculated by Albrecht et al. [30] in the small amplitude limit

$$\delta f_{\mathrm{rms}} = \frac{1}{A_{\mathrm{osc}}} \sqrt{\frac{k_B T b f_0}{\pi Q c_L}} \tag{2.10}$$

where b is the frequency measurement bandwidth, k_B is Boltzmann's constant and T is the temperature. Therefore, to enhance the signal to noise ratio, high Q cantilevers are used. The quality factor of the cantilever strongly depends on the pressure, therefore all measurements were performed in high vacuum or ultrahigh vacuum. Low temperatures also enhance the signal to noise ratio.

2.4.4 Non-conservative tip-sample interactions

So far, only conservative forces have been discussed. However it is possible that nonconservative surface forces exist, for example if the interaction force depends on time or on the velocity of the tip: $\vec{F}(\vec{x}, \dot{\vec{x}}, t)$ and lead to additional damping i.e. $\gamma_{\mathrm{total}}(\vec{x}) = \gamma_0 + \gamma(\vec{x})$. Such forces are discussed in paragraph 2.6.2.
In this case, in order to distinguish changes caused by conservative forces (resonance frequency shift) from changes due to nonconservative forces (additional energy dissipation), the amplitude of the excitation force can be adjusted to keep the oscillation amplitude constant.
It is well known that the power dissipated by a driven harmonic oscillator is proportional to its damping constant (or inversely proportional to its quality factor) on resonance ($f \approx f_0$) [31]. If the damping changes but the oscillation amplitude stays constant, the excitation amplitude is inversely proportional to the Q-factor (equation 2.6) and the additional energy dissipated per oscillation cycle is given by

$$\Delta E = \frac{E_0}{Q} - \frac{E_0}{Q_0} = \frac{E_0}{Q_0}\left(\frac{A_{\mathrm{exc}}}{A_{\mathrm{exc},0}} - 1\right) \tag{2.11}$$

Once the unperturbed quality factor, Q_0, has been measured, this equation can be used to convert the measured change in excitation amplitude to additional dissipated energy per oscillation cycle.

2.5 Detection electronics

To operate a SFM in dynamic mode, electronics is needed that fulfils the requirements described in the previous section. The general setup, common to both the RTSFM and LTSFM electronics, is shown in figure 2.6. If the oscillation amplitude is small with respect to one half of the laser's wavelength, the cantilever oscillation leads to a sinusoidal modulation of the intensity of the laser beam guided through a fiber and reflected from the cantilever back side. The reflected light is guided by a beam splitter to a photodiode and converted to an electrical signal proportional to the intensity of the laser light. The frequency and amplitude of this signal are measured by the frequency demodulation (FM) detection system. In the RTSFM and the LTSFM, two different electronic systems are used. The FM-detector used with the RTSFM has been described in reference [23]. It uses home-built analogue electronics as well as commercially available components. The FM-detector used with the LTSFM is a based on a home-built digital phase-locked-loop (PLL) described in references [32, 33].

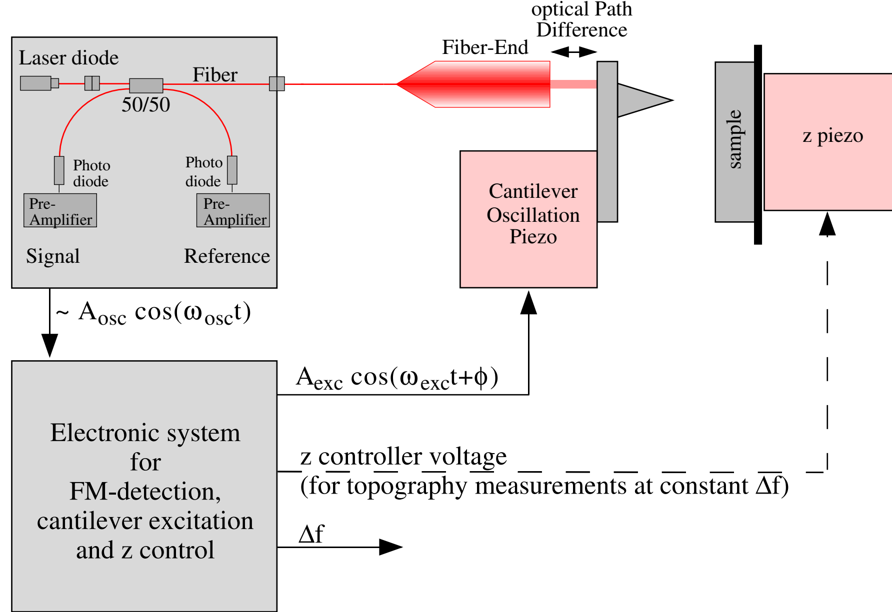

Figure 2.6: Schematic overview of the dynamic SFM setup.

The RTSFM is used in this thesis only for magnetic measurements in the constant height mode, where the frequency shift is measured as a function of the lateral position of the sample. The LTSFM is used in this thesis only for topographical measurements, where the voltage applied to the z piezo is varied in order to maintain the frequency shift at a constant value while scanning the sample under the oscillating tip.

2.5.1 RTSFM Electronics

The RTSFM electronics uses a home-built controlled oscillator for the cantilever amplitude (COCA) to oscillate the cantilever at its resonance frequency and at a constant amplitude. Using the COCA, the oscillation of the cantilever is excited by a feedback of the photodiode output with a fixed phaseshift (self-excitation). To measure the oscillation frequency, the interferometer

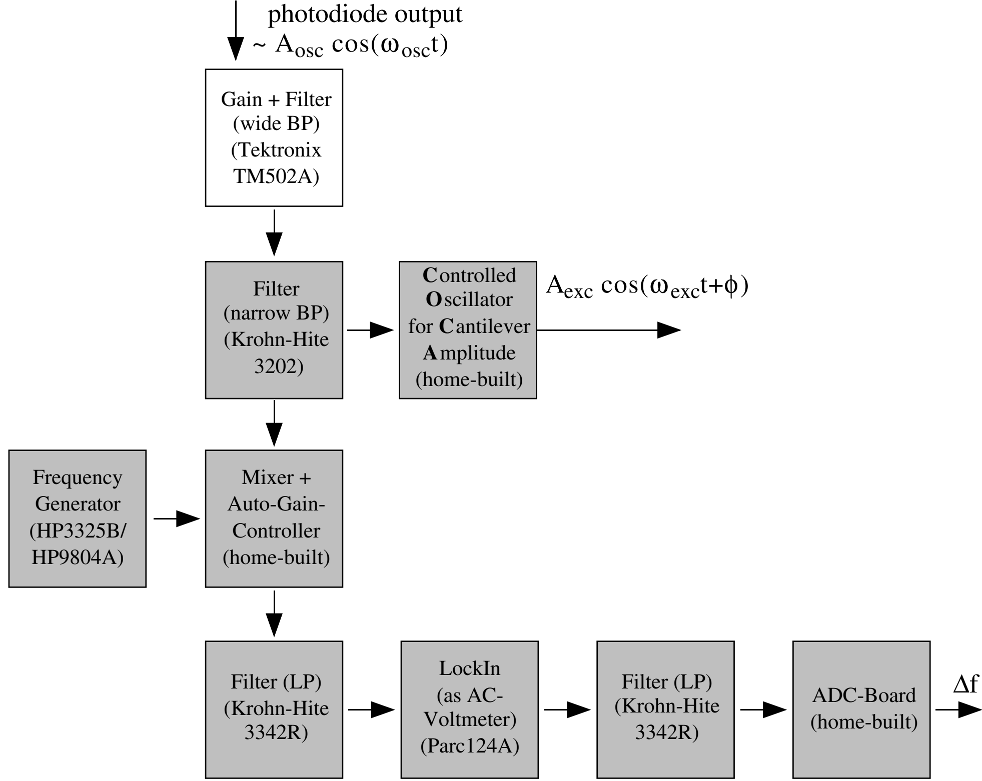

Figure 2.7: Details of the electronic system used for FM-detection and cantilever excitation in the RTSFM.

signal is connected to a mixer with automatic gain where the high cantilever oscillation frequency is mixed with a reference frequency to obtain a lower frequency signal of constant amplitude that can be measured more easily. This signal is filtered with a narrow band-pass filter. The amplitude of the filtered signal is a measure of the cantilever oscillation frequency. It is measured by a commercial lock-in amplifier used as an AC voltmeter.

2.5.2 LTSFM Electronics - PLL

In order to maintain the amplitude of the cantilever oscillation at a constant value, the LTSFM electronics uses an amplitude controller. This controller keeps the amplitude of the cantilever oscillation at a constant value by varying the sinusoidal excitation that is applied to the cantilever oscillation piezo.
The frequency of the interferometer signal input is compared inside the PLL to the setpoint frequency. The difference is fed to the z-controller that controls the z-piezo voltage and is also directly measured during the measurement. This frequency shift signal represents the error signal of the z-controller and therefore contains important information about the quality of the measurement. The output of the numerical controlled oscillator is used to excite the cantilever at the chosen amplitude. To do this, the phase has to be adjusted, as additional phase shifts might occur in the electronic circuit, but the cantilever is accurately excited with a 90° phase shift to oscillate at resonance even if the latter is shifted by the tip-sample interaction.

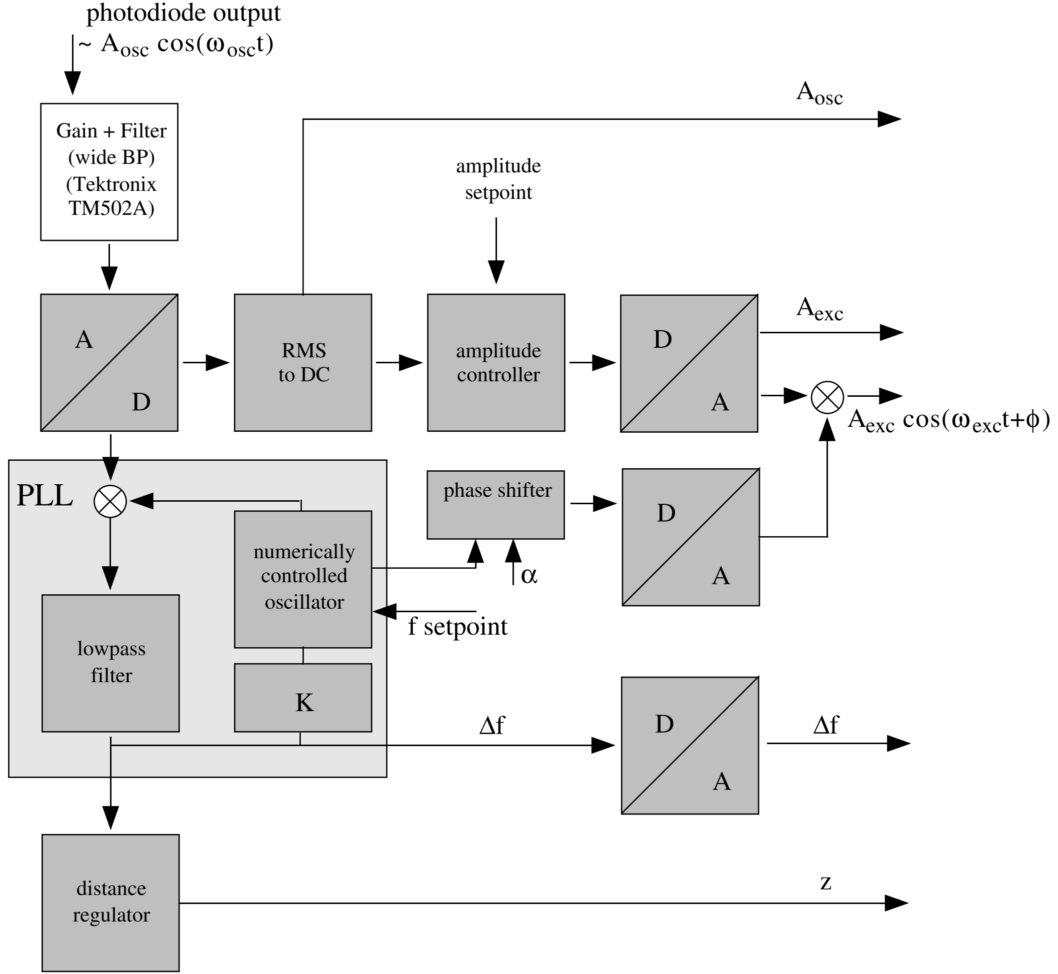

Figure 2.8: Details of the electronic system used for home-built FM-detection, cantilever excitation and z control in the LTSFM.

2.6 Forces

Various kinds of forces can be measured with a SFM. In general, conservative interaction forces can be described as (Hamaker approximation [34]):

$$\vec{F}(\vec{x}) = -\nabla \frac{1}{\mathrm{V_{sample}V_{tip}}} \int_{\mathrm{V_{sample}}} \int_{\mathrm{V_{tip}}} U_{\mathrm{tip/sample}}(\vec{x}, \vec{x'}) d^3\vec{x'} d^3\vec{x} \tag{2.12}$$

Here $\vec{x} = (x, y, z)$ is a coordinate system fixed to the sample as in figure 2.1. The forces can be classified according to the distance dependence of the underlying microscopic interaction potential $U_{\mathrm{tip/sample}}(\vec{x}, \vec{x'})$. If the variations of the microscopic interaction potential $U_{\mathrm{tip/sample}}(\vec{x}, \vec{x'})$ are small on the scale of interatomic distances, the integration can be carried out over a continuous tip and sample. These forces are called long-range forces and decay over a distance range of several nanometers or tens of nanometers. If the variations are not small, then the total force is rather a sum carried out over all forces acting between single atoms or ions, and the interaction

is called short-range [1].
The main long-range forces studied in this thesis result from van-der-Waals interactions, electrostatic interactions and magnetic interactions. The van-der-Waals and electrostatic interactions are background present in all SFM studies. The magnetic interaction is used to study the magnetic domain structure of particular samples in chapters 3 and 4. To be able to measure magnetic forces the tip has to be coated with magnetic material.
The main short-range interaction forces studied in this thesis are chemical bonding forces, short-range electrostatic and exchange forces (chapters 5 and 6). Short-range forces involve per definition mainly the tip apex. If the tip apex is atomically sharp, the main short-range contribution is given by the forces acting on only one tip atom thus allowing atomic resolution.
One of the main complications occurring with short-range forces is that the configuration and composition of the tip apex is in general not well known: The silicon tips used are stored in air, so their surface is covered with a native oxide of unknown structure and with a water layer. The water layer can be removed by heating the tip after introducing it to vacuum. However, when scanning over steps or defects or through tip crashes, the tip apex can change in an uncontrolled way, in particular, material from the sample surface can be deposited on the tip apex.
A related complication arises because short-range chemical bonding forces can become of the same order of magnitude as the forces that hold the tip apex atoms in their positions. Therefore, as the tip apex approaches the surface, the positions of the tip apex atoms may change gradually or irreversibly. Gradual changes are called relaxation. Relaxation can strongly influence the apparent distance dependence of the short-range forces [35]. Therefore, in order to compare measurements to theory, simulations taking account of this effect are needed.

2.6.1 Distance dependence of conservative forces

Long-range forces

Van-der-Waals forces
As only flat surfaces covered uniformly with only one chemical species are studied (in the ideal case), the long-range van-der-Waals force does not vary locally (it does not lead to imaging contrast). Therefore, a sample model consisting of a uniform semi-infinite flat surface is used. The tip (excluding the small nanotip at its end believed responsible for atomic resolution) is described as a cone with a spherical cap. Then, the van-der-Waals force is given by [36, 37]

$$F_{\mathrm{vdW}}(z) = -\frac{C_H}{6}\left[\frac{R}{z^2} + \frac{\tan^2\alpha}{z+R_\alpha} - \frac{R_\alpha}{z(z+R_\alpha)}\right] \tag{2.13}$$

where C_H is the Hamaker constant, R is the tip radius, $R_\alpha = R(1-\sin(\alpha))$ and z is the minimal distance of the surface to the tip[2].

Capacitive forces
Capacitive forces occur on metal and semiconductor surfaces if a voltage is applied or if the contact potentials of the tip and sample materials are not the same. The distance dependence of such a force for a conical tip with a spherical cap is given by

[1] The Hamaker approximation is not valid for the short-range forces.
[2] The cantilever canting will be neglected throughout the thesis except where necessary for the discussion of magnetic forces.

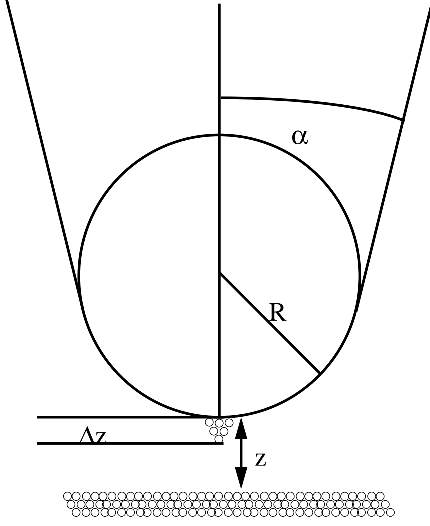

Figure 2.9: Tip model used for describing the van-der-Waals and electrostatic forces. The cluster at the end of the tip is the nanotip.

$$F_{\mathrm{el}}(z) = -\pi\varepsilon_0 \cdot (\Delta V)^2 \cdot \left[\frac{R}{z} + c^2(\alpha)\cdot\left(\ln\frac{l_{\mathrm{tip}}}{z+R_\alpha} - 1\right) - \frac{R\cdot(1 - c^2(\alpha)\cos^2\alpha/\sin\alpha)}{z+R_\alpha}\right] \quad (2.14)$$

where ΔV is the voltage difference, R is the tip radius, α is the cone angle, $R_\alpha = R(1-\sin\alpha)$ is the height of the spherical cap, $c(\alpha) = 1/\ln(\cot(\alpha/2))$ and l_{tip} is the tip length [36, 38].
As the capacitive force is proportional to $(\Delta V)^2$, sweeping ΔV results in a parabolic change of the frequency shift that can be used to find the contact potential difference between tip and sample on metals or semiconductor samples.

Electrostatic image forces
On insulating surfaces, static localized charge induces image charges in the conducting tip (figure 2.10a)). This surface charge can however be compensated by a polarization of the sample material induced by a voltage applied to the sample ground plate (figure 2.10b)). This polarization does not occur instantaneously when a voltage is applied but with a certain time constant related to the sample residual conductivity [39].

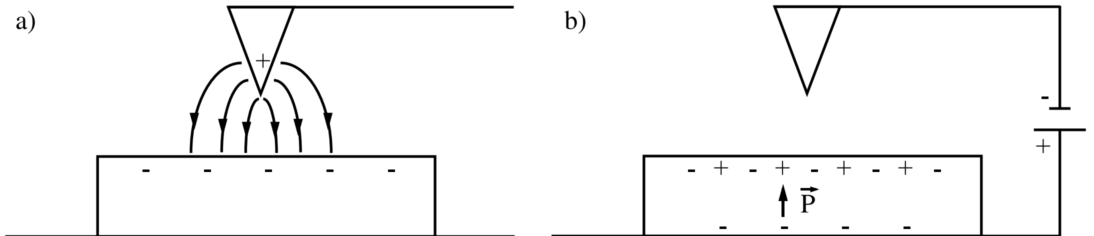

Figure 2.10: Image interaction on insulating surfaces a) without applying a voltage to the sample base b) after minimizing the electrostatic forces by applying a voltage to the sample base.

Magnetic forces
In order to describe magnetic forces, a model needs to be found that describes domains in a ferromagnetic sample, i.e. variations of the magnetization directions. This is a fundamental difference to the other long-range forces previously described as these long-range forces are no longer constant background interactions but are the object under study. We limit ourselves to models with perpendicular magnetization and negligible variation of the magnetization vector inside the sample. The sample is regarded as a superposition of sinusoidal magnetic patterns and the interaction of each of these with the tip is treated individually in Fourier space.
As the magnetic interaction is in our case not measured by a tip made of bulk magnetic material but rather by a silicon tip coated on one side with a thin magnetic layer, the tip cannot be described by a conical model. In the past, a pyramidal model has been successfully applied [16, 40], but a more general way of describing the tip has been found: the tip is calibrated using its imaging properties.
As described in paragraph 2.7 and proven in appendix A, the force exerted by each Fourier component of the sample magnetic pattern decays exponentially with a decay constant related to its wavelength. This is true for a magnetic tip of any shape.

Short-range forces

Chemical bonding forces
Chemical bonding forces are the object of study of SFM measurements with atomic resolution shown in chapters 5 and 6. From a theoretical point of view, they can be described using various models. In the theoretical part of this thesis (chapter 5.6), the Buckingham potential is used for describing chemical bonding forces acting between ions:

$$U_{\mathrm{B}}(r) = C_1 e^{-r/r_0} - \frac{C_2}{r^6} - \frac{C_3}{r^8} \tag{2.15}$$

where r is the distance and C_1, C_2, C_3 and r_0 are parameters obtained by fitting experimental data. The exponential term describes the repulsive force due to the Pauli exclusion principle, the other two terms describe the atomistic van-der-Waals attraction.

Short-range electrostatic forces
Short-range electrostatic forces can occur because of localized charge or dipoles present on atoms or ions. A static sinusoidal charge pattern leads to an exponentially decaying interaction similar to the long-range magnetic force. The decay constant is related to the period of the charge pattern [34]. This equation will be derived for the magnetic case in paragraph 2.7.

Exchange forces
The exchange interaction arises when electrons in two different orbitals interact and are exchanged between the two states through the Pauli exclusion principle in combination with electrostatic repulsion of the two electrons. If the spin direction of the two states is fixed, this leads to magnetic forces. The exchange interaction leads to the spontaneous occurrence of the ordered phase in ferromagnets and antiferromagnets. It is usually described with a Heisenberg hamiltonian

$$U_H(r) = \sum_{i,j} J_{i,j}(r)\vec{S}_i\vec{S}_j \tag{2.16}$$

where $J_{i,j}$ is the exchange interaction and S_i, S_j are the two interacting spin magnetic moments. Recently calculations have shown that exchange forces are expected to be of the order of nN, a magnitude readily accessible to SFM [19, 20].

2.6.2 Mechanisms of energy dissipation in dynamic mode SFM

In chapter 2.4 we mentioned that the cantilever oscillation amplitude is kept constant during the measurement. On resonance, the ratio of this amplitude to the excitation amplitude is given by the quality factor Q. During SFM measurements (images and frequency versus distance measurements), the excitation amplitude is measured and often shows contrast on the atomic scale. Several mechanisms have been proposed to explain the observed changes in excitation amplitude.

Apparent energy dissipation

The forces acting on the cantilever in the vicinity of the surface are highly nonlinear and can lead to a distortion of the resonance curve of the cantilever especially if the cantilever is too soft or if the oscillation amplitude is too small. Such effects have been shown experimentally by Erlandsson et al. [41] and discussed theoretically by Aimé et al. [42] and Gauthier and Tsukada [43]. This can lead to an apparent dissipation and to instabilities in the cantilever oscillation. However, the amplitude and the cantilever stiffness used here are so large that this cannot explain the observed energy dissipation. Instabilities have not been observed experimentally if the phase difference rather than the frequency is controlled and the tip oscillation amplitude rather than the excitation is kept constant [44, 32].

Friction-like energy dissipation

This type of dissipation is described by a dissipation force proportional to the velocity of the tip: $F_{\text{diss}}(z) = \gamma(z)\dot{z}$; it can have several physical origins.

a) Joule energy dissipation
Joule dissipation occurs when a DC voltage difference is applied between the tip and the sample or because the contact potentials of the two are not equal. In this case the tip-sample system can be modelled as a capacitor charging and discharging during each oscillation cycle. If the tip and sample are conducting, flowing currents are induced and energy will be dissipated. This energy is provided by the power supply. The RC-circuit has a certain time constant, and if the charging of the capacitor is not too slow or too fast compared to the cantilever oscillation, the force acting on the tip during approach will not be the same as during retraction. This dissipation is long-ranged, as the capacitive forces are long-ranged. The distance dependence of the damping is in this case approximately given by

$$\gamma(z) = 2\pi\varepsilon_0^2 \frac{(\Delta V)^2 R\rho\omega_0^2}{c_L z^2} \tag{2.17}$$

where ΔV is the voltage difference, R is the tip radius and ρ is the resistivity of the sample [45, 46, 32].

b) Brownian energy dissipation
Brownian dissipation occurs via coupling to the atomic vibrations of the tip and sample owing to their the mutual interaction. Although the phonons have typical frequencies that are much higher than the tip oscillation frequency, their presence disturbs the micro-reversibility of the process: The force during retraction is not exactly the same as during approach of the tip. The corresponding damping has been computed using the fluctuation-dissipation theorem

$$\gamma(z) = \frac{\pi m_{\text{eff}}}{k_B T}\Theta(\omega \to 0)\left(\frac{dF(z)}{dz}\right)^2 \tag{2.18}$$

where $F(z)$ is the short-range force assumed to act on the sample atom closest to the tip, m_{eff} is the effective mass of the cantilever and $\Theta(\omega \to 0)$ is related to the phonon density of states at low energy $N(\omega)$ by $\Theta(\omega) = N(\omega)/\omega^2$ [47, 48]. This formula gives values for γ that are several orders of magnitude smaller than experimentally observed values if $N(\omega)$ is estimated for a free surface. However, it can be significantly enhanced if relaxation caused by interaction with the tip is included [48, 49]. These modes are called soft modes and could interact more strongly with the cantilever oscillation.

Energy dissipation caused by hysteretic motion of atoms

Dissipation arises also when there is a difference between the approach and retraction curve due to a change of position of one or several atoms on the tip or on the surface [50]. In contrast to the previous mechanism, the change lasts for a longer time period, and may occur at each oscillation cycle. As the dependence of the energy dissipated by this mechanism on the cantilever velocity is different from that predicted for the Brownian motion mechanism, it is in principle possible to differentiate experimentally between the two mechanisms.

Energy dissipation caused by hysteretic motion of magnetic domain walls

Energy dissipation also occurs if there is a hysteretic motion of magnetic domain walls under the influence of the tip oscillation. This mechanism has been studied experimentally as well as theoretically [51, 52, 53].

2.7 Magnetic contrast formation

In this section, magnetic contrast formation is discussed for a tip with an arbitrary but fixed magnetization. In the previous section, the distance dependence of various forces was discussed using predetermined models for the tip. Here, not only the distance dependence of magnetic forces, but also the imaging properties of magnetic tips and the stray field of a thin magnetic film with perpendicular magnetization are discussed. The imaging properties of the tip can be used to characterize the tip, thus overcoming the need for models. This method has been mainly developed by van Schendel et al. [16, 40]. A more detailed discussion of the required transfer function theory is given in appendix A.

2.7.1 Contrast mechanisms and force acting on the tip

When attempting to record an MFM image, a field is applied to the sample by the tip and vice versa. This can in principle lead to different situations: There can be negligible modification of both the tip and the sample, there can be reversible modification of the tip or the sample or both, or there can be hysteretic or irreversible modification of the tip or the sample or both [54]. To obtain a reliable MFM image, the first case is desirable. It is also important to know how to exclude possible modification of either the tip or the sample from the images obtained.
If no mutual modification occurs, the force acting on the tip is given by the interaction of a dipole with a magnetic field:

$$\vec{F}(\vec{x}) = -\mu_0 \int_{-\infty}^{\infty} \vec{H}_{\text{sample}}(\vec{x'}) \cdot \nabla' \vec{M}_{\text{tip}}(\vec{x'} - \vec{x})\, d^3\vec{x'} \tag{2.19}$$

$$\text{where} \quad \vec{x'} = (x', y', z') \quad \text{and} \quad \nabla' = \left(\frac{\partial}{\partial x'}, \frac{\partial}{\partial y'}, \frac{\partial}{\partial z'}\right)$$

The role of the tip and the sample in this equation can be reversed [55]. If this form of equation 2.19 is chosen, the stray field of the sample in the region above the sample and the magnetization of the tip have to be studied in more detail. It is well known that a convolution in real space transforms into a simple product in Fourier space; therefore the discussion will be continued in Fourier space. Here we use two-dimensional Fourier transforms defined as:

$$\vec{f}(\vec{k}_{||}, z) = \int_{-\infty}^{\infty} \vec{f}(\vec{x}) \cdot e^{-i\vec{k}_{\|}\vec{x}_{\|}}\, dx\, dy$$

$$\vec{f}(\vec{x}) = \frac{1}{4\pi^2} \int_{-\infty}^{\infty} \vec{f}(\vec{k}_{||}, z) \cdot e^{i\vec{k}_{\|}\vec{x}_{\|}}\, dk_x\, dk_y \tag{2.20}$$

$$\text{where} \quad \vec{k}_{||} = (k_x, k_y) \quad \text{and} \quad \vec{x}_{||} = (x, y)$$

2.7.2 The tip equivalent magnetic charge distribution

As a result of transfer function theory, if mutual modification of tip and sample can be neglected, the magnetic force is given by the following equation:

$$\vec{F}(\vec{k}_{||}, z) = \mu_0 \vec{H}_{\text{sample}}(\vec{k}_{||}, z)\sigma^*_{\text{tip}}(\vec{k}_{||}) \tag{2.21}$$

σ_{tip} is a surface charge distribution located in the plane touching the tip apex. It is defined such that it creates a field equivalent to the field emitted by the tip. Its units are A/m in direct space and Am in Fourier space.
For simple tip geometries, σ_{tip} can be calculated (figure 2.11). A monopole is represented by a delta function in real space, and therefore shows a constant σ_{tip} in Fourier space, $q_{\text{M,tip}}$. A monopole at a certain additional distance to the surface, Δz (see figure 2.11) is represented by

$$\sigma_{\text{tip}}(k_{||}) = q_{\text{M,tip}} e^{-k_{\|}\Delta z} \tag{2.22}$$

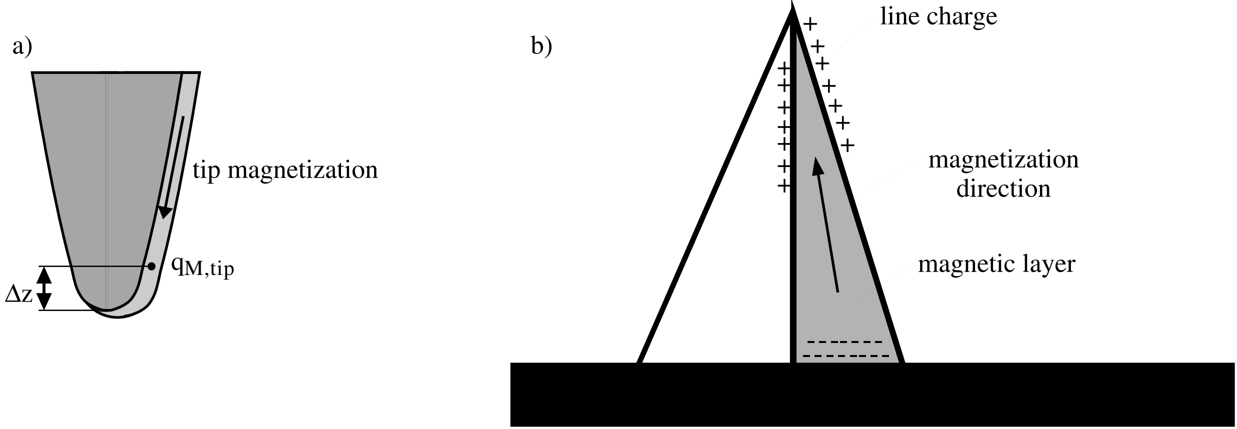

Figure 2.11: Tip models used to describe magnetic tips. a) Monopole model with additional distance to the surface, b) pyramidal tip model.

σ_{tip} has also been calculated for a tip consisting of a magnetic rod [56] and for a pyramidal tip [16].

In practice, equation 2.21 can be used in two ways: If the sample stray field is known and the force is measured, then the tip equivalent charge distribution can be calculated using this equation. If, on the other hand, the tip equivalent charge distribution is known, then the sample stray field can be calculated from a measurement of the force. In this chapter, equation 2.21 will be applied in the first way: The surface charge distribution of a test sample will be derived from MFM measurements, the resulting sample stray field will be calculated and used to characterize and compare MFM tips. This approach gives a better description of imaging properties for pyramidal Nanosensor tips than the use of a monopole model [16, 40].

Knowing σ_{tip}, the magnetic field emitted by the tip can be calculated [57, 58]:

$$\vec{H}_{\text{tip}}(\vec{k}_{||}, z) = -\frac{1}{2}\begin{pmatrix} ik_x \\ ik_y \\ k_{||} \end{pmatrix} \cdot \frac{1}{k_{||}} e^{-k_{||} z'} \cdot \sigma_{\text{tip}}(\vec{k}_{||}) \tag{2.23}$$

where z' is the distance of the field from the tip in the direction of the sample.

2.7.3 The stray field of a perpendicularly magnetized sample

In order to calculate σ_{tip} using equation 2.21, the sample stray field has to be known. In principle, the sample stray field is unknown, but for samples with perpendicular magnetization which does not depend on z, the magnetization pattern can easily be determined from an MFM measurement by applying a discrimination procedure: white contrast corresponds to repulsive forces (antiparallel magnetization), black contrast corresponds to attractive forces (parallel magnetization).

After determination of the magnetization pattern, the sample stray field can be calculated using the following formula [40, 59, 60]:

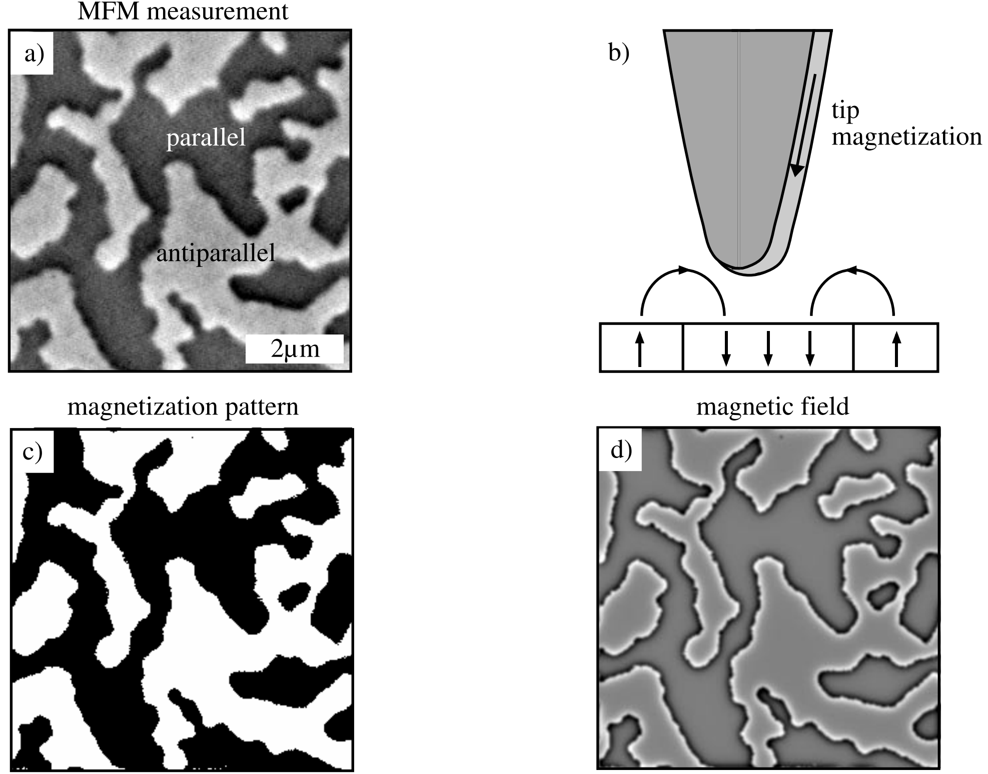

Figure 2.12: Determination of the sample stray field from a MFM measurement. a) MFM measurement showing domains parallel and antiparallel to the tip magnetization direction shown in b). c) Magnetization pattern obtained from the MFM measurement. d) Magnetic field calculated from the magnetization pattern.

$$\vec{H}_{\mathrm{sample}}(\vec{k}_{||}, z) = -\frac{\nabla}{k_{||}} \frac{(1 - e^{-k_{||}d})}{2} \frac{e^{-k_{||}z}}{k_{||}} \begin{pmatrix} -ik_x \\ -ik_y \\ k_{||} \end{pmatrix} \cdot \vec{M}(\vec{k}_{||}) \tag{2.24}$$

where d is the sample thickness.

2.7.4 Conversion of frequency shift to force

As all MFM measurements shown here are done in the dynamic constant height mode discussed in chapter 2.4, we have to convert the frequency shift to force. The frequency shift is given by [27] (see also equation 2.7):

$$\Delta f(\vec{x}_0) = -\frac{f_0}{\pi c_L A} \int_0^{\pi} \vec{n}\vec{F}(\vec{x}(\varphi)) \cos\varphi d\varphi \quad \text{where} \quad \vec{x} = \vec{x}_0 + \vec{n} \cdot A \cos\varphi \tag{2.25}$$

Here $\vec{n}$ is the direction of the oscillation of the cantilever. This equation transforms to the following equation for a magnetic force (see also appendix A):

$$\Delta f(\vec{k}_{||}, z_0) = \frac{f_0\mu_0}{2c_L} \cdot \vec{n}\vec{F}(\vec{k}_{||}, z_0) \cdot \frac{2}{A} I_1(iA(\vec{k}_{||}\vec{n}_{||} - k_{||}n_z)) \tag{2.26}$$

$$\text{where} \quad I_1(u) = \frac{1}{\pi}\int_0^{\pi} e^{-u\cos\varphi}\cos\varphi d\varphi \qquad u \in \mathbb{C}$$

is the first order modified Bessel function of the first kind. In the small amplitude limit the Bessel function is proportional to $z/2$ and the signal is proportional to the force derivative. For large amplitudes and large $\vec{k}$ this is no longer the case. If the minimal distance to the sample, $\vec{x}_0 - A\vec{n}$ is kept constant while increasing the oscillation amplitude, the measurement becomes less sensitive to short wavelengths of the sample magnetization.

2.7.5 Distance dependence of the frequency shift

In appendix A it is proven that if there is no modification of the tip and sample magnetization, the magnetic force decays exponentially as a function of distance:

$$\vec{F}(\vec{k}_{||}, z) = \vec{F}(\vec{k}_{||}, 0) \cdot e^{-k_{||}z} \tag{2.27}$$

As this equation is only valid if σ_{tip} does not depend on the distance to the sample, it can be used to test whether mutual modification of the tip and sample is indeed negligible and thus determine whether transfer function theory is applicable to a particular experiment.
In order to perform this test, a series of images (images i = 1 to n) is taken with the same tip at different distances z but at the same lateral position on the sample. For each of these measurements, a spectrum is calculated. We define the spectrum of a measurement as the circular average over constant absolute value of $k_{||}$ of the 2D Fourier transformed image. The spectrum of the image

$$< \Delta f(k_{||}, z) >=< \Delta f(k_{||}, 0) > \cdot e^{-k_{||}z} \tag{2.28}$$

where $< \ldots >$ means the average over constant $k_{||}$, is also proportional to $e^{-k_{||}z}$. In order to eliminate $< \Delta f(k_{||}, 0) >$, the spectra obtained from the series of images are normalized by the spectrum obtained from the image acquired at the closest distance (image 1). These normalized spectra are given by (see also reference [53])

$$\frac{< \Delta f(\vec{k}_{||}, z_i) >}{< \Delta f(\vec{k}_{||}, z_1) >} = e^{-k_{||}(z_i - z_1)} \tag{2.29}$$

From these normalized spectra the relative distances $z_i - z_1$ can be obtained.
This property will be used in chapter 4.3.3. Equation 2.27 shows immediately how important it is to be as close as possible to the sample for measuring small wavelengths of the sample field. The measuring distance has to be of the order of the smallest wavelength of the field to be resolved.

Chapter 3

Perpendicular magnetic domains of a thin Ag/Fe/Ag film observed by magnetic force microscopy at room temperature

3.1 Introduction

Ultrathin magnetic films are widely studied because of their interesting magnetic properties: as the film thickness is reduced, the influence of the surfaces increases, and in some cases, the anisotropy changes from in plane to out of plane easy axis due to surface anisotropy. A good example for this phenomenon are Ag/Fe/Ag sandwiches - they show a magnetic reorientation transition as a function of the film thickness and temperature. At a thickness lower than about three to five atomic layers, the iron layer is magnetized out of plane; above this critical film thickness, the magnetization of the film lies in the plane. In the transition region, the effective perpendicular anisotropy constant becomes small. The peculiarity of thin Fe films sandwiched between Ag is that this reorientation transition takes place at relatively low film thicknesses, so that the film is still close to two-dimensional behaviour. Mermin and Wagner proved in 1966 that a two-dimensional isotropic Heisenberg magnet cannot show long-range magnetic order in the absence of anisotropy [61]. Therefore the question was raised whether Ag/Fe/Ag thin films show a region of absent or reduced magnetization. For films with a large thickness range with perpendicular magnetization, just below the reorientation transition, a reduced remanent magnetization was measured [62]. It has been speculated that this reduced perpendicular remanence is due to magnetic domains.
Magnetic domains have been detected in many thin magnetic films with perpendicular anisotropy by scanning electron microscopy with polarization analysis (SEMPA) and by magnetic force microscopy (MFM). Here we focus on the domain structure of ultrathin films where a reversible transition of the magnetization direction has been observed as a function of temperature. Perpendicular domains have been studied by SEMPA only on one such system, Fe/Cu [7, 63]. On Ag/Fe/Ag thin films only in plane domains, typical size 0.1 mm, could be imaged until now by Kerr microscopy above the reorientation transition [64]. For thin films with perpendicular anisotropy, like Ag/Fe/Ag sandwiches below the reorientation transition, the domain size de-

creases strongly with increasing film thickness. This has been calculated theoretically [65] and observed experimentally [3]. Based on general thermodynamic considerations a definite shape variation of the perpendicular domains of thin films showing temperature and film thickness dependent perpendicular magnetic anisotropy has been predicted: the domains are expected to exhibit a stripe pattern (called "nematic or smectic phase" in reference [66])" at small film thicknesses or low temperatures. The pattern is predicted to become more isotropic (called "tetragonal liquid") near the reorientation transition. As these predictions are based on thermodynamic considerations, they are valid not only for Ag/Fe/Ag but also for other similar systems such as Fe/Cu. A shape variation from stripe domains at small film thicknesses and isotropic domains at large film thicknesses has been observed experimentally in the Fe/Cu system [4]. We were interested in the question how small these domains become near the reorientation transition, and whether they persist or whether there is a range where no long-range magnetic order exists.

Although we cannot definitely answer these questions, magnetic force microscopy (MFM) can improve our understanding by studying magnetic domains of thin Fe films in the perpendicularly magnetized region at room temperature. One of the main problems is to know precisely at which film thicknesses and temperatures the ultrathin films are expected to show perpendicular magnetization, as results obtained through the study of hysteresis curves vary strongly [62, 67, 68, 69, 70]. For example Qiu et al. [62] found that for thicknesses smaller than 6.5 atomic layers the films were magnetized in the perpendicular direction, while Berger and Hopster [67] found that the magnetization of a film of 4.3 atomic layers of Fe was in-plane above 270 K. Recently, these differences of the magnetic properties could be related to differences in the microscopic interface morphology [68]. A method for preparing flat interfaces has been proposed [71]. The films studied in this article have been prepared following Schaller et al. Another main experimental problem that has to be solved, is that the coercive field of these films is so low that a conventional MFM tip will strongly modify the domain pattern of the thin film. Therefore, a special MFM tip had to be designed that generates a field smaller than the coercive field of the sample. From the study of the domain size in dependence of the film thickness, the surface anisotropy of the film can be estimated and compared to the values obtained from other techniques.

3.2 Tip and sample preparation

Samples were prepared in the ultra-high vacuum system described in references [68, 71]. More details about sample preparation and characterization can be found in these references. The system has a base pressure of $5 \cdot 10^{-11}$ mbar. As substrate, a 150 nm thick Ag film was grown on a Fe precovered GaAs(001) wafer. This Ag film was grown at 100° C and subsequently annealed at 300° C for one hour. A high-quality single crystalline Ag(001) film was obtained. A wedge-shaped Fe film with a slope of 2.51 ML/mm = 0.361 nm/mm was prepared by linearly moving a shutter in front of the substrate kept at room temperature during deposition. During the measurements described in the following, the film thickness was determined from the lateral position on the sample. After deposition, the Fe film was annealed at 200° C following Schaller et al. [68] to obtain the lowest interfacial roughness and the highest perpendicular anisotropy. Before exposing the sample to air, it was covered with 5 nm Ag to get a similar interface on the top of the film and then with 5 nm of Au to prevent oxidation.

Similarly prepared Ag/Fe/Ag thin films were characterized ex situ by magneto-optical Kerr effect

(MOKE) hysteresis measurements. They showed perpendicular magnetization in the thickness range of 2.5 to 5 atomic layers [68].
All MFM measurements were carried out in our home-built instrument. This instrument is similar to the low temperature ultra high vacuum SFM described in reference [24], but operates at room temperature and under high vacuum conditions. The scanner of our instrument was calibrated and linearized carefully as described in reference [24]. High vacuum allows us to measure in dynamic mode with high Q cantilevers oscillating at a constant amplitude and to apply frequency modulation detection as described in reference [30]. In this measurement mode, high sensitivity is achieved and the frequency shift signals obtained can be interpreted quantitatively [16]. All measurements were done in the constant height mode at a mean tip-sample distance of about 50 nm. We used a soft Si_3N_4 cantilever with a force constant $c_L = 0.03$ N/m and a resonance frequency $f_0 = 16.5$ kHz for a high force sensitivity with an oscillation amplitude of 30 nm. From these values the minimal detectable frequency shift due to thermal noise can be estimated using the formula derived by Albrecht et al. [30] (equation 2.10)

$$\delta f_{\mathrm{rms}} = \frac{1}{A} \sqrt{\frac{k_B T b f_0}{\pi Q c_L}} \qquad (3.1)$$

For a quality factor of the cantilever $Q = 10\ 000$, a temperature $T = 300$ K and a measurement bandwidth $b = 100$ Hz as in the experiment, one obtains $\delta f = 0.1$ Hz. Before imaging, the tip was magnetized in the direction perpendicular to the sample using a magnetic field of about 0.4 T generated by a permanent magnet.
When imaging soft magnetic samples by MFM, the magnetization of the sample may be influenced by the stray field of the MFM tip. The coercive field of our sample as measured by MOKE is less than about 1 mT. Therefore, special care has been taken to reduce the stray field of the tip. On the commercially available tip, a carbon needle has been grown by electron beam induced deposition. After growth, 9.4 nm of iron were evaporated onto the carbon needle under high vacuum conditions ($p = 10^{-5}$ to 10^{-6} mbar). This method has been proposed by Rührig et al. [72] to reduce the lateral extent of the magnetic field generated by the tip. The quality of this iron layer and the magnetic field generated from the tip depend strongly on the pressure during evaporation. A tip was selected if it produced a weak signal in test measurements on a reference Cu/Ni/Cu sample. Van Schendel proposed the following method for calibrating magnetic tips [16]. The frequency change on a well-known reference sample is used to determine first the amplitude with which a certain Fourier component of the magnetization is imaged by the tip. From the calibration of the tip one can calculate the generated field and its spatial distribution. With this tip a calibration was obtained based on one image taken on a Cu/Ni/Cu sandwich. Based on this calibration we estimate that the field is only about 1.1 mT at the position of the tip apex and extends over less than 300 nm full width at half maximum in the lateral direction. This is small compared to values obtained with different tips, e.g. 9.5 mT for the tip calibrated in reference [16]. As the field emanating from this tip is larger than the coercive field of the sample, perturbations of the magnetic state of the sample are still possible. Note, however, that this is the field present at the tip apex and that the measuring distance to the magnetic layer is always larger than 10 nm due to the Ag and Au capping layers.
We have tried to further reduce the thickness of the Fe film on our tips, but the quality of Fe films deposited under high vacuum conditions was too poor to give reproducible results at lower coverage. The quality of the Fe films could be improved by using UHV evaporation. Another

possibility is to deposit a material with lower saturation magnetization on the tip, for example Ni, instead of Fe. These approaches are studied in chapter 4.

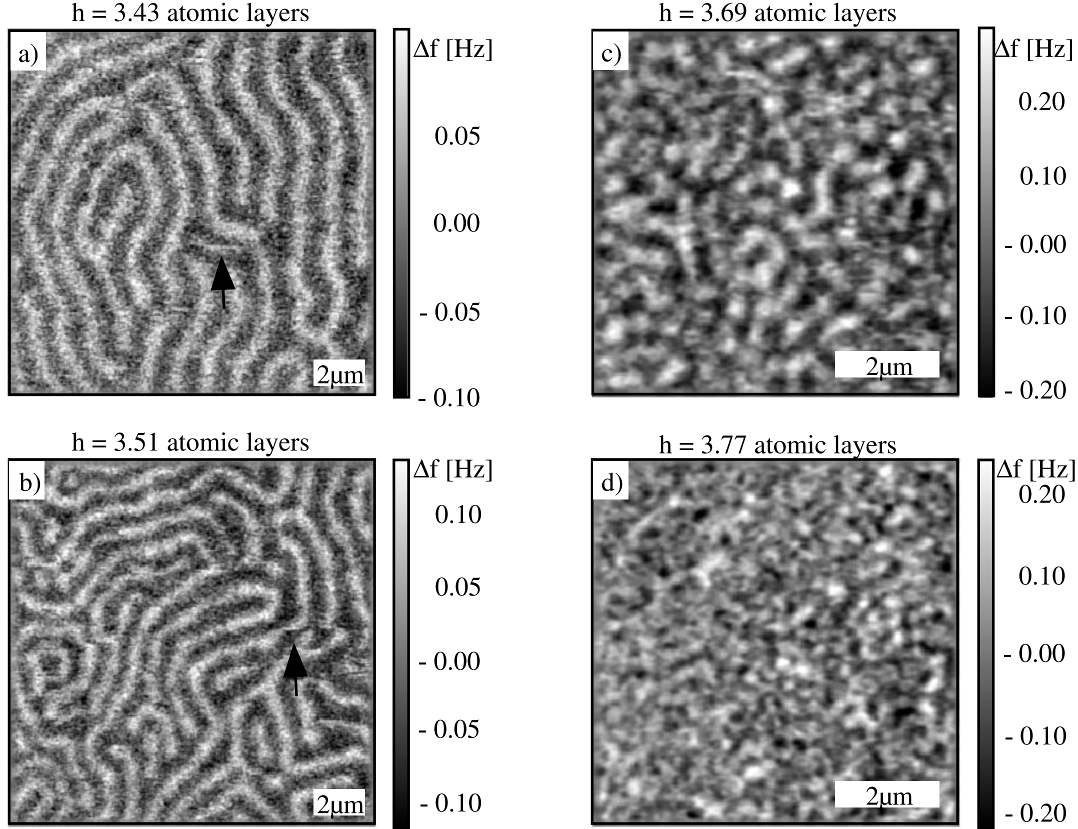

Figure 3.1: Four MFM images of magnetic domains for different Fe thicknesses: a) 3.43 b) 3.51 c) 3.69 and d) 3.77 atomic layers of iron. All images have been filtered. The arrows indicate movement of the domain walls under the influence of the tip. Note that images a) and b) cover a larger area than images c) and d).

3.3 Magnetic Force Microscopy images

The Fe wedge sandwiched between two Ag thin films has been investigated by MFM in the thickness region between 0 and 7 atomic layers. Perpendicular magnetic domains could be imaged in the thickness region between 3.34 to 3.77 atomic layers of iron (Figure 3.1). In the simplest picture, black contrast (attractive force) corresponds to domains pointing into the sample plane, while white contrast (repulsive force) corresponds to domains pointing out of the sample plane (or vice versa). The observed peak-to-peak frequency variation was only $\Delta f = 0.2$ Hz translating into a force gradient $dF/dz = 2c_L\Delta f/f_0 = 730$ nN/m. The observed frequency shift difference is only slightly above the thermal noise limit. The magnetic structures observed here are typical for perpendicularly magnetized thin films and resemble in size and shape the domains imaged on other samples [3, 8, 63]. At small film thicknesses, the domains are larger and stripe-shaped, while at larger film thicknesses the domain size decreases and the domains become more isotropic. MFM images with such a small magnetic contrast may be influenced by the sample topography.

However, in images 3.1 a) b) and c) the size and shape of the observed structures differ from any topographical structures observed by STM on a similar sample [71]. We therefore conclude that the observed contrast is in fact due to the domain structure of the film. Only in image 3.1 d) an influence of the topography cannot be excluded.
As mentioned above, the stray field of the tip is larger than the coercive field of the sample, and therefore, a distortion of the domain structure under the influence of the tip may be possible. In the images 3.1 a) and b) discontinuous changes of the contrast are observed (see arrows), which can be attributed to the perturbation of a domain wall position by the tip. Fortunately, most of the image is free of such artefacts, moreover the image acquired during back-scans is identical to that acquired during forward-scans. Therefore, the perturbation of the sample by the tip can be neglected. However, at film thicknesses lower than 3.34 atomic layers, the number of locations where the magnetic structure of the sample is disturbed increases, and eventually a major part of the image is distorted by such instabilities (image not shown). In this thickness range, the domain pattern cannot be imaged. This is consistent with the observation by Schaller et al. that the Curie temperature is reduced for films thinner than 3.5 atomic layers [68].
The fact that we cannot image domains at film thicknesses larger than 3.77 atomic layers of Fe seems to contradict the measurement of the reorientation transition at a film thickness of about 5 atomic layers by the same authors. One possible explanation is the modification of the sample by the tip. Another one is that the resolution of our MFM could be too low to resolve the domains. On the other hand, we have shown that the lateral resolution of our MFM is about 40 nm [73] i.e. much smaller than the domain size observed at 3.77 atomic layers of Fe (190 nm). It is possible that the coercive field and the perpendicular anisotropy of the film are so low for film thicknesses near the reorientation transition that the domains are modified under the influence of the tip, as expected from theory [66]. It is also possible that the reorientation transition occurs at a smaller thickness in our film, as small differences in the film morphology are crucial. In summary, inspite of the experimental difficulties due to thermal noise, tip-sample interaction and influence of topography on the measured images, the size and shape of the domains can be clearly identified in all images shown here and will be discussed in detail in the following.

3.4 Analysis of the domain size

From our MFM measurements, the domain size can be extracted and compared to models. The domain size and pattern observed on this Ag/Fe/Ag sandwich vary strongly with film thickness. Kaplan and Gehring [65] have calculated the variation of the domain size with film thickness in thin films with perpendicular anisotropy:

$$D = C_{\text{pattern}} d_{\text{Fe}} \exp\left(\frac{\pi l_{\text{dipolar}}}{2 d_{\text{Fe}}}\right) \quad \text{where} \quad l_{\text{dipolar}} = \frac{\sigma_W(h)}{1/2 \mu_0 M_S^2} \tag{3.2}$$

where d_{Fe} is the film thickness, C_{pattern} is a numerical factor which is characteristic for a certain domain pattern ($C_{\text{pattern}} = 0.955$ for a stripe pattern and $C_{\text{pattern}} = 2.62$ for a checkerboard pattern), σ_W is the domain wall energy per unit of surface and M_S is the saturation magnetization. The anisotropy and also the wall energy vary with film thickness. Taking the formula for Bloch walls we obtain

$$\sigma_W = 4\sqrt{C_{\text{exc}} K_u} \quad \text{with} \quad K_u = K_V + \frac{2 * K_S}{h} \tag{3.3}$$

where we have assumed the bulk exchange constant $C_{\rm exc} = 1.49 \cdot 10^{-11}$ J/m [74] for iron and the cubic bulk value for the volume anisotropy $K_V = 4.75 \cdot 10^4$ J/m^3 [75]. A fit according to equation 3.3 where K_S is the only free parameter gives $K_S = 0.266$ mJ/m^2 (figure 3.2). In this fitting procedure, the point obtained at the lowest film thickness was not taken into account, because at this film thickness the domains are already unstable under the influence of the tip and we might not measure their size correctly. The value obtained for K_S is in good agreement with the measurement by Heinrich et al. [76], $K_S = 0.277$ mJ/m^2. It is also in good agreement with $K_S = 0.27$ mJ/m^2 obtained by Schaller et al. [68].

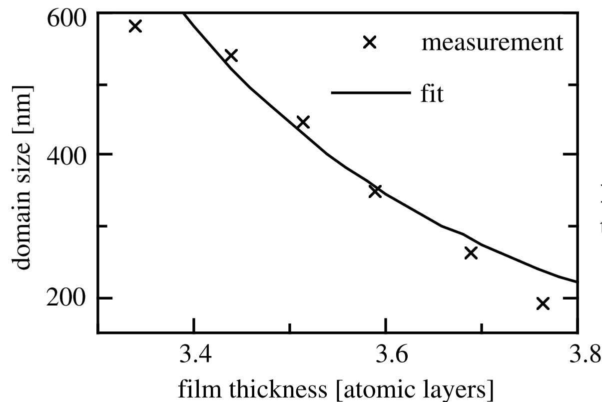

Figure 3.2: Domain size as a function of the Fe film thickness in atomic layers and fit to equation 3.3.

In the study by Schaller et al. [68], the effect of roughness on K_S was carefully taken into account following the analysis by Bruno [77]. The main reason to do this is that the anisotropy constant is in their case determined by taking the difference of the energy necessary to magnetize the film in plane and the energy necessary to magnetize the film in the perpendicular direction. Roughness mainly affects the first energy. In our analysis, however, the magnetization is always perpendicular to the film plane, and therefore we only have to take the change of the second energy into account. This change is negligible even for the roughest of the films investigated by Schaller et al. [68]. In our case, the most important effect of roughness is a reduction of the exchange constant. In the case of a film only 4 atomic layers thick, already half of the atoms constituting a domain wall have a reduced number of nearest neighbours. This could lower the exchange constant A and thus lead to an artificially low K_S. From the STM study by Bürgler et al. [71], we also know that the interfaces exhibit roughness on a lateral scale of about 10 nm, which is of the order of the domain wall thickness but still much smaller than the observed domain size. The exchange constant A could be lowered further by this roughness.
The largest error on our value of K_S is due to the fact that the absolute lateral position of the sample was only precise to about 250 μm although the relative positions of the images taken could be measured with a precision of about 10 μm, resulting in an error on the film thickness and on the value obtained for K_S of ± 0.13 mJ/m^2.

3.5 Analysis of the domain shape

The perpendicular magnetic domains observed on ultrathin Ag/Fe/Ag sandwiches show a strong variation of their shape from stripe domains to an isotropic pattern as the film thickness is increased. This transition seems to takes place gradually: while in image 3.1a) the domains are stripe-shaped with a few defects, the stripes show even less long-range alignment in image 3.1b),

but remain locally aligned. In image 3.1c) the domains are still elongated, but disordered, and in image 3.1d) some domains have a round shape. Recently, the domain shape in ultrathin films was analysed theoretically [66]. A phase diagram of the domain shape as a function of temperature and applied external field in the direction parallel and perpendicular to the film was proposed. At low temperatures the domains should show a stripe-like pattern and at higher temperatures, the orientational order should change to that of a tetragonal liquid near the transition to in-plane magnetization. Unfortunately, this phase diagram was not calculated as a function of the film thickness, but it can be inferred that a similar variation of the domain size should be observed as a function of film thickness in qualitative agreement with our experiments. A similar variation of the domain shape as a function of film thickness has been observed by SEMPA on Fe/Cu thin films [63].

3.6 Conclusions

Qiu et al. [62] have suggested the existence of magnetic domains with perpendicular magnetization near the magnetic reorientation transition of thin Ag/Fe/Ag samples. Our room temperature MFM measurements confirmed this hypothesis. The domain size and shape was found to vary as a function of film thickness. The observed domain size decreases strongly with increasing film thickness in agreement with the model provided by Kaplan and Gehring [65]. The analysis of the domain size as a function of film thickness is consistent with a value of the surface anisotropy similar to that measured by Schaller et al. [68] and Heinrich et al. [76]. The domain shape variation as a function of film thickness predicted by Abanov et al. [66], from stripe domains on thin films to isotropic domains on thick films, was also confirmed by our measurements. In order to test the applicability of the Mermin-Wagner theorem on ultrathin films of Ag/Fe/Ag, it is not sufficient to confirm a reduced remanent magnetization near the reorientation transition, but it should also be shown that this reduced remanent magnetization is not simply due to the presence of magnetic domains.

Chapter 4

Quantitative magnetic force microscopy

4.1 Introduction

In the previous chapter, the imaging of magnetic domains on Ag/Fe/Ag has been discussed. For the study of magnetic domains in an Ag/Fe/Ag sandwich and for many other samples with low coercive fields, it is important to reduce the magnetic stray field of the tip in order to prevent a perturbation of the micromagnetic state of the sample during imaging. The tip used in the last chapter was coated under high vacuum conditions with a 9.4 nm thick Fe film. The stray field of such a tip can be reduced, if a magnetic Fe film of smaller thickness is used. Another way of reducing the stray field is to deposit a material with a lower saturation magnetization than Fe on the tip, for example Ni. These "ultralow strayfield" tips should be prepared in a reproducible way, inspite of the small film thickness of their magnetic coating, and their micromagnetic structure should not be modified by the sample stray field.

Another problem in MFM is the improvement of the resolution. In chapter 3, domains with a size of about 200 nm were shown. The resolution obtained by MFM today is about 40 nm, but on many samples, for example on the CAMST[1] sample, domains of smaller sizes are known to exist [73]. A high resolution is also needed to image bits on today's hard disks [53]. The resolution of an MFM is only limited by the shape of the magnetic charge distribution on the tip. The magnetic forces are long-ranged compared to the short-range forces probed in atomic resolution experiments and therefore not only the magnetic charge distribution on the tip of the nanoscopic tip apex is important, but also the mesoscopic tip charge distribution. The resolution can only be improved, if this mesoscopic tip charge distribution can be confined to a smaller volume.

These two problems are related to the question how MFM tips can be characterized. The magnetic field generated by the tip has been investigated experimentally using electron holography or tomography [78, 79, 80]. There have also been attempts to interpret MFM images in a quantitative way [81, 55, 82, 83, 56, 84, 85]. Recently, a method to calculate the imaging properties of MFM tips from images of a well-known standard sample has been proposed [16, 40]. This method, known as quantitative magnetic force microscopy, will be applied in this chapter to

[1] Concerted Action on Magnetic Storage Technology program of the European Community see reference [73]. A description of this sample is given in chapter 4.2.2

characterize ultralow strayfield and ultrasharp tips.
In total 25 tips have been tested, some of them on several samples and with several image sizes. The imaging properties of 10 of these tips have been analysed using quantitative magnetic force microscopy. Out of these, the data of seven tips have been chosen to address the questions raised above.

4.2 Tip and sample preparation

4.2.1 Tip preparation

For both, ultralow strayfield and ultrasharp tips, it is important to deposit a thin magnetic layer in a reproducible way. A good film quality is obtained if the thin film does not contain significant amounts of impurities, i.e. it is, for example, not oxidized during growth, and it is smooth and continuous. Oxidation or grain formation can lead to magnetically soft or nonmagnetic properties of thin films. The deposition of Fe films on tips using a heated Fe wire under high vacuum conditions (used previously in our group) provided reproducible MFM tips, but the frequency shift obtained on a standard test sample with the tips on a standard test sample depended on the quality of the vacuum during evaporation (see chapter 3.2). Quantitative magnetic force microscopy revealed that the magnetic field generated by the tips was smaller than the magnetic field calculated for a tip of similar geometry [16].
To obtain thin films generating larger magnetic fields for the same film thickness, preparation in UHV was implemented. For all tips described in this chapter, the magnetic layers were deposited on the tips using the electron beam evaporator in the preparation chamber (chapter 2.2). Pyramidal Nanosensor tips and conical ultrasharp tips will be discussed in this chapter. SEM pictures of the two tip shapes are given in section 4.3 for the Nanosensor tips and in section 4.4 for the ultrasharp tips.
Special care has been taken to coat only one side of the tip. Therefore all tips were coated with magnetic material in the direction forming an angle of $\theta = 60°$ with the cantilever (see figure 4.1). This procedure should avoid the formation of flux closure domains or domain walls at the tip apex that may occur when the tip is magnetized in the direction parallel to the magnetic film plane of the tip coating (almost perpendicular to the sample surface) [40].

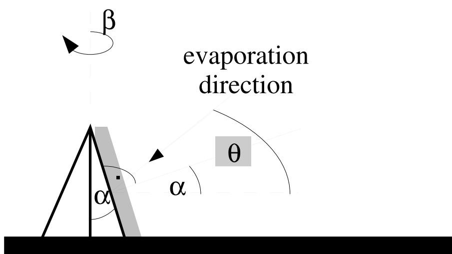

Figure 4.1: Sketch of the evaporation direction of the magnetic layer deposited on the tip.

Coating the tip under a certain angle relative to the tip surface reduces the effective film thickness deposited on the tip. For the pyramidal Nanosensor tips, the tip facet orientation can be described using two angles: α and an azimuth, β (see figure 4.1). For the ultrasharp tips of conical shape, β cannot be defined. The magnetic coating on ultrasharp tips is inhomogeneous. The film thickness deposited on both types of tips will be given using $\theta = 60°$ and $\alpha = 10°$ for the Nanosensor tip and $\alpha = 5°$ for the ultrasharp tip: The nominal layer thickness

$$d_{\text{film, nom}} = \cos|\theta - \alpha| \cdot d_{\text{film, Quartz}} \tag{4.1}$$

where $d_{\text{film, Quartz}}$ is the film thickness measured by the quartz microbalance[2]. β cannot be taken into account for all tips and has therefore not been taken into account. However, it is important to note that the physical thickness of the layer on the tip is even smaller than the nominal value that will be given in the following, because of the deposition angle.
The cantilever itself is masked during evaporation in order to preserve its high Q factor of about 10 000. After deposition of the magnetic layer, the tips were coated with a Au or Pd protection layer of 3 nm and then magnetized in a magnetic field of about 0.4 T applied in the direction perpendicular to the cantilever using a permanent magnet. They were then transferred to the RTSFM.

4.2.2 Calibration procedure and choice of the test sample

As mentioned before (chapters 2.7.2 and 2.7.4), the surface charge distribution generating the same field as the tip, σ_{tip}, can be calculated from a MFM measurement if the sample stray field is known (equations 2.21 and 2.27).

$$\vec{F}(\vec{k}_{||}, z) = \mu_0 \vec{H}_{\text{sample}}(\vec{k}_{||}, z)\sigma^*_{\text{tip}}(\vec{k}_{||}) \tag{4.2}$$

where $\vec{F}(\vec{k}_{||}, z)$ is the two-dimensional Fourier transform of the measured force, $\vec{k}_{||}$ is a two dimensional wavevector in Fourier space and $\vec{H}_{\text{sample}}$ is the sample stray field.

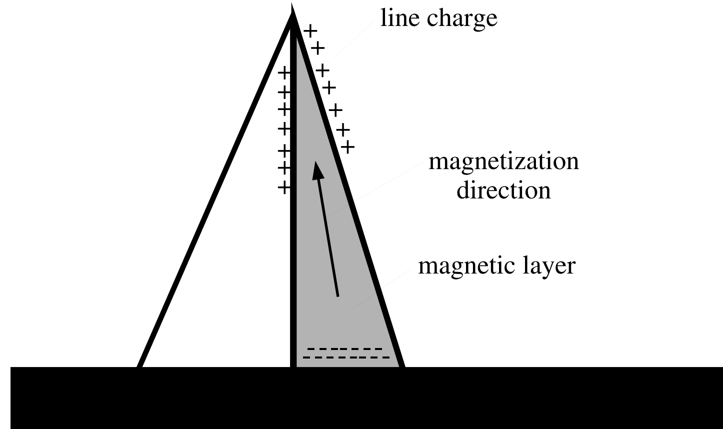

Figure 4.2: Sketch of the charge distribution for a pyramidal Nanosensor.

This approach gives a better description of the tip's imaging properties than simple monopole or dipole models, especially for the pyramidal Nanosensor tips. The imaging properties of Nanosensor tips are strongly determined by the line charge located at the edge of its pyramidal facets. In section 4.4 it will be discussed whether monopole models are suitable to describe conical ultrasharp tips.
The determination of the sample stray field relies on the MFM measurement itself. The magnetization pattern of the sample can be determined easily from an MFM measurement on a

[2]For the tip used in chapter 3, the evaporation angle was $\theta = 30°$.

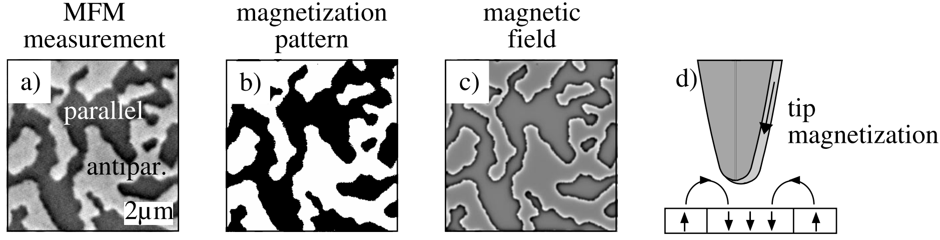

Figure 4.3: Determination of the sample stray field from a MFM measurement. a) MFM measurement showing domains parallel and antiparallel to the tip magnetization direction shown in b). c) Magnetization pattern obtained from the MFM measurement. d) Magnetic field calculated from the magnetization pattern.

perpendicularly magnetized thin film sample ($\vec{M} = M_z\vec{e}_z$) in which the magnetization is homogeneous throughout the film thickness ($M_z = M_z(x,y)$). Regions, where tip and sample magnetization are parallel are imaged as black and regions where tip and sample magnetization are antiparallel are imaged as white. The magnetization pattern can then simply be determined by applying a discrimination procedure to the image (figure 4.3). The magnetic field distribution and σ_{tip} can be calculated from this magnetization image using equation 2.24:

$$\vec{H}_{\text{sample}}(\vec{k}_{||}, z) = -\frac{\nabla}{k_{||}}\frac{(1-e^{-k_{||}d})}{2}\frac{e^{-k_{||}z}}{}\frac{1}{k_{||}}\begin{pmatrix} -ik_x \\ -ik_y \\ k_{||} \end{pmatrix} \cdot \vec{M}(\vec{k}_{||}) \tag{4.3}$$

A similar calibration procedure has been proposed by van Schendel et al. [16, 40][3].

These conditions are satisfied for the two different reference samples used here: Cu/Ni/Cu and CAMST.

Cu/Ni/Cu sample
This sample contains three different layers deposited on a Si(100) substrate: a Cu buffer layer of 200 nm film thickness, a Ni layer of 8 nm thickness, and a Cu capping layer of 5 nm thickness. The shape anisotropy of the thin film is overcome by the strong perpendicular interface and magnetoelastic anisotropy induced at the interface between Cu and Ni. The total perpendicular anisotropy of the sample depends on the Ni film thickness and is largest for a film thickness of about 7 nm. The saturation magnetization of Ni is 480 kA/m [86]. The domain size is about 1 μm. Further details of this sample can be found in references [3, 87, 88].

CAMST sample
The CAMST sample consists of 20 $Co_{50}Ni_{50}$ alloy and Pt bilayers. The thickness of the $Co_{50}Ni_{50}$ alloy layers is 0.55 nm and the thickness of the Pt layers is 1.2 nm. The total magnetic layer thickness is 35 nm. This sample has been used as a test sample for MFM imaging by many different groups. The smallest magnetic domains on this sample have a diameter of only about

[3]The main difference between the calibration procedure used here and the one used in the given references is that in the references, a new magnetization pattern was created with the results of the tip calibration. Using this new magnetization pattern, the calibration procedure was repeated. This process was iterated four times. Here, no iterations were applied.

10 nm. This sample generates a much stronger magnetic field than the Cu/Ni/Cu sample. The saturation magnetization of the multilayer is 300 kA/m. Further details of this sample can be found in reference [73].

All MFM images were measured on these two samples in dynamic constant height mode (chapter 2.4).
In order to evaluate the sample stray field at the position of the tip, and to apply the calibration procedure, the distance to the sample during imaging has to be known precisely. The magnetic field depends exponentially on the tip-sample distance, therefore a precise measurement of this distance is crucial for a precise tip calibration. The measurement of the distance to the sample surface is perturbed by the piezo-electric creep effect and by drift due to temperature changes. In order to reduce drift, the measurement should be done as quickly as possible, in order to reduce creep, the measurement should be done as slowly as possible. In order to minimize the effects of drift and creep, the position of the sample was measured here during one minute. Imaging was typically carried out at a minimal tip-sample distance of about 20 nm. The results are presented together with the results of the calibration procedure in the remainder of this chapter.

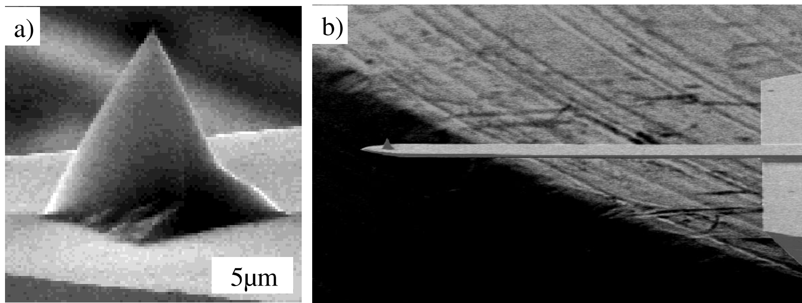

Figure 4.4: Scanning electron microscope (SEM) image of a Nanosensor tip a) sideview of the pyramidal tip b) cantilever with tip

4.3 Calibration of ultralow strayfield tips

In this chapter, tips that generate small magnetic fields are presented. Two ways of producing ultralow strayfield tips have been investigated: First, the tips coated with Fe were tested. The minimal Fe layer thickness at which the imaging properties of the tips were still satisfactory was investigated. Second, the use of a thin Ni coating was investigated. Ni has a lower saturation magnetization ($M_S = 480$ kA/m [86]) than Fe ($M_S = 1710$ kA/m [86]) and therefore generates a smaller magnetic field. All tips characterized in this chapter are Nanosensors[4] provided by Nanosensors, Wetzlar, Germany. A scanning electron microscopy image of a Nanosensor tip is shown in figure 4.4. These tips have a pyramidal shape because they are produced by an anisotropic etching technique.

4.3.1 Iron coated tips

First tips coated with Fe of different film thicknesses will be discussed. Four tips were prepared (table 4.1). The thickness of the iron layer deposited on the tips ranges from 1.3 nm to 2.2 nm.

[4] The trade name of these tips is “pointprobe contact mode cantilevers”.

tip name	layer thickness [nm]	force sensitivity $f_0/(2c_L)$ [kHz/(N/m)]
Fe-2.2	2.2	52.0
Fe-2.1	2.1	51.0
Fe-1.7	1.7	47.3
Fe-1.3	1.3	47.3

Table 4.1: Properties of the Nanosensor tips coated with thin Fe layers in UHV.

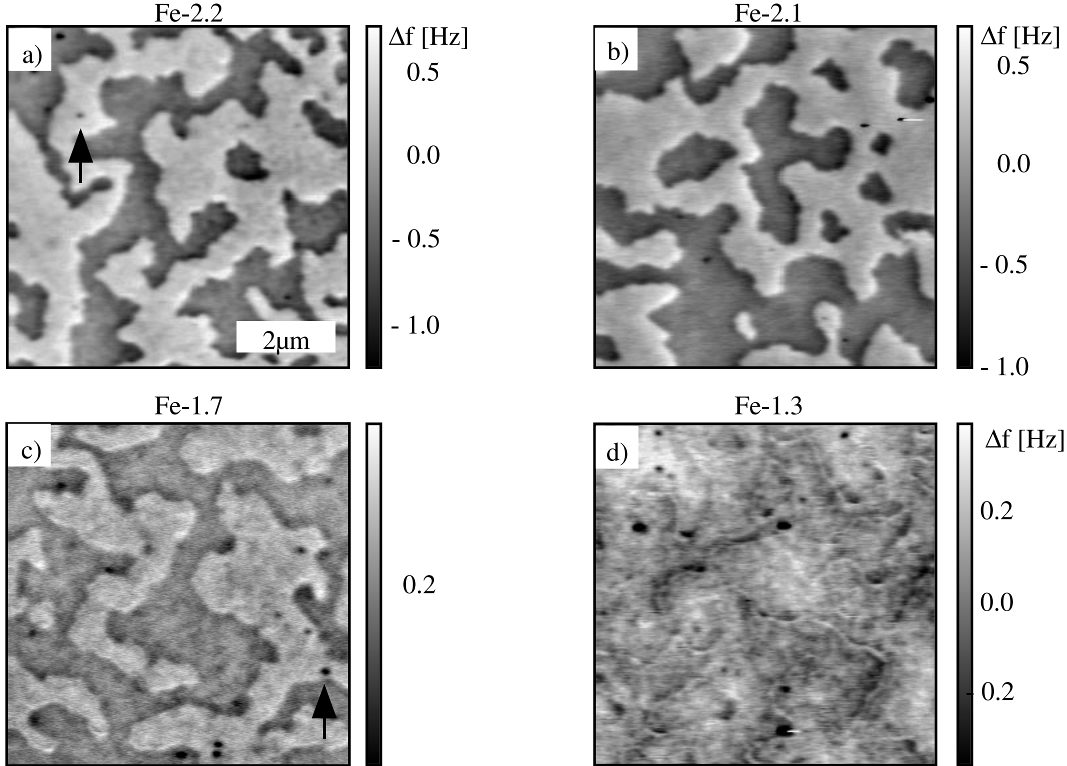

Figure 4.5: Images of the Cu/Ni/Cu sample obtained with Nanosensor tips coated with different thicknesses of Fe: a) Fe-2.2 b) Fe-2.1 c) Fe-1.7 and d) Fe-1.3

Each tip is labelled according to the thickness of Fe deposited on it. The force sensitivities of the four iron coated tips are similar[5].
With each of these tips, an image of the same size was measured on the Cu/Ni/Cu sample with an oscillation amplitude of 10 nm. These images are shown in figure 4.5. Image 4.5 a) shows the perpendicular domains on our Cu/Ni/Cu reference sample imaged by the Fe-2.2 tip. In the simplest picture, black contrast (attractive force) corresponds to domains pointing in the sample plane, while white contrast (repulsive force) corresponds to domains pointing out of the sample plane (or vice versa).
At the location of the domain walls, depending on the orientation of the domain wall, dark or bright contrast is observed. A similar dependence of the domain wall contrast on the domain

[5]The force sensitivities are important in order to compare the frequency shift read from the images measured with different cantilevers. The force sensitivity is needed to convert the force gradient to frequency shift, see equation 2.8.

wall orientation was observed by van Schendel and could be explained by the cantilever canting relative to the surface. The observed images are similar to the measurements obtained with tips coated under high vacuum conditions (see for example [40]). Image 4.5 b), obtained with the Fe-2.1 tip, shows a similar, but weaker contrast. Isolated black points in the images are topographical artefacts. Some of these artefacts are marked by arrows.
In image 4.5 c) (tip Fe-1.7) the topographical influence becomes large and the magnetic contrast decreases further. In image 4.5 d) (tip Fe-1.3) the topographical contrast is stronger than the magnetic contrast. Weak line-shaped features are visible in the image. The shape of these features is similar to the shape of the domain walls observed in the other images. Therefore, we believe that they are of magnetic origin. This tip is not useful for magnetic imaging.
In conclusion, the measured frequency shift decreases strongly with decreasing thickness of the Fe film. This will now be analysed in a more quantitative way using transfer function theory.

Calibration

The tips Fe-2.2, Fe-2.1 and Fe-1.7 have been calibrated and $\sigma_{\text{tip}}(\vec{k_{||}})$ has been calculated using formula 4.2. For the tip Fe-1.3, calibration was impossible. With the tips Fe-2.2 and Fe-2.1, four images have been measured, and $\sigma_{\text{tip}}(\vec{k_{||}})$ has been obtained from each of these images. Then the average of these four functions was taken for each tip. The calculation of $\sigma_{\text{tip}}(\vec{k_{||}})$ for the tip Fe-1.7 is based on only one image. $\sigma_{\text{tip}}(\vec{k_{||}})$ is represented here after taking its amplitude and then averaging over constant $k_{||}$ (figure 4.6). This circular average is plotted here on a double logarithmic scale for the three Fe coated tips.

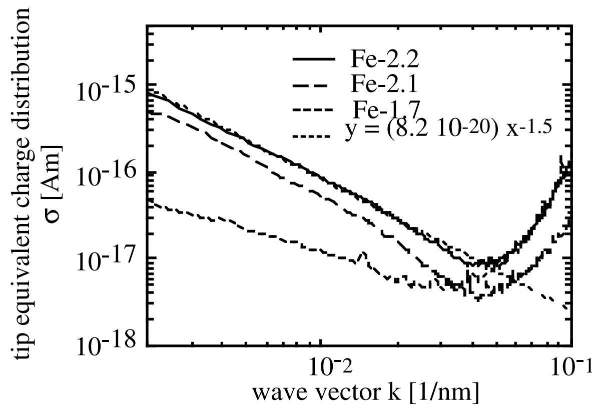

Figure 4.6: σ_{tip} obtained from calibration for the tips Fe-2.2, Fe-2.1 and Fe-1.7. The black arrows mark topographic artefacts.

For all tips, the frequency shift measured by the tip decays with increasing wavevector (decreasing domain size). For large wave vectors $\sigma(k_{||})$ increases again. In this wave vector range, the signal to noise ratio of the measurement is unfavorable[6]. The noise at these short wavelengths is enhanced by the calibration procedure. The value obtained for $\sigma(k_{||})$ in this region is not significant, as the standard deviation (not shown here) obtained from the averaging procedure over the four $\sigma(k_{||})$ obtained from the four measured images and the mean value of the averaging procedure have nearly the same value.
The functional dependence of $\sigma(k_{||})$ in the significant region (below the critical wavevector - see below) is similar for all Nanosensor tips used and can be fitted by a power law. In figure 4.6 the

[6]The signal to noise ratio of the measurement as a function of wave vector $\sigma(k_{||})$ will be shown in section 4.5.

power law describing the tip Fe-2.2 is plotted. The exponent found here, -1.5, is the same as for the tips coated in high vacuum by van Schendel et al. [16, 40]. $\sigma(k_{||})$ of lever Fe-1.7 also decays with a power law as a function of wavevector but with a smaller absolute value of the exponent than the other two tips. This could be due to the influence of topographic artefacts and noise or due to a difference in the magnetic properties, relative to the other tips, of a film with such a small thickness.
We define the critical wavelength of a tip as the wavelength where the frequency shift measured by the cantilever is $\sqrt{2}$ times as strong as the noise. The noise is given by the standard deviation of the averaging procedure over the four different $\sigma(\vec{k}_{||})$ functions calculated from four different images. Thus, the critical wavelength can be determined from $\sigma(\vec{k}_{||})$ and from its standard deviation. For the tips Fe-2.2 and Fe-2.1 a value of 160 nm was found, while for the tip Fe-1.7 it is 210 nm[7].

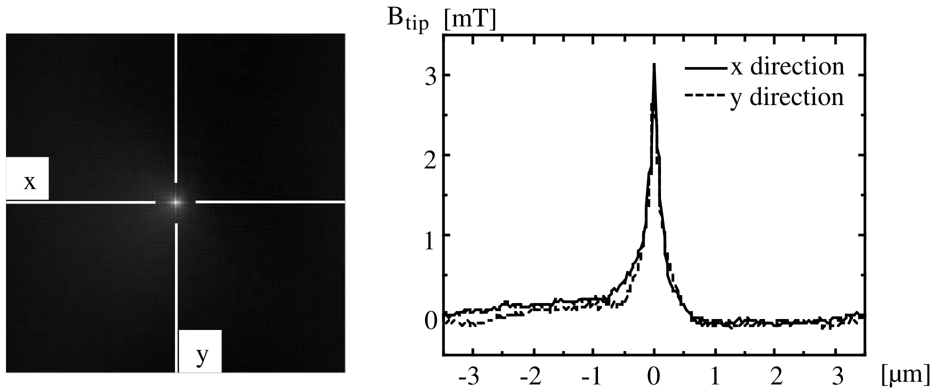

Figure 4.7: Magnetic field distribution in a plane through the tip apex for the tip Fe-2.2. The full width at half maximum is about 200 nm.

Magnetic field generated by the tips

From $\sigma(\vec{k}_{||})$, we can calculate the magnetic field generated by the tip (equation 2.23) in direct space using equation 2.23:

$$\vec{H}_{\mathrm{tip}}(\vec{k}_{||}, z) = -\frac{1}{2}\begin{pmatrix} ik_x \\ ik_y \\ k_{||} \end{pmatrix} \cdot \frac{1}{k_{||}} e^{-k_{||}z'} \cdot \sigma_{\mathrm{tip}}(\vec{k}_{||}) \tag{4.4}$$

The tip stray field distribution in a plane touching the tip end is shown in figure 4.7 for the tip Fe-2.2. The maximal magnetic field generated by the tip is 3 mT, the full width at half maximum is 200 nm. The shape of the tip stray field distribution resembles the one obtained by van Schendel et al. [16, 40] as well as the one obtained by Ferrier et al. [80] using electron tomography and by Streblechenko et al. [79] using electron holography. It is asymmetric in the x and in the y direction probably due to the canting of the pyramidal facets of the tip. The maximum tip stray fields obtained for all Fe tips are shown in figure 4.8.

[7] $\sigma(k_{||})$ for the tip Fe-1.7 was calculated from only one image and the standard deviation is therefore not defined. For this tip, it was assumed that the critical wavelength occurs at the same position relative to the minimum of $\sigma(k_{||})$ as for the other tips.

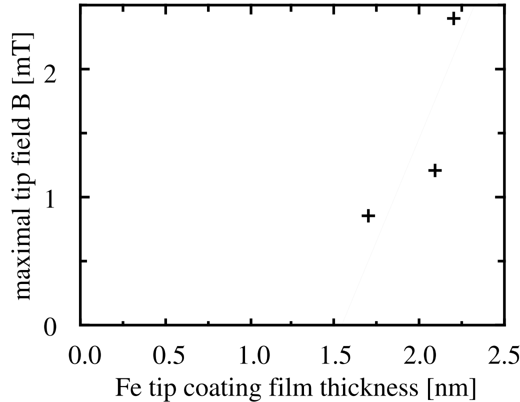

Figure 4.8: Maximal magnetic field generated by the tip at the position of the tip apex as a function of Fe film thickness for three Fe coated tips, Fe-2.2, Fe-2.1 and Fe-1.7. The straight line serves as a guide for the eye to determine the film thickness, where the magnetic field generated by the tip should vanish.

Similar to the measured contrast and $\sigma(k_{||})$, the maximum magnetic field also depends on the thickness of the iron coating. The maximum stray fields generated by the three calibrated tips are shown in figure 4.8. If one extrapolates the trend from these three tips (the line in figure 4.8), the magnetic field generated by the tips vanishes for an Fe coating of a thickness of about 1.3 nm. This is in agreement with the small magnetic contrast observed using the tip coated with 1.3 nm of iron, Fe-1.3 (table 4.1, figure 4.5). It implies that below about 1.3 nm film thickness, the Fe layer is magnetically soft or non-magnetic. It is possible that such layers are not continuous, and therefore have a reduced Curie temperature, or that Fe is in a different oxidation state, for example due to interaction with the SiO substrate, and therefore has antiferromagnetic or ferrimagnetic properties.
In chapter 3 we discussed measurements on a Ag/Fe/Ag sandwich. These Fe films have a coercive field of less than 1 mT. From the analysis of tips coated with thin Fe layers shown in this paragraph, it is clear that preparing a magnetic tip generating a magnetic field smaller than 1 mT is difficult, if iron is deposited on the tip. To do this, between 1.3 and 1.7 nm of iron should be deposited on the tip. If there is some variance in the growth mode of this Fe layer on the tip, for example due to nucleation of grains at arbitrarily distributed nucleation sites, these iron coated tips may not be reproducible. As an alternative, tips coated with a material with lower saturation magnetization, Ni, were studied. For Ni, a larger film thickness can be chosen for the same magnetic field than with a Fe layer. However, before we show the studies of Ni coated tips, the question is addressed whether tip equivalent charge distributions obtained from calibrations using different image sizes and using images obtained on different test samples are similar to each other. This will be discussed in the following paragraph.

4.3.2 Comparison of tip equivalent charge distributions obtained using different image sizes and using images obtained on different test samples

So far, all MFM measurements used for tip calibrations were performed using the same image size, 7 μm, and the same test sample, the Cu/Ni/Cu sandwich, for all cantilevers. However the tip equivalent charge distribution obtained from calibration should be independent of the image size and of the test sample. In order to check whether the tip equivalent charge distribution is in practice independent of the test sample and the image size, the same tip was calibrated on two different samples, the CAMST sample and the Cu/Ni/Cu sample. For the calibration done on the CAMST sample, two different image sizes were used, 1 μm and 3.5 μm. The image size used on the Cu/Ni/Cu sample was the same as for the other Fe levers calibrated (7 μm). The

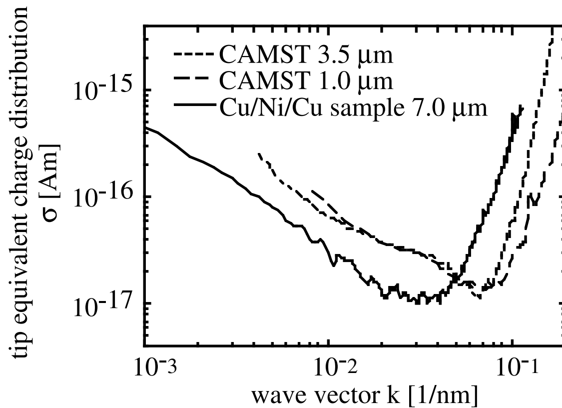

Figure 4.9: $\sigma_{\rm tip}$ obtained from calibration for an iron tip calibrated on two different samples, the Cu/Ni/Cu sample and the CAMST sample, using in total three different image sizes.

results are shown in figure 4.9.

The two tip equivalent charge distributions obtained on the CAMST sample with different image sizes are discussed first. Both $\sigma_{\rm tip}$ functions obtained on the CAMST sample show the same values, although the critical wavelength obtained from the measurements with the smaller image size is slightly smaller than the one with the larger image size. For a certain wavevector, $\sigma_{\rm tip}$ should be independent of the image size. The observation that the critical wavelength is larger for the image acquired with a larger size, can be explained by the larger scanning speed used for acquiring the larger image: even though the scanning speed in pixel/s was the same for the two images, this translates to a larger scanning speed in nm/s for the larger image, and therefore to more noise.

Now the differences between the $\sigma_{\rm tip}$ functions obtained on the two different test samples will be discussed. $\sigma_{\rm tip}$ obtained on the Cu/Ni/Cu sample is about 2.5 times smaller than $\sigma_{\rm tip}$ obtained on the CAMST sample. The critical wavelength obtained on the Cu/Ni/Cu sample is about a factor of 2 larger than the critical wavelength obtained on the CAMST sample. For a certain wavevector, $\sigma_{\rm tip}$ should be independent of the test sample used. The difference in critical wavelength can be explained by the same argument as the slight difference in the critical wavelength obtained for the two different image sizes on the CAMST sample. In addition, the signal to noise ratio is smaller for larger wavevectors, because the density of large wave vectors contained in the MFM image of the Cu/Ni/Cu sample is smaller due to the larger domain size.

The different absolute value of $\sigma_{\rm tip}$ obtained for the two different test samples must be due to a systematic error. An error in the magnetization, in the thickness of the magnetic layer or in the tip sample distance of the MFM images used for the calibration procedure may be causes for the large differences in magnitude of $\sigma_{\rm tip}$. Another possible reason for the difference in $\sigma_{\rm tip}$ obtained from calibration on the two test samples is that the tip changed during the course of the experiments. For example, the tip could have been damaged in the course of the measurement on the CAMST sample. However, a similar difference between $\sigma_{\rm tip}$ functions obtained on the Cu/Ni/Cu and the CAMST sample was obtained for an ultrasharp tip and will be discussed in paragraph 4.4. The tip could also have been changed by the magnetic field generated by the CAMST sample. The CAMST sample is in a magnetized state, and generates an attractive background field. Possibly the magnetic charge distribution at the tip apex is influenced by this field.

tip name	layer thickness [nm]	force sensitivity $f_0/(2c_L)$ [kHz/(N/m)]
Ni-9.6	9.6	36.3
Ni-7.1	7.1	36.3
Ni-5.1	5.1	34.8
Ni-4.5	4.5	36.3

Table 4.2: Nanosensor tips coated with thin Ni layers in UHV.

4.3.3 Nickel coated tips

To obtain tips with an even smaller magnetic field generated at the position of the tip apex, Nanosensors were coated with a thin Ni film in UHV using the procedure described in chapter 4.2.1. Their properties are summarized in table 4.2.
The thickness of the Ni film deposited on the tips is much larger than the thickness of the Fe film. The amount of Ni needed to obtain the same frequency shift was expected to be about 4 times larger, because the saturation magnetization is four times smaller than the saturation magnetization of Fe. The validity of this assumption can be tested later by analysing the tip equivalent charge distribution obtained from these tips. Their force sensitivities $f_0/2c_L$ are similar to each other but smaller than the force sensitivities of the Fe tips[8]. The frequency shift obtained from these measurements will therefore be smaller for the same force gradient as for the Fe tips.
Images were acquired on the Cu/Ni/Cu reference sample with all four Ni coated tips. The amplitude of the cantilever oscillation was about 45 nm. The images obtained are shown in figure 4.10. Note that the image size (14 μm) is not the same as the size of the images measured with Fe tips (7 μm).
While image 4.10 a) resembles the images obtained with Fe tips, the other three images show a different kind of contrast. For example in image 4.10 d), the contrast seems to have a maximum near a domain wall, the region of the domain wall itself appears as a minimum, and then the contrast is maximal again in the opposite domain near the domain wall, and then decreases to a minimum near the next domain wall. This can be seen even more clearly in the line section shown (figure 4.10f)). The appearance of the perpendicular domains on the Cu/Ni/Cu test sample is different for all three images 4.10 b), c) and d). In these three images, within each domain, the contrast is generally not constant within a domain like in the images measured with Fe coated tips. The magnitude of the detected frequency shift decreases with decreasing Ni thickness similar to Fe coated tips.
The domain wall contrast cannot be explained by the cantilever canting as there is an asymmetry not only in y direction, the direction of the cantilever canting, but also in the x direction. It is, however, possible that the magnetization within the tip is canted with respect to the axis of the tip. The tip Ni-5.1 was magnetized with a stronger magnetic field (6 T using a superconducting magnet) than usual (0.4 T) in order to overcome the coercive field even if it is much larger than expected for example due to magnetic vortices. This did not change the imaging properties of the tip. A canted magnetic structure does not affect the applicability of transfer function theory. Another potential explanation for the observed contrast is the modification of the tip under the

[8]They were taken from a different batch. Note also that the oscillation amplitude used for the Ni tips is not the same as for the Fe tips. This changes the frequency shift obtained from the measurement and has been taken into account in the calibration procedure.

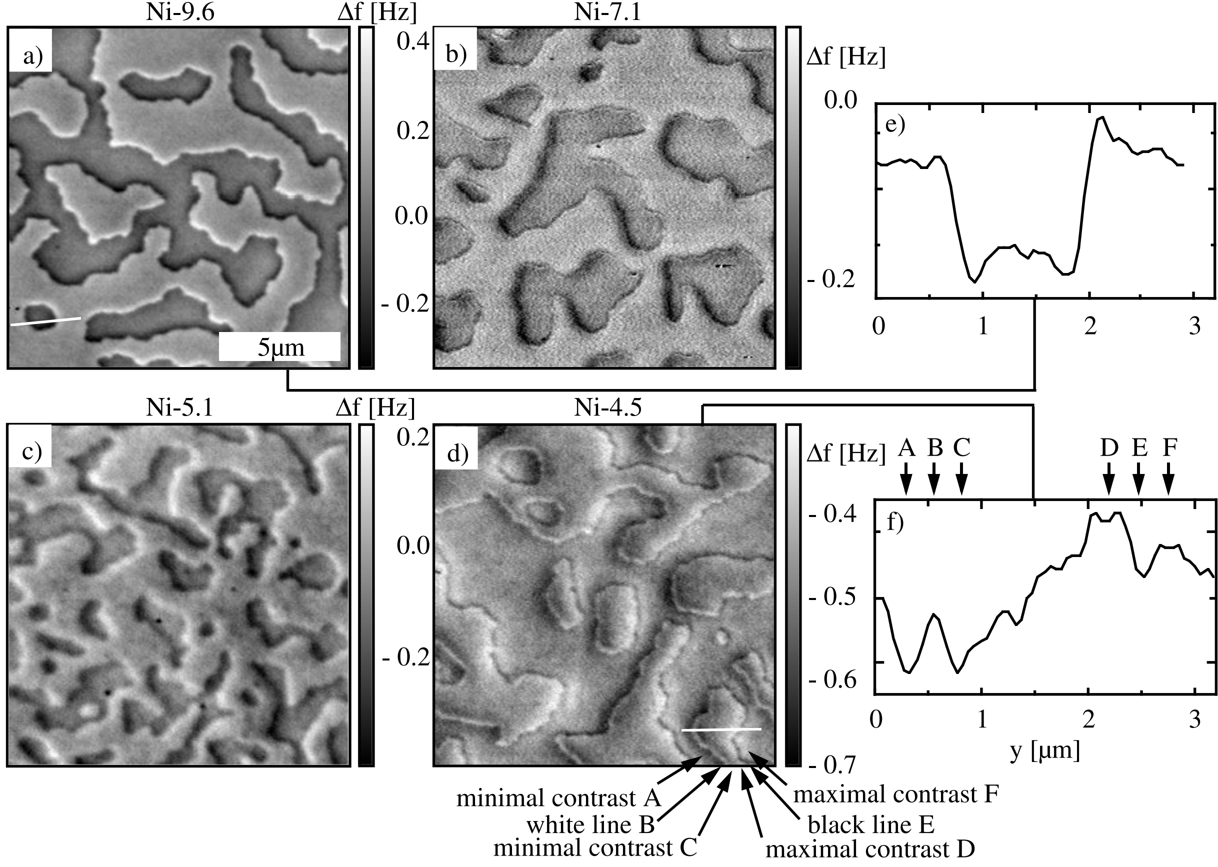

Figure 4.10: Images of the Cu/Ni/Cu sample acquired with Nanosensor tips coated with different thicknesses of Ni: a) Ni-9.6 b) Ni-7.1 c) Ni-5.1 and d) Ni-4.5. A line section is shown for the Ni-9.6 tip in e) and for the Ni-4.5 tip in f).

influence of the sample stray field. The black and white lines observed near the domain walls could be a sign of modification of the tip magnetization by the sample, as the sample stray field is strongest at the position of the domain walls. As mentioned in chapter 2.7.5, the distance dependence of the frequency shift can be used to test whether there is mutual modification of the tip and the sample. Therefore, we carefully analysed the distance dependence of the frequency shift for these tips.

Distance dependence of the frequency shift measured with Ni coated tips

In chapter 2.7.5, a technique for determining the relative distance between two images obtained with the same tip at the same lateral position on the sample was described. It was shown that (equation 2.29)

$$\frac{< \Delta f(\vec{k_{\|}}, z_i) >}{< \Delta f(\vec{k_{\|}}, z_1) >} = e^{-k_{\|}(z_i - z_1)} \tag{4.5}$$

where $< \ldots >$ is the average over constant $k_{\|}$, $i = 1$ to n indicates the image numbers where image 1 is the reference image. From these normalized spectra the relative distances $d_i = z_i - z_1$

tip name	ratio	magnetic properties
Ni-9.6	1.34	hard?
Ni-7.1	1.54	soft
Ni-5.1	1.40	soft
Ni-4.5	1.19	hard?
Fe-3.2	0.88	hard

Table 4.3: Ratio between the distance to the surface obtained from the frequency shift using transfer function theory (as explained in the text, $\Delta z_{\Delta f(k)}$) and the measured distance (Δz_{piezo}) for all Ni coated tips and an Fe-3.2 tip for comparison. For the Ni-7.1 and the Ni-5.1 tip strong deviations from the expected ratio of 1 suggest that the Ni coating is magnetically soft.

can be obtained. This relative distance will be called $\Delta z_{\Delta f(k)}$ in the following. This equation is only valid if mutual modification is negligible. Consequently, equation 4.5 can be considered as a criterion for negligible modification of the tip and the sample. In order to do this, the theoretical relative distance between two images will be compared to the measured distance (Δz_{piezo}) for the four Ni tips, as well as for a tip coated with 3.2 nm of Fe for comparison (figure 4.11 and table 4.3.3).

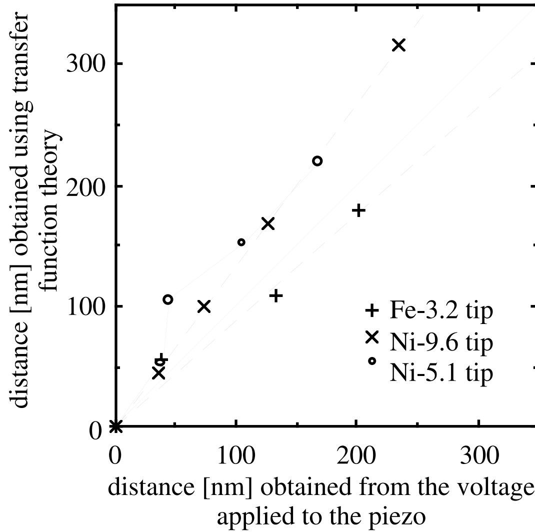

Figure 4.11: The distance $\Delta z_{\Delta f(k)}$ obtained from the measured frequency shift as a function of the distance Δz_{piezo} obtained from the voltage applied to the piezo is plotted for an Fe-3.2 tip, the Ni-9.6 tip and the Ni-5.1. The two dashed lines are fits of the data to a straight line passing through the origin. The solid line is the curve $y = x$ which corresponds to a measurement without errors for a tip with no modification.

Figure 4.11 shows the data obtained for the Ni-9.6, the Ni-5.1 tip and a Fe-3.2 tip. While the data from the Ni-9.6 tip and the Fe-3.2 tip follow straight lines (dashed lines), the deviations from a straight line are large (more than 50%) for the Ni-5.1 tip. These deviations (figure 4.11) are too large to be explained by the experimental error in the distance determination (up to about 35%), but are possibly due to a modification of the magnetic state of the tip in the field of the sample. The other two Ni tips (Ni-7.1 and Ni-4.5) also follow straight lines (data not displayed in the graph). For all tips, the slope of the best fit is displayed in table 4.3.3.
For the tip Ni-7.1, the slope of the best fit deviates strongly from the value of 1 suggested by transfer function theory. This is a sign of mutual modification of the tip and sample. Within the experimental error of the measured distance Δz_{piezo}, the theoretical distance dependence is fulfilled for tip Ni-9.6, for Ni-4.5 as well as for tip Fe-3.2. However, the deviation from the optimal ratio 1 is large (34%) although it is smaller than the experimental error of 35%. A small mutual modification cannot be ruled out for the tip Ni-9.6. A method for distance determination with a higher precision should be used, for example frequency versus distance or A_{exc} versus distance measurements. Assuming that the distance dependence measured for the Ni-9.6 tip can be explained by experimental errors, this tip will be calibrated.

Calibration

As mentioned previously, for the application of the transfer function theory, mutual modification has to be ruled out, but it is not important in which direction the magnetization of the tip points. Therefore, in principle, tips Ni-9.6 and Ni-4.5 can be calibrated. However, it is more difficult to create magnetization images from the images measured with the Ni-4.5 than from the images measured with Fe tips and with tip Ni-9.6 as applying a simple discrimination procedure to the images measured with tip Ni-4.5 (figure 4.10d)) does not create good magnetization images. However, this problem does not occur for the tip Ni-9.6, therefore only this tip can be calibrated. Four images have been measured with tip Ni-9.6 on different positions on the Cu/Ni/Cu sample using an oscillation amplitude of 45 nm.

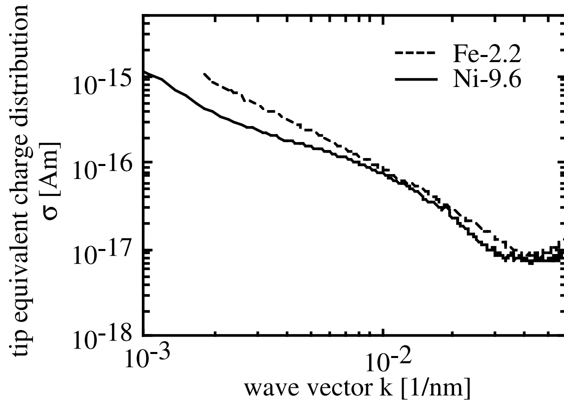

Figure 4.12: σ_{tip} obtained from the calibration of tip Ni-9.6 compared to that of tip Fe-2.2.

Similar to the procedure used for the iron tips, $\sigma(\vec{k}_{||})$ has been determined from each of the measured images, and after calculating the average over the four two-dimensional functions obtained, the circular average over constant $k_{||}$ was calculated. It is shown in figure 4.12. The data is compared to that of tip Fe-2.2. Although the σ_{tip} functions of the two tips have been obtained on images of a different size, the general features of the two σ_{tip} functions are similar. The critical wavelength of the Ni-9.6 tip is slightly larger (180 nm) than the critical wavelength of the Fe-2.2 tip (160 nm), but the magnitude of $\sigma(k_{||})$ is comparable. This can also be checked by comparing the frequency shift difference between the parallel and antiparallel domains of tip Ni-9.6 to the frequency shift difference of tip Fe-2.2 (see image 4.10a) for the Ni-9.6 tip and image 4.5a) for the Fe-2.2 tip). Both frequency shift differences are similar.

Magnetic field generated by the tip

The magnitude and spacial distribution of the magnetic field generated by tip Ni-9.6 is similar to the magnetic field generated by tip Fe-2.2. The maximum tip stray field calculated from the tip equivalent charge distribution of the Ni-9.6 tip ($B_{\text{max tip}} = 1.7$ mT) is slightly smaller than the magnetic field generated by the Fe-2.2 tip ($B_{\text{max tip}} = 2.4$ mT) in agreement with the initial assumption that the magnetic field generated should be roughly proportional to the saturation magnetization of the material deposited on the tip. The extension of the magnetic field generated by the tip is 200 nm at half of the maximum value of the tip field. It is similar to the extension of the field generated by the Fe-2.2 tip. The spatial distribution of the magnetic field generated by the tip strongly depends on the filter applied to the tip image. The stray field distributions

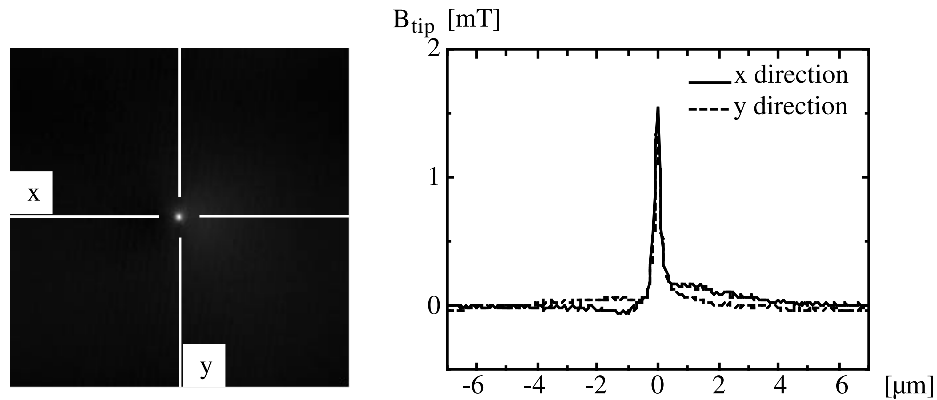

Figure 4.13: Magnetic field distribution in a plane through the tip apex for the tip Ni-9.6. The full width at half the maximum is about 200 nm.

of all tips shown here have been filtered using the same type of filter and the same filtering wavevector. The tip stray field shows an anisotropy different to that obtained for the Fe-2.2 tip. This probably reflects the tip facet canting or a canted magnetic state of the tip.

4.3.4 Conclusions

The imaging properties of the Fe coated tips are roughly proportional to the thickness of the Fe coating. The tip strength can be tuned in order to obtain a certain stray field generated by an Fe tip. No signs of modifications of magnetic state of the tip by the sample stray field are found down to Fe film thicknesses as small as 1.7 nm.
A tip coated with 9.6 nm of Ni can be used for imaging. It shows similar properties as a tip coated with 2.2 nm of Fe. Tips with smaller film thicknesses of Ni yielded distorted images. These distortions could be due to either a canted magnetization state or to a modification of the tip magnetization under the influence of the sample stray field. Ni tips can therefore not be recommended for measuring low coercive samples, as the image interpretation becomes difficult.

4.4 Ultrasharp tips

The second class of tips investigated are ultrasharp tips. From the study of the ultralow strayfield tips, we know that the critical wavelength of a typical Nanosensor tip is about 160 nm. In the study by van Schendel et al. [16, 40] a critical wavelength of 100 nm was obtained with a Nanosensor tip[9]. The purpose of this section is to investigate whether the critical wavelength can be further reduced by using sharper tips.
One attempt to make sharper tips was discussed in the previous chapter (chapter 3): High aspect ratio tips were prepared by electron beam induced deposition (EBID) of a carbon needle on the tip in a scanning electron microscope (SEM) [72]. This method relies on the breaking of C-C-bonds by irradiating a surface under a rest gas of organic molecules in a SEM. The rest gas was in our case not well controlled and therefore the production of EBID tips was not reproducible.

[9]The Nanosensor tip used by van Schendel was covered with 6.8 nm of Iron and the calibration was carried out using an iteration process based on the same method as described here, giving a more precise calibration than here. See also footnote 3 of this chapter.

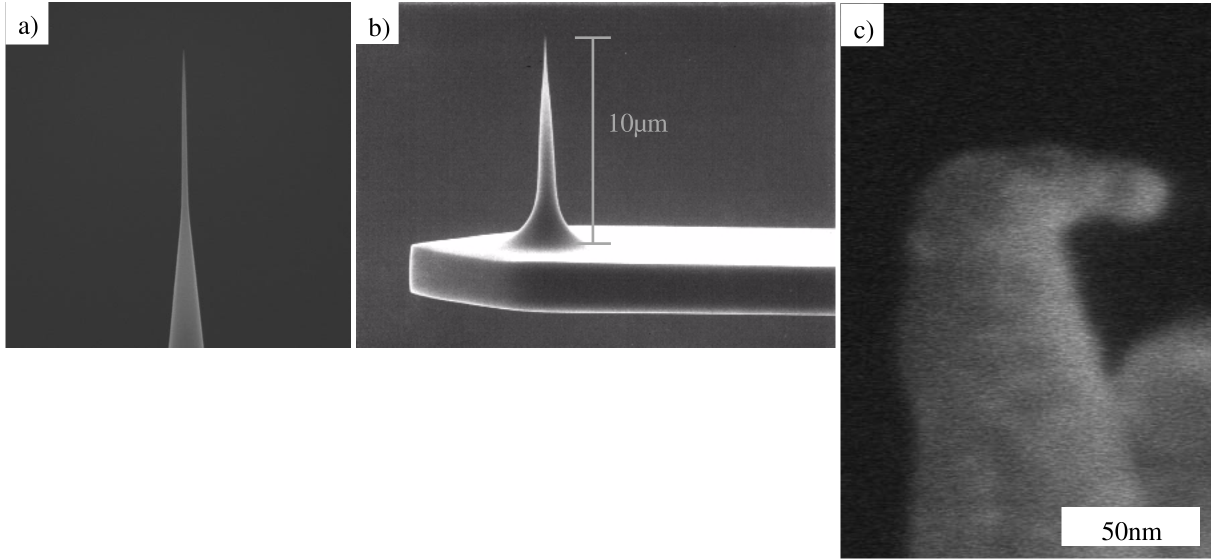

Figure 4.14: SEM image of an ultrasharp tip a), b) sideview of the cantilever with conical tip, c) SEM image obtained after imaging.

tip name	layer thickness [nm]	force sensitivity $f_0/(2c_L)$ [kHz/(N/m)]
us-2.9	2.9	20.4

Table 4.4: Ultrasharp tips coated with thin Fe layers in UHV.

The ultrasharp tips studied in this chapter were supplied by Team Nanotech, Villingen-Schwenningen, Germany. These tips are etched isotropically in contrast to the pyramidal Nanosensors. They have cone angles of less than 10 degrees and a tip radius of less than 10 nm. A SEM image of such a tip is shown in figure 4.14a) and b). The magnetic layers on these tips were prepared using the same procedure as for the Nanosensor tips. After finishing the experiments described in this section, the shape of the tip was checked again in the SEM (figure 4.14c)). The SEM images revealed that this tip was bent in the course of the experiments and the tip radius was broadened to about 25 nm. This could be due to a tip crash during the MFM measurements. However another ultrasharp tip that was imaged with the SEM directly after evaporation (before using it for MFM images) showed a similar broadening. The broadening could also be due to stress in the thin film resulting from the temperature of the tip and thin film during deposition and the difference in thermal expansion between the tip and deposited layers.

4.4.1 Calibration of an ultrasharp tip and comparison to a Nanosensor tip

The parameters of the ultrasharp tip used are shown in table 4.4. It was coated with a 2.9 nm thick Fe layer. The force sensitivity is smaller than that of the Nanosensor tips, because the cantilever length, width and thickness were not the same (see table 2.1 and equation 2.2). This means that the frequency shift will be smaller for the same force gradient compared to the Fe and Ni tips discussed above (see equation 2.8). Recently, the cantilever design has been changed for the purpose of magnetic force microscopy[10]. The ultrasharp tip was tested on the CAMST

[10]The trade name of these new tips is “supercone-MFM”.

and on the Cu/Ni/Cu sample. An image obtained on both test samples using an ultrasharp tip is shown in figure 4.15 along with the image shown in paragraph 4.3.1 obtained with the tip Fe-2.2.

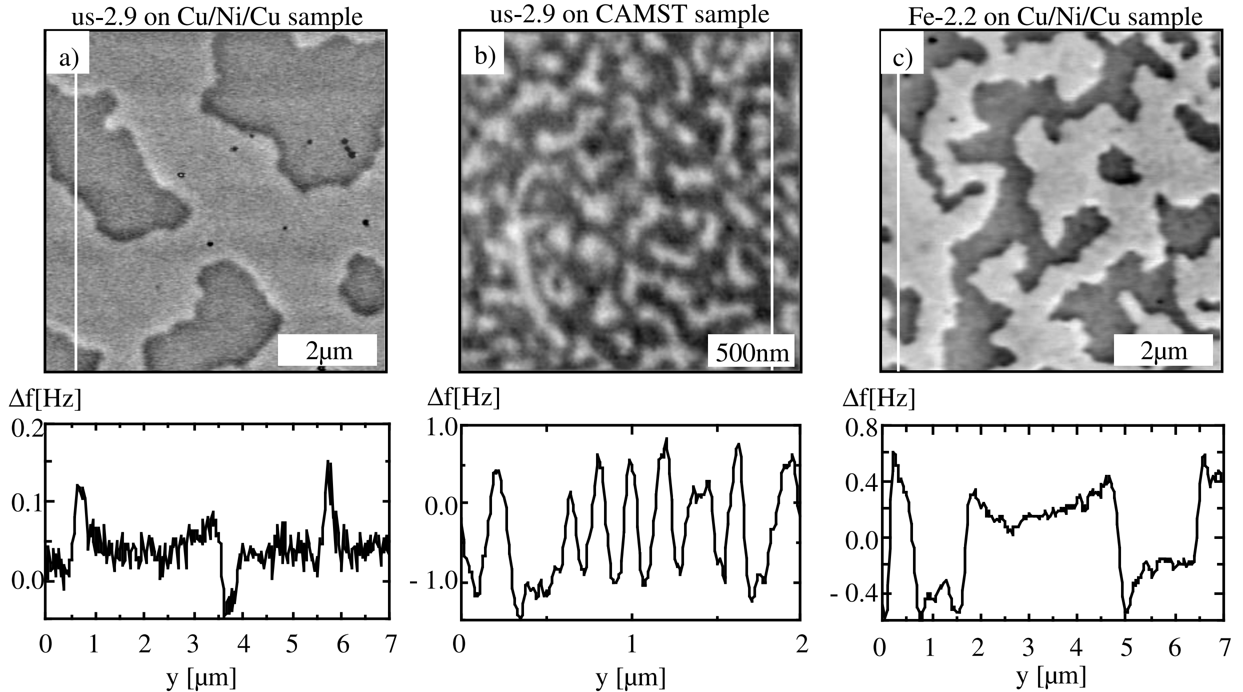

Figure 4.15: Comparison of two images obtained with an ultrasharp tip a) on the Cu/Ni/Cu sample and b) on the CAMST sample with c) an image obtained with a Nanosensor tip on the Cu/Ni/Cu sample. The black points in image a) are topographical artefacts.

The domains of the Cu/Ni/Cu test sample are imaged in a different way by the ultrasharp tip compared to a Nanosensor tip. In the centre of a domain the frequency shift is close to its mean value of the image, strong contrast is only observed near the domain walls. In other words, the frequency shift in the middle of an antiparallel domain is almost the same as in a parallel domain. This is typical for the magnetic field and the field derivative created by such a sample. With the Fe-2.2 tip, a frequency shift difference of at least 0.3 Hz is observed between two domains of opposite magnetization. As a MFM image obtained with a monopole tip in the dynamic mode is proportional to this field derivative, this tip can be regarded as more similar to a monopole than the other tips.

The images obtained on the CAMST sample do not show a frequency shift close to the mean value in the domain centre, probably because the domains are much smaller on this sample.

Considering the relatively thick layer of iron deposited on the tip (2.9 nm compared to 2.2 nm in the case of the Nanosensor), the frequency shift is small. Compared to the tip Fe-2.2 (figure 4.5a)), only 1/6 of the frequency shift is obtained across the domain walls. This can be explained by the different imaging properties of this tip and can be analysed in more detail using the tip equivalent charge distribution.

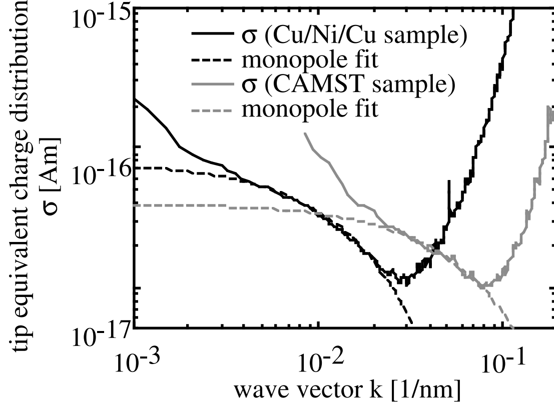

Figure 4.16: σ_{tip} of the ultrasharp tip obtained on the Cu/Ni/Cu and on the CAMST sample and corresponding fit to a monopole model.

Calibration

For calibration purposes, four images were measured on the Cu/Ni/Cu sample and two on the CAMST sample with an oscillation amplitude of 10 nm. $\sigma(k_{||})$ was calculated from each of these images and the average of the results was calculated separately for the measurements on the Cu/Ni/Cu sample and the measurements on the CAMST sample. The tip equivalent charge distributions $\sigma(k_{||})$ of the ultrasharp tip are shown in figure 4.16. They show the same general features as described above for the Nanosensor tips: The frequency shift decays with increasing $k_{||}$ until the noise limit is reached and at even larger values of $k_{||}$ the noise is amplified and the σ_{tip} function is not significant.
σ_{tip} obtained on the CAMST sample is about 2.5 to 3 times stronger than the σ_{tip} obtained on the Cu/Ni/Cu sample. This is in agreement with the observation made for the Fe tip (section 4.3.2). It also shows a smaller critical wavelength. This demonstrates once again that it is important to use a small domain sample and small scale images in order to calibrate a sharp tip.

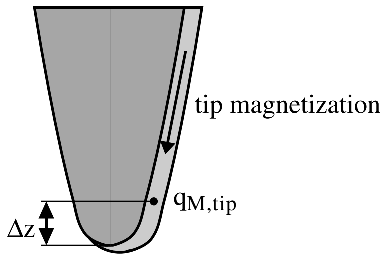

Figure 4.17: Model of a magnetic monopole tip with an additional distance of the magnetic charge to the surface.

Comparison of the ultrasharp tip to a monopole model

In section 2.7.2, the tip equivalent charge distribution of a monopole tip with additional distance Δz of the monopole to the tip apex (figure 4.17) was shown (equation 2.22):

$$\sigma(k_{||}) = q_{\text{M,tip}} e^{-k_{\|}\Delta z} \tag{4.6}$$

where $q_{\text{M,tip}}$ is the charge of the monopole. Previously, monopole models have been used in the literature in order to describe MFM tips. However, by analysing Nanosensor tips tested on Cu/Ni/Cu samples with different Ni thickness and therefore different domain size, Barwich [89]

found that the monopole strength $q_{\mathrm{M,tip}}$ and the additional distance Δz decrease strongly with decreasing domain size of the sample [89]. The reason is that the Fourier components of the sample magnetic field with small wavevectors (large domain sizes) decay more slowly ($\sim e^{-zk_{\|}}$) than the Fourier components with large wavevectors that this part of the magnetic field therefore interacts with a larger volume of the tip. The calculation of $\sigma(k_{||})$ by van Schendel [40] showed that $\sigma(k_{||})$ of a Nanosensor tip had a different functional dependence than the monopole model, and that the monopole model was therefore only suitable within a certain range of wavevectors. Furthermore, the additional distance $\Delta z = 125$ nm obtained by fitting was large. The images calculated from the monopole model did not well describe the contrast observed with the Nanosensor.

Compared to the Fe coated Nanosensor tip, $\sigma(k_{||})$ obtained with the ultrasharp tip on the Cu/Ni/Cu sample shows a different functional dependence. It resembles $\sigma(k_{||})$ of a monopole tip with an additional distance (model shown in chapter 2.7.2), and for large wave vectors exhibits a stronger decay than a power law (straight line in a log/log plot) for large wave vectors. This means that the frequency shift of the small wave vectors is larger than for the Nanosensor tip, and that at large vectors the frequency shift is smaller than for the Nanosensor tip. The functional dependence of $\sigma(k_{||})$ and the image contrast obtained motivates the comparison of this tip to a monopole model.

The monopole model has been fitted to $\sigma(k_{||})$, with the strength of the monopole $q_{\mathrm{M,tip}}$ and the additional distance Δz being the only two free parameters. The best fit was obtained with $q_{\mathrm{M,tip}} = 7.89 \cdot 10^{-17}$ Tm^2 and $\Delta z = 82.1$ nm for the Cu/Ni/Cu sample, and with $q_{\mathrm{M,tip}} = 3.99 \cdot 10^{-17}$ Tm^2 and $\Delta z = 18.0$ nm for the CAMST sample. The result is shown in figure 4.16. The additional distance obtained by fitting is significantly smaller than the value of 125 nm obtained for a Nanosensor tip coated in high vacuum by van Schendel [40]. This implies that the centre of the magnetic charge is closer to the topographical tip end for an ultrasharp tip than it is for a Nanosensor tip. The magnitude of the monopole charge can be compared with a simple model of a needle magnet with a certain size of the frontal area. The size of this frontal area is the product of the layer thickness and the tip radius (see also figure 2.11). With this assumption, a tip radius of about 13 nm is calculated for the calibration on the Cu/Ni/Cu sample, and a tip radius of 6.7 nm for the calibration on the CAMST sample.

The difference of the two fits obtained reflects the difference in the tip equivalent charge distribution obtained on the two samples. This is similar to the result found for the Nanosensor tip calibrated on both samples, discussed in paragraph 4.3.2. As in the case of the Nanosensor tip, $\sigma(k_{||})$ can only be described by a monopole model within a limited wavevector range. $\sigma(k_{||})$ obtained from the calibration procedure gives a more general description of the tip's imaging properties (see figure 4.16).

An important criterion to answer the question of whether the monopole model is a good description of the ultrasharp tip is to compare images calculated from the monopole models to the experimental results. The image created by a monopole tip is simply proportional to the field derivative and can be calculated using equation 2.24. These images are shown in figure 4.18. In both cases, the monopole model is suitable for describing the ultrasharp tip, in contrast to the Nanosensor tips prepared in high vacuum by van Schendel [40]. In conclusion the ultrasharp tip is better described by a monopole model than the Nanosensor tip, but $\sigma(k_{||})$ obtained from the calibration procedure gives a more general description of the tip's imaging properties.

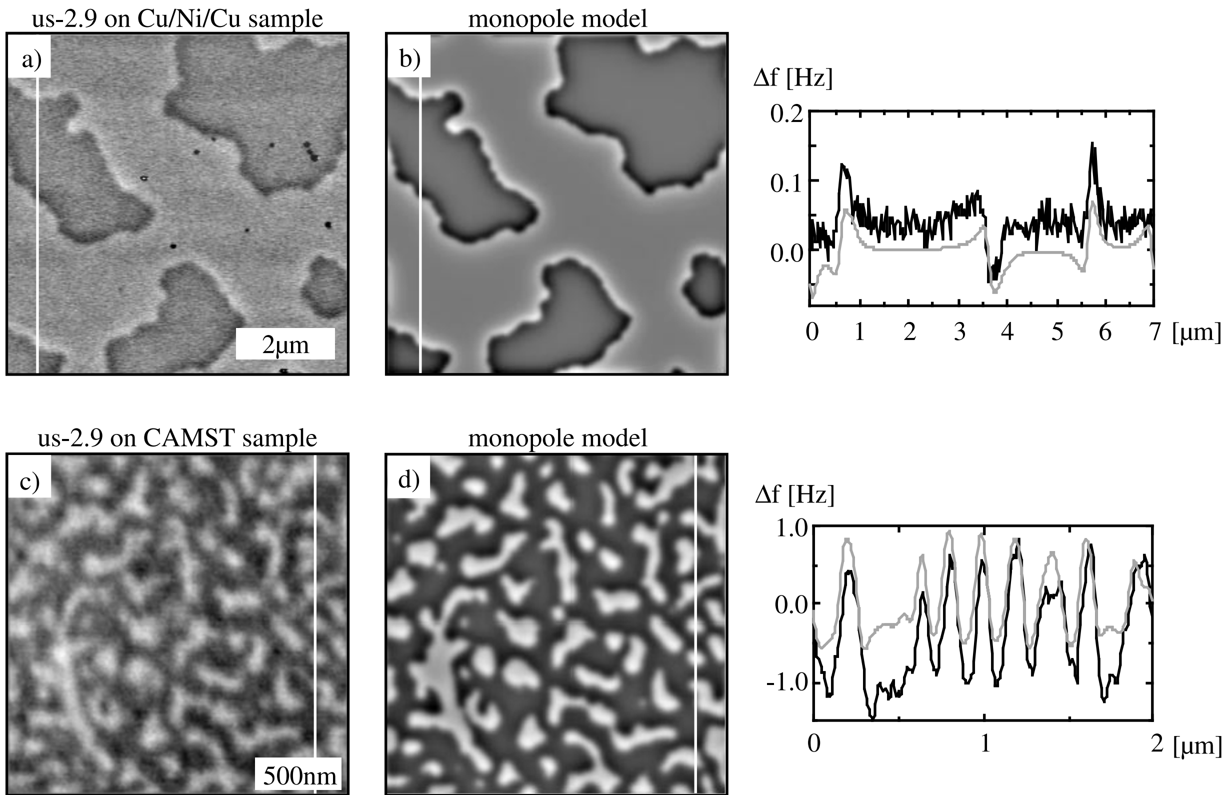

Figure 4.18: Images obtained with an ultrasharp tip compared with simulated images using a monopole model. a) Original image measured on the Cu/Ni/Cu sample b) simulated image c) Original image measured on the CAMST sample d) simulated image

Magnetic field generated by the tip

The tip stray field obtained by calibrating the us-2.9 tip on the Cu/Ni/Cu sample is shown in figure 4.19. The maximum tip stray field is small (1.75 mT) in comparison to the maximum tip stray field of 2.4 mT obtained with the Fe-2.2 tip, although the film thickness is larger[11]. The width of the tip stray field at half the maximum value of the stray field is 100 nm for the calibration done on the Cu/Ni/Cu sample, smaller than the value obtained for the Fe-2.2 tip (160 nm). The tip stray field obtained is also more symmetric than the Nanosensor's tip stray field. This reflects the circular symmetry of the ultrasharp tip.

4.4.2 Conclusions

Although the ultrasharp tip was damaged during the evaporation process or during imaging, it still shows a smaller critical wavelength than the Nanosensor tips and the tip stray field is more confined than the tip stray field of the Nanosensor tip. The images produced by the ultrasharp tip are well described by a monopole model, underlining the sharpness of the ultrasharp tip.

[11] From the calibration of the us-2.9 tip on the CAMST sample, a tip stray field of 3.6 mT is obtained.

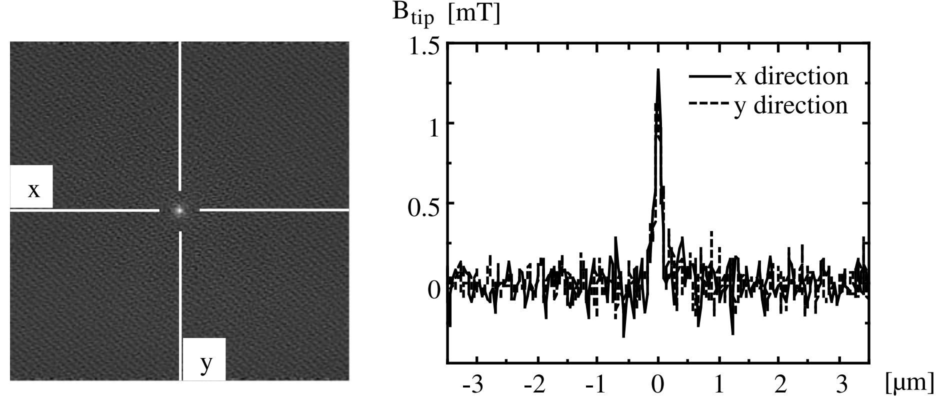

Figure 4.19: Magnetic field distribution in a plane through the tip apex for the ultrasharp tip. The full width at half maximum is about 100 nm.

4.5 Signal to noise ratio as a function of oscillation amplitude

Magnetic tips generating a small magnetic field which is necessary in order not to perturb low coercivity samples, were shown in the last section. However, as a side effect, the frequency shift measured by such a tip decreases. Also in the case of the ultrasharp tip the measured frequency shift was small for the thickness of its Fe coating. Therefore, special care has to be taken to improve the signal to noise ratio. It will be shown experimentally that one way of improving the signal to noise ratio is to use large amplitudes.

In all tip calibration studies carried out in our group before this thesis, the amplitude during MFM measurements was chosen to fulfil the small amplitude approximation in order to facilitate quantitative analysis[12]. However, with such a small amplitude the signal to noise ratio is not optimal. The noise [30] (equation 2.10)

$$\delta f_{\text{rms}} = \frac{1}{A_{\text{osc}}} \sqrt{\frac{k_B T b f_0}{\pi Q c_L}} \tag{4.7}$$

depends on $1/A_{\text{osc}}$ similar to the frequency shift [27] (equation 2.7):

$$f - f_0 = \Delta f = -\frac{f_0}{2\pi c_L A_{\text{osc}}} \int_{-\pi}^{\pi} F_n(\vec{x}(\varphi)) \cos\varphi d\varphi \quad \text{where} \quad \vec{x} = \vec{x}_0 + \vec{n} \cdot A_{\text{osc}} \cos\varphi \tag{4.8}$$

where A_{osc} is the oscillation amplitude of the cantilever, k_B is Boltzmann's constant, T is the temperature, b is the measurement bandwidth, f_0 is the resonance frequency of the unperturbed cantilever, Q is its quality factor and c_L is its longitudinal spring constant. Note, however, that the integral over the force also depends on the oscillation amplitude. From these two equations, the amplitude dependence of the signal to noise ratio is not obvious. Van Schendel calculated the equations necessary to describe the variation of the signal to noise ratio for any amplitude for magnetic forces and showed that large amplitudes enhance the signal to noise ratio (section 2.7.4 and appendix A). These results will be tested qualitatively in this section.

[12] In paragraph 4.3.3, for the Ni coated tips, large amplitudes have been used and the large amplitude theory has been applied in the tip calibration procedure.

4.5.1 MFM images acquired at different oscillation amplitudes

Using the ultrasharp tip, the frequency shift and the noise were studied as a function of the amplitude in order to test the calculated amplitude dependence of the frequency shift and noise. For this purpose, a series of five images were acquired using different oscillation amplitudes at the same lateral position on the Cu/Ni/Cu sample. These images are shown in figure 4.20. The tip-sample distance was adjusted so that the minimum tip-sample distance during an oscillation was approximately the same for all measurements. However, the determination of the tip-sample distance is only accurate to about 35% (paragraph 4.3.3) and the determination of the tip-sample distance cannot be done simultaneously to the measurement with the method used here. Due to these experimental difficulties, the minimum tip-sample distance varied between 60 nm (image 4.20 e)) and 34 nm (image 4.20 a)).

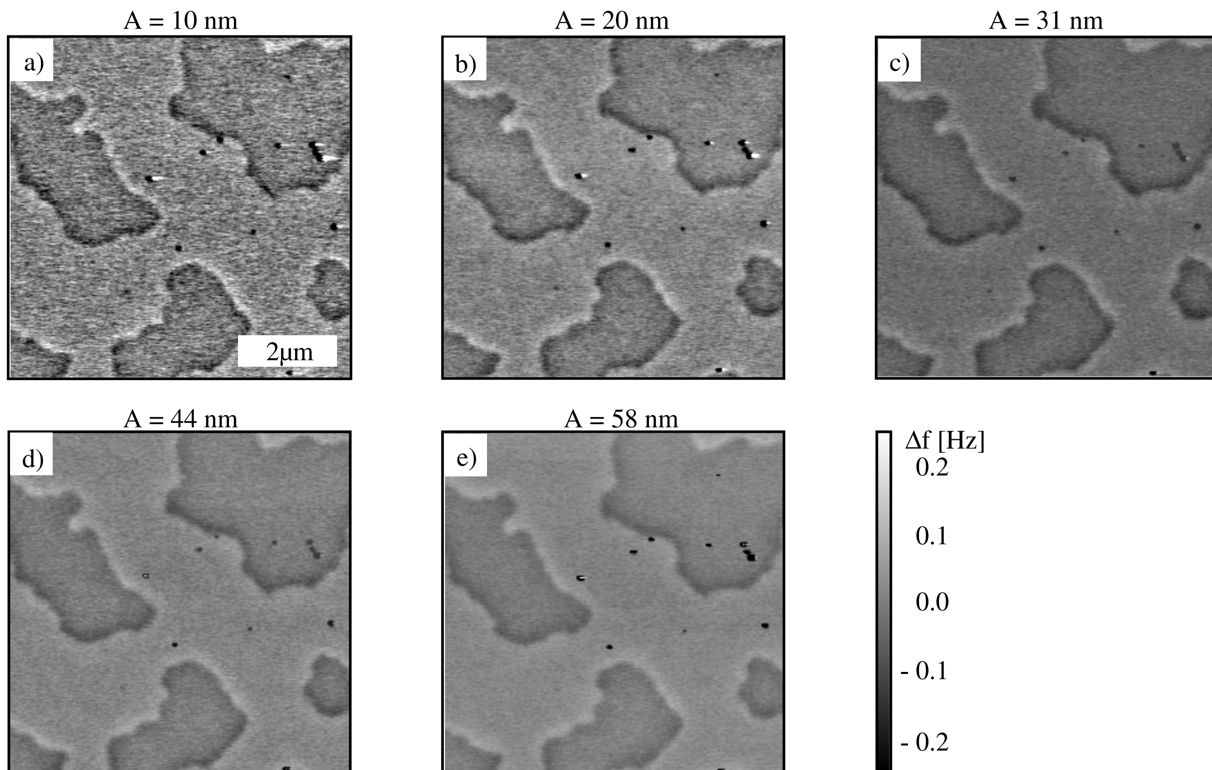

Figure 4.20: A series of images measured with different oscillation amplitudes. a) 10.1 nm b) 20.5 nm c) 31.5 nm d) 43.7 nm e) 58.5 nm. The frequency shift scale is the same for all images. The contrast changes strongly with increasing oscillation amplitude. Some black points in the images are topographical artefacts.

The frequency shift scale of the images has been set to the same values for the five images shown here. Qualitatively, the contrast decreases with increasing amplitude, however, as expected, the noise also decreases with increasing amplitude. The change in signal to noise ratio can be analysed quantitatively using the spectra of the images.

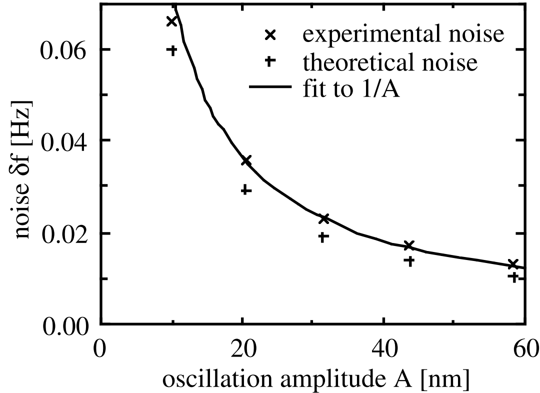

Figure 4.21: Root mean square noise calculated from the noise measurements and theoretical thermal noise limit as a function of the amplitude.

4.5.2 Evaluation of the noise

In order to evaluate the noise, for each amplitude, images have been acquired at a large distance to the sample with the image size set to zero. These images contain only noise and the root mean square value of the noise can be calculated from these measurements. The noise obtained experimentally by this calculation is compared to the thermal noise limit for each amplitude in figure 4.21. The thermal noise limit has been calculated using equation 4.7 with the parameters: T = 300 K, measurement bandwidth b = 100 Hz, resonance frequency f_0 = 81 745.39 Hz, quality factor Q = 15 000 and force constant c_L = 2 N/m. These parameters were determined experimentally, the force constant was specified by the manufacturer.

The experimentally determined noise is in good agreement to the thermal noise limit. Systematic deviations are possible if the parameters listed above contain errors. The oscillation amplitude may be slightly too small, as it was measured not at the position of the tip, but about 50 μm away from the tip on the cantilever beam. A fit to the experimentally determined noise using an inverse proportional law ($\sim 1/A$) is also plotted in figure 4.21. Comparison of the fit and the data indicates that the noise is proportional to $1/A$. No indication of amplitude independent noise is found from this analysis.

4.5.3 Evaluation of the signal to noise ratio

The spectra of the images were calculated by averaging over constant $k_{||}$. The spectra were normalized by the spectra of the noise measurements for each amplitude to obtain the signal to noise ratio as a function of the wave vector (figure 4.22). The result is shown in figure 4.22.

The analysis of the spectra confirms the interpretation obtained qualitatively from the images. The signal to noise ratio increases with increasing amplitude from 10.1 nm to 31.5 nm for all wavevectors at which a frequency shift is detected. At an even larger oscillation amplitude, the signal to noise ratio decreases again for large k vectors. The ratio is largest for the image taken with an amplitude of 31.5 nm. Increasing the oscillation amplitude further does not increase the signal to noise ratio. We conclude that in agreement with the equations presented in chapter 2.7.4, the signal to noise ratio increases if the amplitude is increased. For a sample of this domain size, the oscillation amplitude should be set to about 30 nm in order to achieve the best signal to noise ratio.

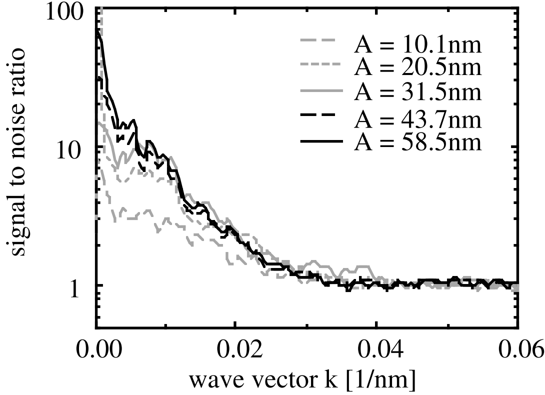

Figure 4.22: Signal to noise ratio for different oscillation amplitudes as a function of k-vector.

lever name	layer thickness [nm]	$f_0/(2c_L)$ [kHz/(N/m)]	calibration sample	B_{max} [mT]	critical wavelength [nm]
Fe-2.2	2.2	52.0	Cu/Ni/Cu	2.4	160
Fe-2.1	2.1	51.0	Cu/Ni/Cu	1.2	160
Fe-1.7	1.7	47.3	Cu/Ni/Cu	0.8	210
Ni-9.6	9.6	36.3	Cu/Ni/Cu	1.6	270
us-2.9	2.9	20.4	Cu/Ni/Cu	1.75	100
us-2.9	2.9	20.4	CAMST	3.6	86

Table 4.5: Comparison of the imaging properties of all calibrated tips.

4.6 Conclusions

In order to illustrate the main conclusions drawn from the MFM tip calibration, a summary of the parameters obtained is given in table 4.5. The magnetic field generated by ultrathin Fe tips scales roughly in proportion to the film thickness. The tips show good imaging properties down to a film thickness of about 1.7 nm. With a film thickness of about 1.7 nm the generated magnetic field is about 0.8 mT. Ni tips are not suitable for magnetic imaging, as the images show distortions that reflect either a canting of the magnetization vector relative to the tip axis or modification of the tip magnetization by the sample stray field. Other materials that have a significantly lower saturation magnetization than Fe, for example Cobalt ($M_S = 1420$ kA/m [86]) and magnetic alloys such as FePd ($M_S = 1100$ kA/m [90]) could be used as tip coating materials. Although the ultrasharp tip tested was damaged either due to the heat deposited at the tip apex during evaporation of the magnetic coating or by touching the sample during imaging, it still has a smaller critical wavelength and therefore a higher resolution than Nanosensor tips. The imaging properties of ultrasharp tips can be described by a monopole model in a better way than conventional Nanosensors proving that ultrasharp tips are sharper than Nanosensor tips.
Although the resolution of MFM can be improved by using sharper tips, in order to achieve atomic scale resolution, the regime of short-range forces must be considered. These short-range forces are studied in the next chapter.

Chapter 5

Atomic resolution imaging and frequency versus distance measurements on KBr at low temperatures

5.1 Introduction

To achieve atomic magnetic resolution with scanning force microscopy, short-range chemical bonding forces have to be probed. This chapter is about short-range chemical forces of non-magnetic origin on the ionic crystal KBr. Alkali halides are widely studied because of their known defect structure. Bulk defects lead to colour changes in these crystals and defects at surfaces play an important role in catalysis. Desorption and creation of defects is an important issue mostly studied by spectroscopic techniques. However, many surface sensitive techniques, for example LEED, photoemission spectroscopy, etc. can only be used on conductive samples. In particular, alkali halides cannot be imaged by STM unless they are grown as thin films on metals [91].

Alkali halide surfaces were the first insulating materials to be imaged by scanning force microscopy (SFM) with true atomic resolution [13]. The surfaces of these materials can be prepared and imaged easily with SFM. Although atomic resolution images on alkali halides have been obtained by several groups [92, 93, 94], the interaction force of a tip over a specific site has so far only been studied theoretically [95]. However, knowing this interaction force gives insight into atomic resolution image mechanisms and allows one to study bonding interactions on a surface on the atomic scale. In SFM operated at room temperature it is difficult to measure the site-specific force as a function of distance due to piezoelectric creep and thermal drift. Recently, site-specific force versus distance experiments have been performed for the first time at low temperatures on the Si(111) 7x7 surface [35]. Here we report similar measurements on the KBr surface in which we study the interaction forces and the imaging mechanism on KBr both experimentally and theoretically.

5.2 Tip and sample preparation

KBr single crystals were purchased from Korth, Altenholz, Germany. Clean, flat alkali halides (001) surfaces can easily be obtained by cleaving a single crystal. Previously it has been shown by SFM [92] that KBr crystals cleaved in air and subsequently heated in ultra-high vacuum show atomically clean surfaces similar to crystals cleaved in ultra high vacuum (UHV). The surface charge accumulated during the cleaving process [96] can be relieved by heating the crystals in vacuum. The results described here were obtained on crystals cleaved in air and subsequently heated in UHV to 100° C for 1 h.
All SFM measurements were carried out in our home-built UHV low temperature SFM at about 7 K. We used silicon cantilevers provided by Nanosensors, Wetzlar, Germany with a force constant of about 40 N/m and a resonance frequency of about 170 kHz. After introducing a tip into ultrahigh vacuum it was heated to 150° C for 1 h, without additional cleaning, for example, by sputtering. We therefore assume that our tips were originally covered with SiO_2. The SFM measurements were carried out in dynamic SFM mode with a constant cantilever oscillation amplitude of 5 nm, using a home-built phase locked loop FM-detection system as described in reference [33].

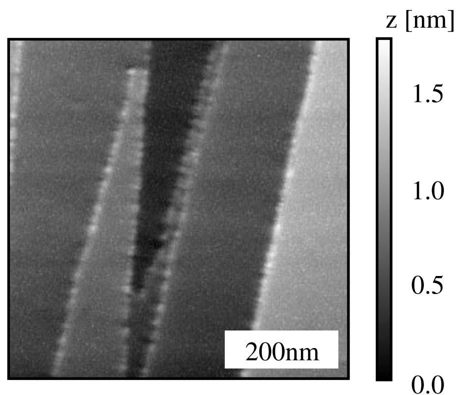

Figure 5.1: Large scale image of a freshly cleaved KBr surface. The frequency shift was −2 Hz. The cleavage steps run in high indexed directions and seem to be decorated with bright, i.e. topographically high or reactive, objects.

5.3 Large scale images

After the preparation procedure described above, large scale SFM images of the surface showed straight cleavage steps. A typical image is shown in figure 5.1. The (100) direction in this image is parallel to the y axis (see also figure 5.2). The mono- and biatomic cleavage steps run in high indexed directions. They therefore contain many kink sites. Bennewitz et al. reported that ions on kink sites are imaged as bright [93]. The bright protruding objects visible at the step edges in figure 5.1 are therefore likely to be kink sites. Almost no defects on the terraces are visible.

5.4 Atomic resolution images

5.4.1 Constant frequency shift contours

After obtaining a large scale image we made higher resolution images on a terrace. While imaging above this terrace we tried to avoid defects and gradually reduced the tip-sample spacing by

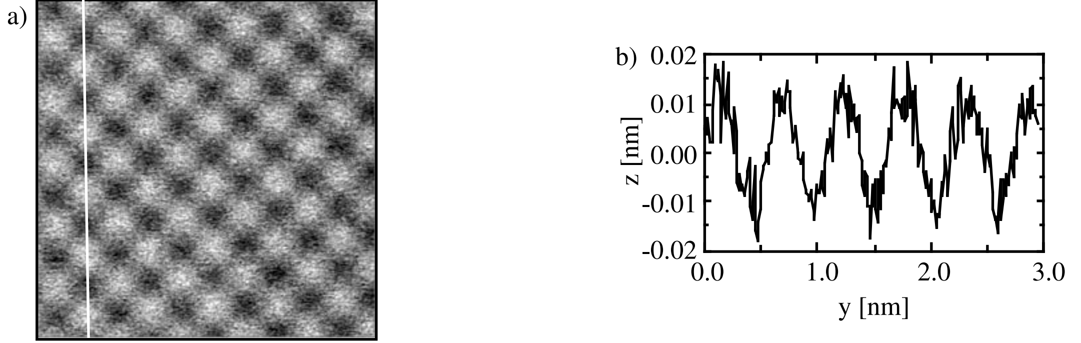

Figure 5.2: a) Atomic resolution image of a KBr (001) surface (Frequency shift -10.4 Hz, $\Gamma = 9.0 \cdot 10^{-16}$ $\mathrm{Nm}^{0.5}$). b) Line section taken along the solid line in a). For this measurement: $c_L = 43$ N/m, $f_0 = 174\ 719.67$ Hz and $A = 5$ nm.

increasing the magnitude of the constant frequency shift set point until atomic resolution images were obtained, showing a series of protrusions on a square lattice (see figure 5.2). The lattice constant of this primitive square lattice corresponds to the interatomic distance of two ions of the same species $a/\sqrt{2}$ (where $a = 0.3264$ nm is the bulk lattice constant [97]). Its orientation is rotated by 45° relative to the bulk (100) direction. This type of contrast is similar to the contrast obtained in previous room temperature studies of KBr and other alkali halides [13, 93]. The corrugation observed in figure 5.2 is about 0.025 nm in agreement with previous results ($\Gamma = (\Delta f/f)c_L A^{3/2} = 9.0 \cdot 10^{-16}$ $\mathrm{Nm}^{0.5}$): Bennewitz et al. obtained a corrugation between 0.03 nm for a total frequency shift of -10 Hz ($\Gamma = 1.9 \cdot 10^{-15}$ $\mathrm{Nm}^{0.5}$) and 0.1 nm for a frequency shift of -50 Hz ($\Gamma = 9.6 \cdot 10^{-15}$ $\mathrm{Nm}^{0.5}$) on KBr [92]. Bammerlin et al. obtained on NaCl a corrugation between 0.05 nm for a sharp tip with a frequency shift of -50 Hz ($\Gamma \approx 1.4 \cdot 10^{-14}$ $\mathrm{Nm}^{0.5}$) and 0.35 nm for a blunt tip with a total frequency shift of -180 Hz ($\Gamma \approx 4.9 \cdot 10^{-14}$ $\mathrm{Nm}^{0.5}$) [98]. According to these measurements, the corrugation is larger the blunter the tip: the stronger background van-der-Waals forces allow stable operation close to the surface. On the other hand, Bammerlin et al. obtained a corrugation between 0.05 nm and 0.175 nm for the same total frequency shift. This underlines the importance of the atomic details of the tip i.e. the chemical nature of the tip and the height of the frontmost protrusion as discussed further below.

5.4.2 Tip instabilities

Following the acquisition of the image shown in figure 5.2, the tip was altered by an uncontrolled tip change after which image 5.3a) was obtained. The image remained stable for about 4/5 of the image with one minor tip change (labelled 1 in figure 5.3a)), where the corrugation stayed almost constant. The corrugation observed in the lower part of the image, about 0.07 nm, can be read from the line section presented (figure 5.3c)). This increase in corrugation relative to figure 5.2 implies that the tip has become sharper and / or that the interaction force has become stronger. After 4/5 of the image was acquired, a tip change occurred (tip change labelled 2 in figure 5.3a)). Then the tip-sample distance was decreased by the feedback loop by about 0.07 nm in order to keep the frequency shift setpoint value constant. This implies that something was removed from the tip and / or that the interaction force decreased. After this tip change, the corrugation was reduced to only 0.025 nm, similar to the corrugation observed previously (line section B in figure 5.3). The magnitude of the distance change (0.07 nm) is comparable to the

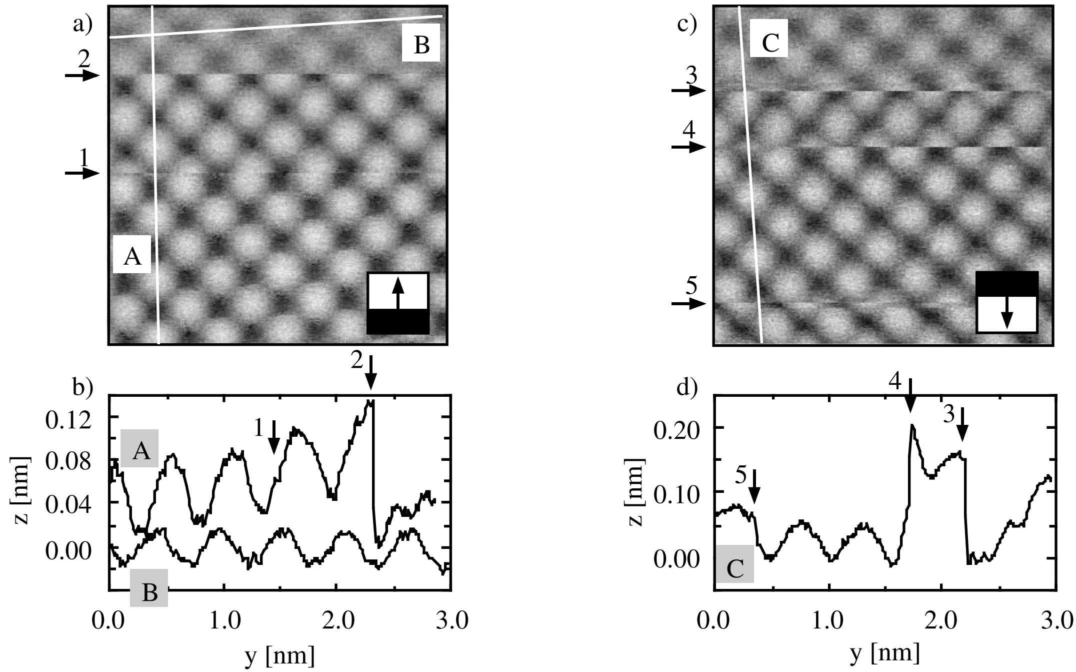

Figure 5.3: a), c) Atomic resolution image of a KBr (001) surface with a tip change. The solid lines labelled A, B, C indicate the positions of the line sections through the original data shown in (b) and (d) respectively. Image (a) was acquired by scanning from the bottom to the top of the image using a frequency shift set point of −14.8 Hz. Two tip changes labelled 1 and 2 occurred during scanning. Image c) was acquired directly after image a) by scanning from the top to the bottom. The frequency shift setpoint was changed between −14.8 Hz and −15.5 Hz in the upper quarter of the image. The numbers indicate the positions where tip changes occurred. Note that a significant decrease in corrugation is observed after the tip change near the top of image (a) while in image (c) a compensating tip change occurs at approximately the same scanline and results in a significant increase in the image corrugation.

corrugation observed in the lower part of the image. It is probable that the tip change labelled 2 in figure 5.3 is the reverse of the very first tip change. Possibly an atom jumped from the tip to the sample or to another place on the tip or the electrical charge of the tip changed.
In order to check this hypothesis, we tried to reverse the tip change intentionally. To do this, we scanned the same area, in this case starting the scan from the positive y side of the image and moving towards the negative y direction (as indicated in figure 5.3c)) and chose a more negative frequency shift setpoint in order to move closer to the sample. During a scanline close to the region where the previous tip change occurred, the tip changed again (tip change number 3), and the strong corrugation of 0.07 nm was again established. We conclude that the tip change was reversed. After several minor tip rearrangements (labelled 4 and 5) and after finishing image 5.3c) this strong corrugation suddenly disappeared.
This measurement provides a clear example where at the same total frequency shift the atomistic tip structure strongly affects the measured corrugation.

5.4.3 Energy dissipation

Several mechanisms are currently discussed as possible origins of atomic scale variations in the excitation amplitude necessary to maintain the cantilever oscillation at a constant amplitude

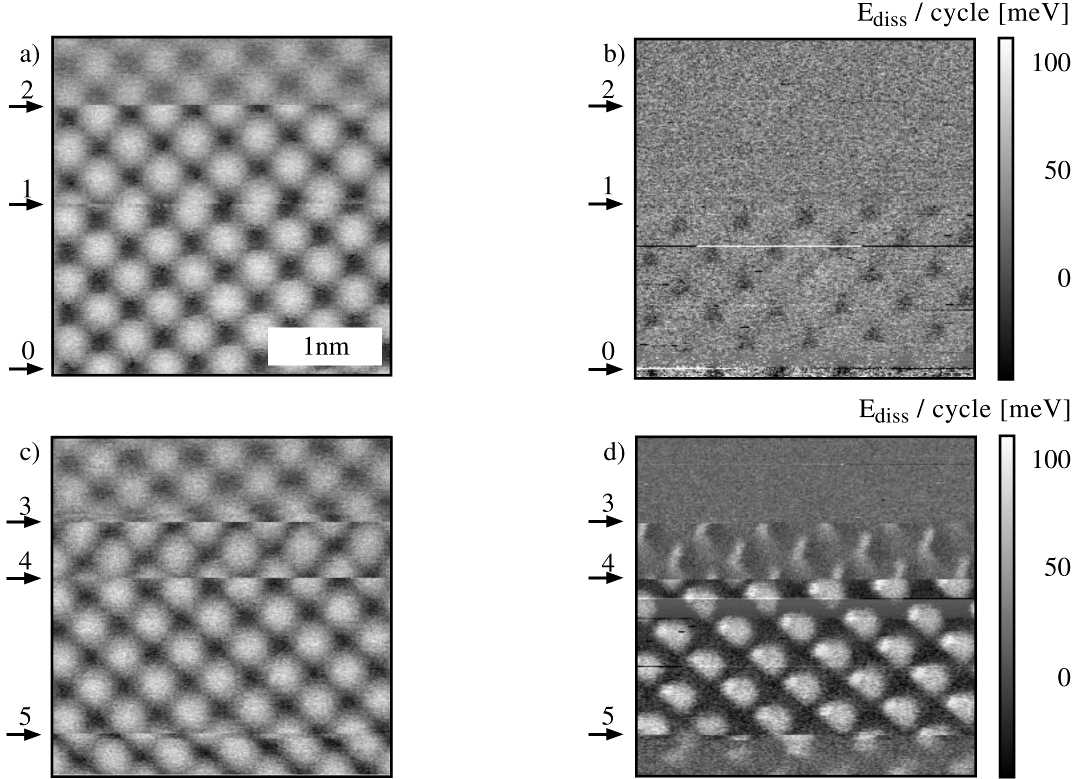

Figure 5.4: Dissipated energy shown together with the corresponding topographic atomic resolution images. For this measurement: $c_L = 43$ N/m, $f_0 = 174\ 719.67$ Hz, $A = 5$ nm and $Q = 58\ 000$.

(chapter 2.6.2). One of the mechanisms that could lead to energy dissipation is hysteretic movement of atoms. Therefore, if a movement of atoms is detected, like the tip instabilities discussed in the last paragraph, the question arises whether this movement is related to dissipation. As mentioned, the excitation amplitude necessary to maintain a constant oscillation amplitude of the cantilever is recorded in parallel to all SFM images. Changes in the measured excitation amplitude when the tip changes can give an insight into the dissipation mechanism. The excitation amplitude recorded parallel to images 5.3 a) and c) has been converted to units of dissipated energy per oscillation cycle using equation 2.11, and is shown in figure 5.4. During most of the two images, atomic resolution contrast is observed in the dissipation. Tip changes in the topographic images are related to contrast changes in the dissipation image. In the two regions of the images 5.4 a) and c), where only weak topographic corrugation is observed (between tip changes 2) and 3)), no atomic resolution in the dissipation occurs. The tip change labelled 0 in image 5.4 a) and some altered scanlines are only visible in the dissipation. In the region between tip changes 3) and 4) in image 5.4c), the tip has to be retracted by about 0.13 nm to remain at the frequency shift setpoint (see scanline C in figure 5.3d)), and the tip therefore is extremely sharp[1] compared to the other parts of the image. One could suspect that in this region, the frontmost (imaging) ion is in an unstable position. However, the region between tip changes 3 and 4 is not the region with the largest corrugation of the dissipation. Regions of comparable

[1]Sharp means here showing a longer nanotip.

frequency shift corrugation show a completely different magnitude of the dissipation. Although regions with no small dissipation but large topographic corrugation occur in image 5.4a) (between tip changes labelled 1 and 2), the imaging tip does not remain in this configuration for a significantly longer time period than in the other configurations, and another tip change occurs (tip change labelled 2). In conclusion, there is no indication that unstable configurations of the tip apex ions correspond to regions with large energy dissipation.

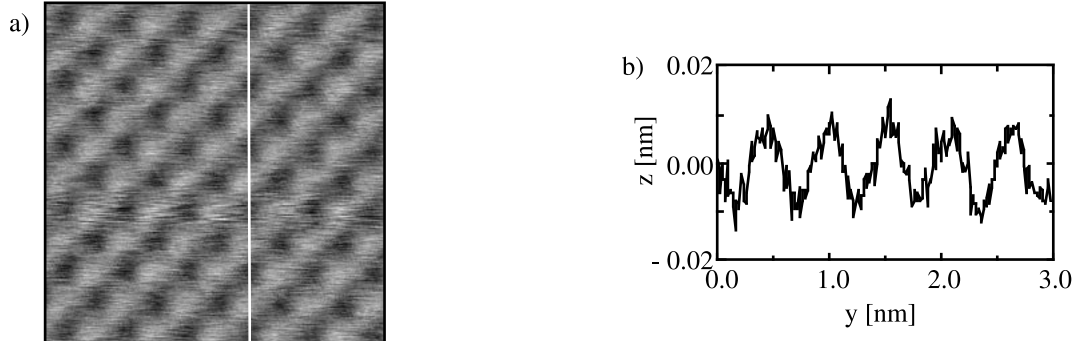

Figure 5.5: 3×3 nm^2 image before the frequency versus distance measurements (Frequency shift -26.4 Hz, $\Gamma = 2.3 \cdot 10^{-15}$ Nm$^{0.5}$).

5.5 Frequency versus distance measurements

In order to study the interaction forces and to characterize the tip in more detail, we performed measurements of the resonance frequency of our cantilever as a function of the distance to the sample above specific atomic sites using a procedure similar to that described in reference [35]. First an image was acquired; second, the feedback was switched off, the tip was retracted and moved laterally to acquire two frequency versus distance curves, one above the maximum of the observed corrugation and one above the minimum. There is very little thermal drift or creep in our instrument at 7 K, and this procedure should minimize any residual thermal drift between the members of each pair of frequency versus distance curves. Finally, the feedback was switched on again, and another image was acquired to confirm that no tip changes or thermal drift had occurred, i.e. the maxima of the atomic scale corrugation were observed in the same position as in the image acquired before the frequency versus distance experiments. Frequency versus distance data over a z-range of 15 nm were first acquired to make an accurate determination of the long-range forces. For a higher precision in the short-range regime, measurements over a z-range of only 0.5 nm were acquired. The acquisition time for each approach and retraction was $2 \cdot 120$ s. The parameters of the cantilever used were: resonance frequency $f_0 = 175$ 123.4 Hz, longitudinal spring constant $c_L = 43$ N/m and oscillation amplitude $A = 5$ nm.
The image obtained immediately before starting the frequency versus distance measurements is shown in figure 5.5. The corrugation obtained is similar to that obtained in figure 5.2.
The long-range frequency shift as a function of the tip-sample distance obtained is shown in figure 5.6. All long range - data obtained with the same tip were identical even for measurements performed two days later on a different part of the KBr crystal. For both the short-range and long-range experiments the approach data were identical within the experimental noise limit to the retraction data. The long-range data is shifted relative to the short-range data because of

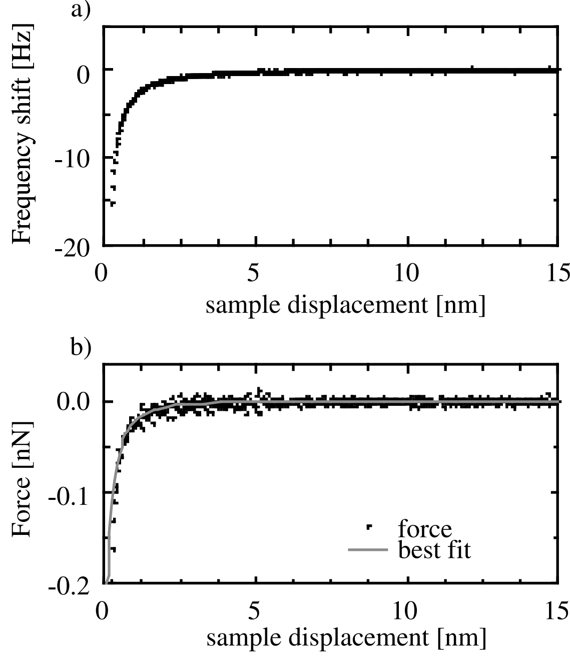

Figure 5.6: Long-range frequency shift on a KBr surface and force obtained after conversion using the method developed by Dürig [28]. The solid grey line in the force plot is a fit obtained assuming only a van-der-Waals force acting between a conical tip with a spherical cap and a flat surface.

the piezo-electric creep effect. This effect can be compensated by shifting the z-axis offset of the long - range data with respect to the short-range data by 84 pm (figure 5.6 shows the shifted data). This value was determined experimentally. To show the resulting match of the two sets of data, the long-range data is shown together with the short range data in figure 5.7.

5.5.1 Analysis of the frequency versus distance data

The oscillation amplitude used here (5 nm) is large compared to the decay length of the frequency shift (figure 5.6). In the large amplitude mode, a simple linear relationship exists between the force and the measured frequency shift [28]. The frequency shift can be transformed into a force using the iterative method developed by Dürig [28]. One iteration was enough to obtain convergence. In order to check the adequacy of the inversion procedure, the frequency shift was calculated from the force obtained by the Dürig method; no significant difference compared to the original data was found. The results are shown in figure 5.6.

The long-range force data can be compared to a model of the long - range van der Waals force. We used a function that describes the van der Waals force acting between a cone with a spherical cap and a flat surface [36, 37].

$$F_{\mathrm{vdW}}(z) = -\frac{C_H}{6}\left[\frac{R}{z^2} + \frac{\tan^2\alpha}{z+R_\alpha} - \frac{R_\alpha}{z(z+R_\alpha)}\right] \tag{5.1}$$

where C_H is the Hamaker constant, R is the tip radius, $R_\alpha = R(1-\sin(\alpha))$ and z is the distance of the surface to the tip. A fixed total cone angle of $2\alpha = 20°$ was used. This cone angle is closer to the value given by the manufacturer ($2\alpha = 20°$) than the angle of $2 \cdot 50°$ used by Guggisberg et al. [36]. Also the Hamaker constant $C_H = 2 \cdot 10^{-20}$ J was fixed because C_H and R cannot be determined simultaneously with a good precision. C_H is $4 \cdot 10^{-20}$ J for CaF_2 interacting with CaF_2 [99], but a lower value is realistic considering that the tip is probably covered with SiO_2.

The best fit was obtained using $R = 14$ nm which is in agreement with the nominal value given by the manufacturer ($R < 10$ nm).
The KBr crystal was mounted directly on a conducting copper plate, to which a bias voltage could be applied. During our experiments the copper plate was grounded. However, small electrostatic forces can arise, if residual charge remains on the insulating surface even after heating. In this experiment, the electrostatic force model used in reference [36] does not describe the measured forces. In another experiment using a different tip and KBr crystal (data not shown), the long-range force data has been well fitted using a model which describes the electrostatic force acting between the tip and sample and a fitting parameter of 0.2 V. Residual surface charge created during the cleaving process could lead to electrostatic forces if the crystal has not been heated sufficiently long to remove all surface charge. We conclude that we can distinguish between a long-range force dominated by an electrostatic force and a long-range force dominated by a van-der-Waals force, and that for the data presented here, the electrostatic force was negligible compared to the van-der-Waals force.

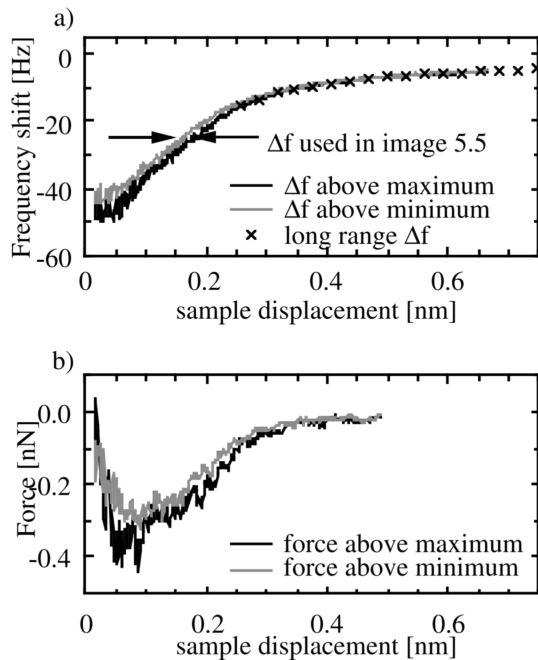

Figure 5.7: Short-range frequency shift and force obtained after conversion above the maximum (black line) and minimum (grey line).

5.5.2 Short-range forces

Around the distance to the sample where atomic resolution images were acquired, force versus distance data were acquired using a smaller z range of only 0.65 nm. In this regime, the force results from both long-range van-der-Waals forces and short-range chemical binding forces (figure 5.7). The short-range frequency distance measurements show that the short-range forces, like the long range forces, are very small compared to the chemical binding forces on the Si(111) 7×7 surface [35]. Comparing the data measured above the local topographic maximum and minimum, we see that the corrugation, i.e. the difference in sample displacement at constant frequency shift, is in agreement with the corrugation observed in figure 5.5. Unfortunately, with such small frequency shifts, the influence of the noise on the data is significant and the corrugation is very hard to quantify. There also seems to be some variability in the corrugation inferred

from different measurements done one after another with the same tip on the same part of the KBr crystal: it varies between zero and about 0.03 nm. Apart from the noise another reason for this variability could be that the area of the minima in the image is quite small, and there might be some uncertainty when the position of the frequency versus distance measurement is chosen by the experimentalist. However the total frequency shift varies only by about 15 % from measurement to measurement.
The short-range frequency distance data have been converted to force using the same procedure as for the long-range force (described in the previous paragraph and also in paragraph 2.4.2). Assuming that the long-range forces are site independent, we can separate the force components by subtracting the long-range force fit to the data shown in figure 5.6. The results are presented in figure 5.7. The maximum attractive short-range force is about 0.3 nN and the interaction range is about 0.2 nm. The position of zero force, determined from the intersection of the force data with the line of zero force, is shifted with respect to the van-der-Waals zero point by about 0.36 nm. We interpret this as resulting from an extremely sharp nanoscopic tip on the apex of the mesoscopic tip described earlier. The order of magnitude of the short range forces is in agreement with simulations of forces of an SFM tip on a NaCl surface, however the force contrast observed here is smaller [95]. The error introduced by the uncertainty of the amplitude and force constant of the cantilever is estimated to about 30 %.
The z scale was adjusted in all frequency and force versus distance data such that the short-range force measured above the maximum becomes zero at $z = 0$. The distance where the force is zero corresponds to the binding length of KBr, 0.330 nm. From this we conclude that the imaging distance in image5.5 was about 0.175 nm+0.330 nm=505 nm. This can be compared to values obtained from calculations shown in the next section (section 5.6). However, this value depends on the fit of the long-range forces in the experiment especially in the region below 1 nm distance to the surface, where the fit is an interpolation of the data obtained at larger distances. Although it was possible to measure the frequency versus distance above the maximum and minimum of the observed corrugation up to a frequency shift of about −45 Hz, it was not possible to acquire an atomic resolution image at a frequency shift smaller than −26.4 Hz. A similar observation has been discussed in reference [35]. This is an indication that tip changes do not mainly take place at positions above the maximum or above the minimum and merits further studies.

5.5.3 Conclusions

The first site-specific force versus distance measurements of the weak interaction force between a sharp tip and an insulator were presented. It was possible to describe the very weak long-range force using a model of the van-der-Waals interaction with the surface. The atomic details of the tip were found to play a strong role in the corrugation obtained in atomic resolution images. Switches in contrast are related to changes of the atomic structure of the tip apex. This could be studied further by preparing atomically controlled tips for example by depositing metal on the tips or by simulating the interaction forces for different tip structures.

5.6 Calculation of the tip-sample interaction using atomistic simulations of the KBr (001) surface

In order to study the interaction from a theoretical point of view, the force between a conducting tip terminated by a KBr cluster and a KBr (001) surface has been calculated using atomistic simulations. L. Kantorovich and A. Foster developed a program which computes the electrostatic and chemical binding forces acting between a system of conducting objects and ions in order to conveniently model SFM on ionic crystals [100]. Such atomistic simulations were previously applied to NaCl (001) [95] and to CaF_2 (111). In the latter system, it was possible to distinguish between positively and negatively terminated tips and to identify sites of Ca^{2+}- and F^--ions on a CaF_2 (111) surface [101]. The method used for distinguishing between positively and negatively terminated tips relies on the comparison of measured and calculated images. Our direct measurements of the site-specific short-range forces offers a unique possibility to compare calculated forces with experiments in unprecedented detail.
So far, such calculations have been carried out assuming a MgO tip. MgO has a similar optical refractive index as SiO_2, therefore it shows a similar Hamaker constant and is assumed to adequately represent a SiO_2-covered tip. However, in the experiment, material transfer from the surface to the tip is frequently observed even when hard contact of tip and sample are avoided. Therefore, we have performed calculations for a tip made of the same material as the sample.

5.6.1 Simulation program, tip and sample models

In the simulation program the van-der-Waals and electrostatic long-range forces with the mesoscopic part of the tip are added after calculation of the short-range forces. The latter are computed from a pairwise sum of Buckingham potentials acting between ions treated atomistically (see figure 5.8)

$$U_B(r) = C_1 e^{-r/r_0} - \frac{C_2}{r^6} - \frac{C_3}{r^8} \tag{5.2}$$

where C_1, C_2, C_3, r_0 are parameters defined for each type of ion pair obtained by fitting experimental phonon dispersion relations of bulk ionic crystals.
The ions are described by a shell model with coupled charged cores and shells in order to take the polarizability of the ions into account. The microscopic dipole moment of one ion is given by $\vec{p} = \alpha_{\text{pol}}\vec{E}$ where $\vec{E}$ is the local electric field generated by the other ions. The polarizability α_{pol} is modelled by a linear force acting between ion cores and shells with a spring constant

$$c_{\text{pol}} = \frac{Q_{\text{shell}}^2}{4\pi\varepsilon_0\alpha_{\text{pol}}} \tag{5.3}$$

where Q_{shell} is the shell charge. The parameters used here were taken from [97] and are summarized in table 5.1. For comparison ionic radii are included although this is not a parameter used by the simulation program.
The sample was represented by a slab of 6 layers of 10×10 atoms. The positions of the atoms situated in the bottom layer of the slab or at the sides of the cluster were kept fixed during the calculations. All other atoms of the sample were allowed to relax. In a first calculation in the absence of the tip, the position of the Br^--ion cores situated at the surface of the sample moved in the positive z direction by about 7 pm while the Br^--ion shells and the K^- cores and shells

interaction parameters	C_1 [eV]	r_0 [pm]	C_2 10^{-6}[eV nm^6]	C_3 10^{-8} [eV nm^8]
$K^+ - K^+$	6172×10^6	10.85	-36.22	-28.74
$Br^- - K^+$	4398	32.77	-126.07	-123.22
$Br^- - Br^-$	2745	39.86	-454.9	-528.4
ion	ionic radius [pm]	core charge [e]	shell charge [e]	spring constant c_{pol} [eV/nm^2]
K^+	152	6.93590	-5.96590	4.8482
Br^-	182	1.76700	-2.73700	0.2380

Table 5.1: The parameters used for calculating the Buckingham potentials, the shell and core charges and the polarizability. For the Buckingham potential a cutoff was used at r = 500 pm. Note that the constant C_1 responsible for the repulsive short-range interaction at close interatomic distances is 10^6 times stronger for the cation-cation interaction than for the cation-anion interaction or for the anion-anion interaction. Also note the large polarizability of the Br^--ion as reflected in its small value of c_{pol}. The K^+- Br^- bulk separation is a_{KBr} = 326.4 pm [97].

remained almost at their truncated bulk positions. The result is a small dipole at the position of each Br^--ion. This is a result of the polarizability of the Br^--ions and of the broken cubic symmetry at the surface.

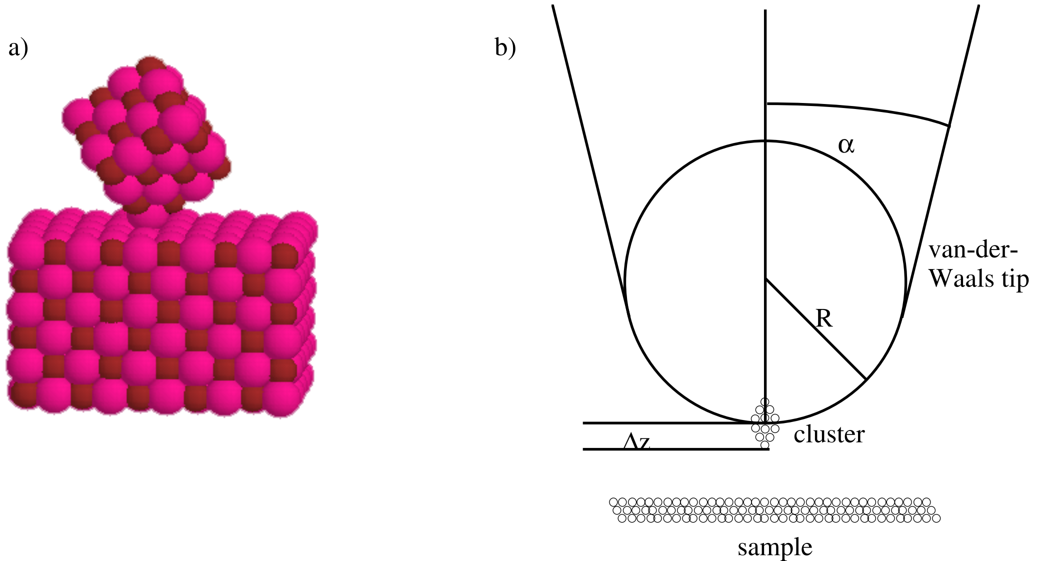

Figure 5.8: a) Tip and sample model used for the atomistic simulations. b) The van-der-Waals force on the mesoscopic tip is added afterwards.

The atomistic part of the tip was represented by a cubic cluster of 64 KBr ions (32 K^+-ions and 32 Br^--ions) oriented such that the (111) direction was perpendicular to the sample (figure 5.8). In this orientation, the cluster contains 10 layers of equally charged ions. Two tips were considered: one with a K^+-ion, and one with a Br^--ion at the tip apex closest to the sample. First, the relaxed positions of the ions contained in the tip cluster were computed. The topmost 5 layers were then fixed for all further calculations; z was defined using the position of the tip apex ion obtained from this relaxed cluster. The interaction forces on these fixed tip ions were summed

to evaluate the short-range force on the tip for each position. A conducting sphere was added to represent the conducting silicon tip where image charges induced by the ions in principle occur. The bottom of the conducting sphere ($R = 10$ nm) was located about 1.1 nm higher than the frontmost (tip apex) ion.
The tip was placed above 15 positions on an orthogonal grid contained in a triangle within 1/8 of a primitive surface unit cell (see figure 5.9). The spacing was 1/8 of the distance between equal ions. Similar positions contained in any other portion of the surface can be obtained from these by applying symmetry operations.

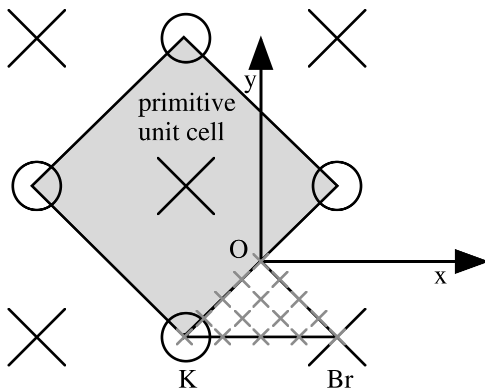

Figure 5.9: Positions where the force versus distance data were calculated.

For each of these 15 positions, the force on the tip was calculated at successive tip-sample distances moving closer to the sample. At each position, the shell and core positions were allowed to relax until equilibrium was reached. The energy tolerance was set to $1 \cdot 10^{-8}$ eV and the force tolerance was set to 0.016 nN. At each z, the ionic positions of the previous z were used as starting values for the new calculation. Thus, theoretical site-dependent force versus distance data were generated. The positions of the frontmost tip atom and the nearest sample atom were retained, giving relaxation versus distance data. The tip apex ion moved less than 40 pm in all calculations, whereas the surface Br^--ion moved less than 50 pm when the K^+-terminated tip was brought close to it. No tip atom jumped to a position on the surface during the calculations, even in the regime of repulsive forces. When calculating retraction data, the same force and relaxation versus distance values were obtained as for the approach to the surface. This confirms that our calculated data are in the true non-contact regime in the distance range studied.

5.6.2 Force versus distance and relaxation versus distance data

The typical characteristics of the calculated force versus distance data can be summarized by analysing the data obtained above the K^+-ion, the Br^--ion and the intermediate position O (see figure 5.9). They are shown in figure 5.10 for the K^+- and the Br^--terminated tip.
Unlike the Si (111) surface, where covalent attractive chemical bonding forces dominate in the non-contact regime [35], on the ionic crystal KBr, short-range repulsive forces arise when the ion at the tip apex faces an ion of the same type on the sample. In the case of the Br^--terminated tip, the strongest attractive force appears over the K^+-ion. A small repulsive force arises over the Br^--ion before the total short-range force becomes attractive at closer distances, then reaches a minimum and becomes repulsive. The force versus distance data calculated at the position O shows a minimum of intermediate depth at a distance located between the positions of the minima observed for the Br^--ion and for the K^+-ion. The maximum attractive force obtained

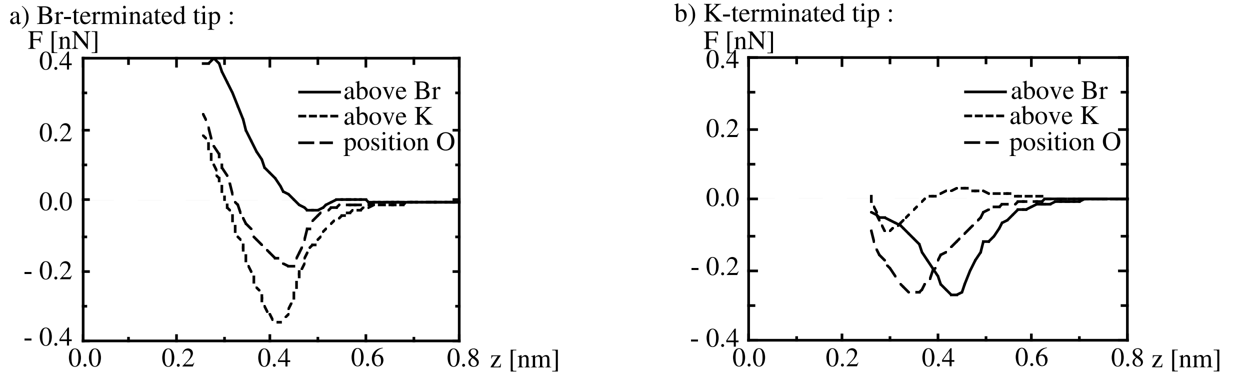

Figure 5.10: Force versus distance data calculated for the Br^-- and the K^+-terminated tip above three atomic sites.

above the K^+-ion is about 0.32 nN and the short-range attraction decays to 1/e of its maximal value within about 100 pm.

In the case of the K^+-terminated tip, a repulsive force first occurs upon approach above the K^+-ion, while the force above the Br^--ion shows a pronounced minimum. The z-range where repulsive forces occur is larger in the case of the K^+-terminated tip above a K^+-ion compared to the case of a Br^--terminated tip above a Br^--ion. The maximum attractive force obtained above the Br^--ion is about 0.35 nN and the range of the short-range attractive forces is about 100 pm, similar to the Br^--terminated tip.

The value of the maximal force obtained and the range of the forces are of the same order as in calculations for a MgO tip against a NaCl (001) surface [93, 95] and a MgO (001) surface [102]. For the K^+-terminated tip, the minimum of the curve obtained at position O is not at the same z distance as the minimum in the curve obtained above the Br^--ion: it is shifted by about 100 pm closer to the sample. Furthermore, the data obtained above the Br^--ion, above the K^+-ion and above position O show qualitatively different repulsive forces. This is consistent with the force obtained at intermediate positions. Whereas the force obtained with the Br^--terminated tip shows a minimum of different magnitude at about the same z distance, the force data obtained with the K^+-terminated tip show a minimum either near the z distance where the minimum occurs above the Br^--ion or near the z distance where the minimum occurs above position O depending on the lateral position. Nevertheless the force curves change smoothly from position to position along lines on the surface in both cases.

On the basis of these results an experiment can be proposed to distinguish between a K^+-terminated tip and Br^--terminated tip: a measurement of the force versus distance data above the position O makes it possible to distinguish between a K^+-terminated tip and a Br^--terminated tip.

The change in position of the frontmost tip atom relative to its equilibrium position in the absence of the sample is shown in figure 5.11 for the three different sites and both tip terminations. The data follow qualitatively the force versus distance data although the force acting on the tip is highly nonlinear. No atomic jump instabilities occurred in the tip-sample distance regime covered even where the forces became repulsive. Such instabilities are however expected to occur at shorter distances.

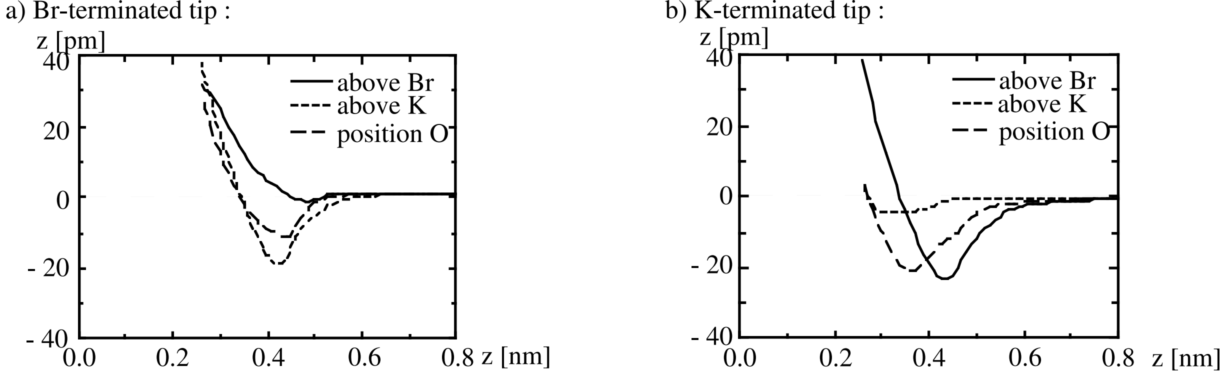

Figure 5.11: Relaxation of the frontmost tip atom calculated for the Br^-- and K^+-terminated tip above three different sites.

5.6.3 Frequency versus distance data

In order to compute the value of the total force a van-der-Waals force must be added to the computed short range forces. To match best the experimental conditions, the van-der-Waals force obtained from the experiment described in section 5.5 is added to the calculated force data to obtain the total force. An expression computed for a conical tip with spherical cap facing a flat half space given by [36, 37]

$$F_{\mathrm{vdW}}(z) = -\frac{C_H}{6}\left[\frac{R}{z^2} + \frac{\tan^2\alpha}{z+R_\alpha} - \frac{R_\alpha}{z(z+R_\alpha)}\right] \tag{5.4}$$

was used with a Hamaker constant $C_H = 2 \cdot 10^{-20}$ J, a tip radius $R = 14$ nm, a tip opening angle $2\alpha = 20°$. Also the values of the cantilever longitudinal spring constant $c_L = 43$ N/m, the unperturbed resonance frequency of the cantilever $f_0 = 175\ 123.4$ Hz and the oscillation amplitude $A = 5$ nm were chosen to match the experimental conditions of section 5.5.
From these total force data, realistic frequency shift versus distance data can be calculated. The only remaining free parameter is the relative offset Δz of the origin in equation 5.4 with respect to the origin of the short-range forces[2]. This corresponds to different heights of the nanotip (see figure 5.8). At small distances where the short-range forces become important, the van-der-Waals attraction still makes a significant contribution to the total frequency shift which is quite sensitive to the offset Δz.
Different values of Δz were therefore chosen to evaluate the effect of the van-der-Waals force on the frequency shift. The results are shown in figure 5.12. The calculated maximal corrugation at constant frequency shift is marked by arrows in the figures. The frequency shift obtained experimentally is superposed on the calculated frequency shift in the figures. First, the results of the calculations will be discussed independently of the experiment, then the calculated frequency shifts will be compared to the experiment.

Calculated frequency versus distance data
For a short nanotip with $\Delta z = 80$ pm (figure 5.12a) and b)), the calculated maximal corrugation at constant frequency shift is small (about 30 pm) and no qualitative difference is found between

[2] It is also possible to compare the calculated short-range force versus distance data to to the experimentally obtained short-range force obtained after subtracting the long-range force. Here, we compare the frequency shifts.

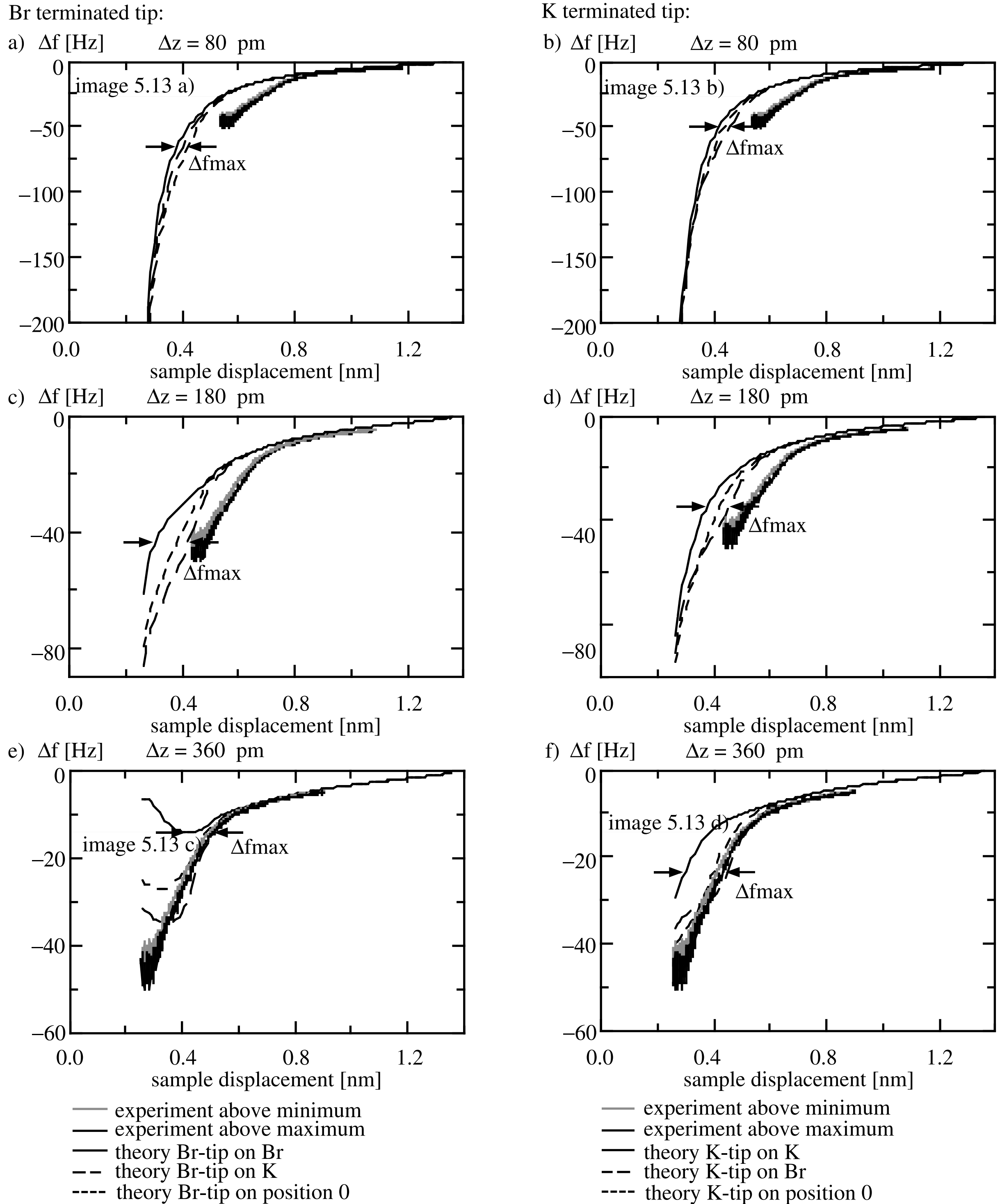

Figure 5.12: Comparison of measured frequency shifts with calculated ones from force versus distance data computed from a model that includes the experimental long-range force for three values of the offset Δz, and for the K^+ and the Br^--terminated tip. The calculated maximal corrugation at constant frequency shift is marked by arrows. The experimentally obtained data superimposed to the calculated data exhibit a much smaller corrugation.

a K^+-terminated and a Br^--terminated tip (the interaction between equally charged ions are similar for both tip terminations and the interaction between oppositely charged ions are similar for both tip terminations). When the tip protrudes more (Δz = 180 pm), the corrugation increases (figure 5.12c) and d)). The maximal corrugation at constant frequency shift is about 200 pm for the Br^--terminated tip and 150 pm for the K^+-terminated tip with a nanotip of Δz = 180 pm. If the tip protrudes even further (Δz = 360 pm, figure 5.12e) and f)), in the case of a Br^--terminated tip, imaging is no longer possible at large negative frequency shifts, because the repulsive short-range interaction produces a smaller minimum above Br^--sites. Therefore only a small corrugation can be obtained for the Br^--terminated tip with a nanotip height of $\Delta z = 360$ pm. In the case of the K^+-terminated tip, the corrugation increases further, however. This means that the Br^--terminated tip produces a larger corrugation for a medium-sized nanotip, while the K^+-terminated tip gives a stronger corrugation for a more protruding nanotip. Note also that the mean imaging distance at the optimal frequency shift strongly depends on the height Δz of the nanotip, especially for the K^+-terminated tip: for a protruding nanotip (figure 5.12f)), the optimum imaging distance is about 250 pm further away from the sample than for a short nanotip (figure 5.12b)).
As mentioned in paragraph 5.4.1, Bammerlin et al. [98] found that tips with a larger tip radius obtained after repeated crashing gave a higher corrugation. This cannot be directly compared to our calculations, because the the nanotip height was varied rather than the tip radius. However, in the relevant parameter range, changing the tip radius and changing the nanotip height have qualitatively a similar effect on the frequency versus distance data. In agreement with Bammerlin et al., the corrugation increases for a larger van-der-Waals background force in the case of a Br^--terminated tip if the height of the nanotip is decreased from Δz = 360 pm to Δz = 180 pm (figure 5.12e) and c)). However, our calculations also show that choosing a large van-der-Waals background force does not automatically increase the corrugation, but it can also lead to a decrease of the corrugation if the background forces are too large.

Comparison of experiment and theory

The experimental short-range frequency shift data are superimposed on the calculated data in figure 5.12. The van-der-Waals force was fitted to measurements at larger distances. Thus care was taken to use the same origin for the experimental force as for the van-der-Waals force. As a result, the long-range part of the calculated and the experimental forces are in good agreement in figure 5.12.
The calculation of the short-range forces does not rely on any assumptions about the imaging distance. However, it relies on an extrapolation of the van-der-Waals force to close tip-sample distances (< 1 nm), where the assumptions underlying equation 5.4 become doubtful. At these tip-sample distances, the Hamaker approximation is no longer valid and the atomistic structure of tip and sample have to be taken into account. This may introduce some error to the procedure in addition to the a priori unknown offset Δz.
A good agreement between calculated and experimental data is obtained for Δz = 360 pm in the case of the K^+-terminated tip above the Br^--ion and in the case of a Br^--terminated tip over the K^+-ion. However, no agreement for the corrugation at constant frequency shift is obtained. A possible reason is that the model of the tip used for the calculation may not describe the experimental situation. The chemical nature of the tip apex ion or the arrangement of the atoms located at the tip apex could be different in the experiment from the model used in the simulation. In an experiment using a different tip (section 5.4.1), the corrugation was 0.07 nm,

much larger than the corrugation obtained from the frequency versus distance measurement discussed here (0.015 nm). This suggests that the corrugation strongly depends on the atomistic details of the tip apex.

5.6.4 Constant frequency shift images

From the force versus distance data calculated at the 15 different lateral positions, constant frequency shift images have been calculated (figure 5.13). To do that, frequency versus distance data were first calculated from all 15 curves including the van-der-Waals force described above. The height of the nanotip was set to the two extreme values used for figure 5.12 ($\Delta z = 360$ pm and $\Delta z = 80$ pm). For images 5.13a) and b) the experimental frequency shift used in section 5.5, $\Delta f = -26.4$ Hz, was chosen. For the images 5.13c) and d)), a smaller frequency shift, $\Delta f = -17.0$ Hz, had to be chosen, because the frequency shift of $\Delta f = -26.4$ Hz could not be reached at all positions, as evident from figure 5.12e).

As expected, with the Br^--terminated tip, the positions of the K^+-ions correspond to corrugation minima and the positions of the Br^--ions correspond to corrugation maxima. With the K^+-terminated tip the opposite situation occurs[3].

In figure 5.13, differences in the size of the maxima are apparent in images computed at different frequency shifts and at different values of the offset Δz. In the images the grey scale was chosen such that the maximum value corresponds to white and the minimum value corresponds to black as usually done for experimental images. For the line profiles (figure 5.13 e) and f)), the corrugation was normalized to 1 for both nanotip heights and both tip terminations. For the Br^--terminated tip, the line profile obtained with $\Delta z = 360$ pm and $\Delta f = -17.0$ Hz shows a broader maximum at the position of the K^+-ion than the profile obtained with $\Delta z = 80$ pm and $\Delta f = -26.4$ Hz (figure 5.13 e)). Similarly, the sharper K^+-terminated tip shows broader maxima at the position of the Br^--ion. The reason is that images 5.13 a) and b) were calculated at a larger tip-sample distance, as can be seen from the scalebar, than images 5.13 c) and d). The tip-sample distance in these two images is larger although the frequency shift has a larger negative value because the nanotip height is much smaller and therefore a large negative frequency shift is reached at a relatively large tip-sample distance. At large tip-sample distances, as can be seen from figure 5.10, the forces on intermediate positions show similar values as the oppositely charged ions, while at close tip-sample distances, these forces show similar values as the similarly charged ions.

These differences have been analysed in more detail by calculating images at different frequency shifts using different Δz values. For a frequency shift of -100 Hz for the Br^--terminated tip protruding only 80 pm, a calculated image showing broad K^+-ions similar to image 5.13c) was obtained. For a frequency shift of 10 Hz for a K^+-terminated tip protruding 360 pm, a calculated image showing narrow Br^--ions similar to image 5.13b) was obtained.

These trends are in good agreement with experimental results: in figure 5.3a) the maxima of the observed corrugation appear as slightly broader in the region between tip changes 1 and 2, where the tip is retracted (presumably the nanotip protrudes more). The same effect is even more pronounced for figure 5.3c) where the maxima definitely look broader between the tip changes 3 and 4, where the tip is also retracted.

[3] The program used for displaying the images interpolates between the 15 data points [103].

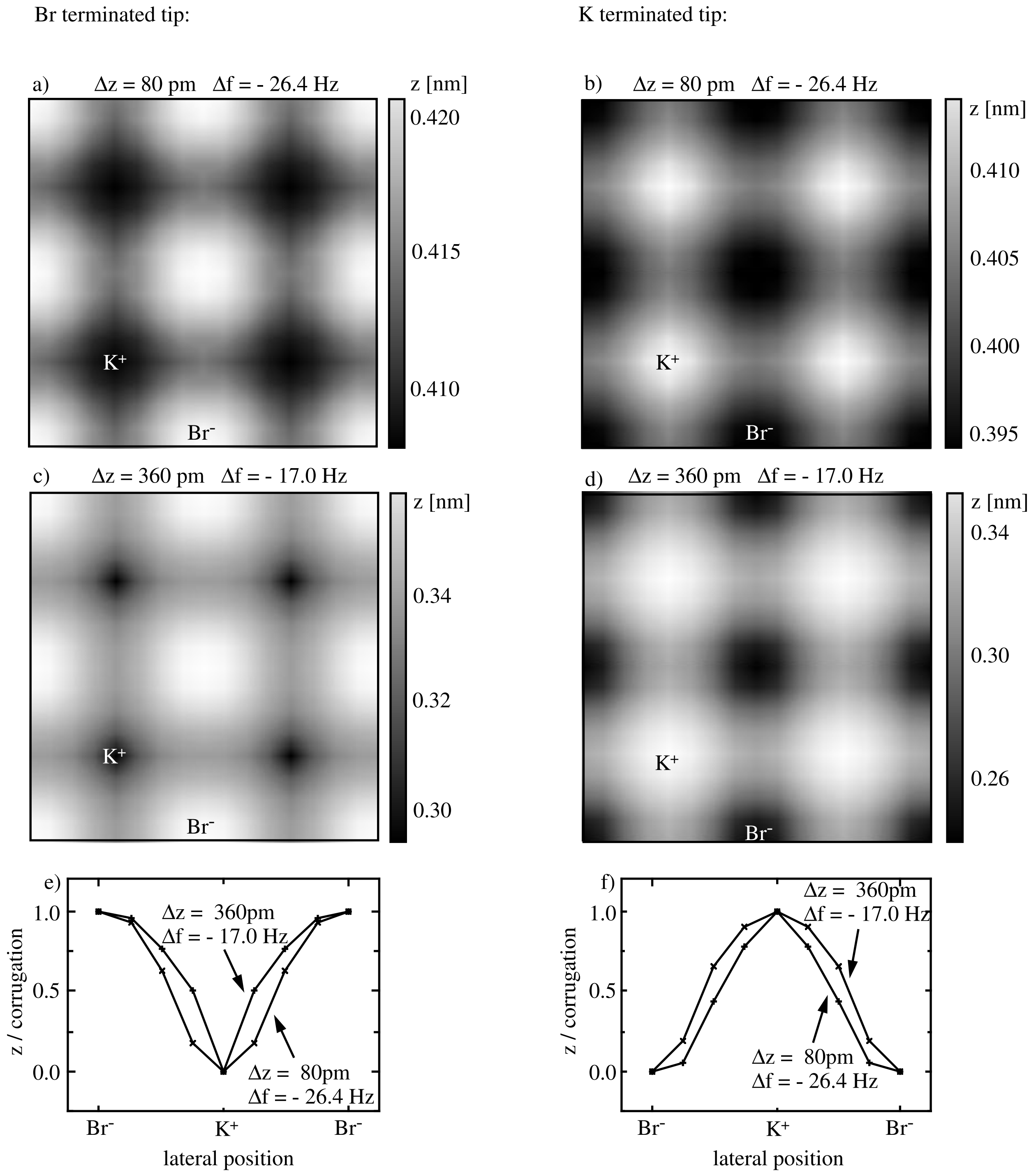

Figure 5.13: a) to d): SFM images calculated from force versus distance data computed from a model that includes the experimental long-range force for two heights of the nanotip (Δz = 360 pm and Δz = 80 pm) for the K^+- and the Br^--terminated tip. e) and f) line profiles along the diagonal of the calculated images; the corrugation was normalized to 1.

name	description	drawing	overall charge
cation vacancy	missing K^+		-e
anion vacancy (α-centre)	missing Br^-		+e
F-centre	electron replacing an anion		0
F'-centre	two electrons replacing an anion		-e
M-centre	aggregate of two F-centres		0
V_k-centre	hole bound to two anions	e^+	+e
U-centre	negatively charged hydrogen replacing an anion	H^-	-e
U_1-centre	negatively charged hydrogen in an interstitial position	H^-	-e
U_2-centre	uncharged hydrogen in an interstitial position	H^0	0

Table 5.2: Some bulk defects in ionic crystals of the NaCl type after [104].

5.6.5 Conclusions

Unlike the Si surface, where covalent attractive chemical bonding forces dominate in the atomic resolution range [35], on the ionic crystal KBr, short-range repulsive forces arise when the ion at the tip apex faces an ion of the same type on the sample. Assuming that the mesoscopic radius of the tip remains constant, reducing the long-range van-der-Waals force by increasing the height of the protruding nanotip does not necessarily increase the obtained corrugation. There is an optimum tip height corresponding to the largest corrugation. If the nanotip protrudes more, imaging is possible only with a very small negative frequency shift.

The frequency shift versus distance data showed qualitative agreement with the experimental data, although the corrugation calculated at the experimental frequency setpoint was stronger. The chemical nature of the apex ion or the arrangement of the ions located at the tip apex could be different in the experiment from the model assumed in the simulation.

It should be possible to distinguish between a positively and a negatively terminated tip even on a simple alkali halide crystal like KBr if a force versus distance measurement above the intermediate position O is performed. Thus, a way of distinguishing between different tips can be proposed, even if no inequivalent sites exist as on CaF_2.

5.7 A point defect on the KBr (001) surface

Defects in ionic crystals and their optical properties have been a field of extensive study as they change the colour of the crystals. For an overview see reference [104] and table 5.14. However, little is known about surface defects since the absorption signal of surface defects is small compared the absorption signal of bulk defects. Additional surface defects not present in the bulk can occur due to interaction with the rest gas. Surface defects can also be created by electron bombardment of ionic crystal surfaces. Stable surface F- and M-centres created by electron bombardment have been studied using LEED and energy loss spectroscopy on thin epitaxial NaCl films grown on Ge (001) [105]. They can be distinguished from the bulk defects by shifts of the absorption peaks.

In scanning force microscopy atomic scale surface defects on ionic crystals have played an important role for proving that true atomic resolution can be achieved on insulators and not only on metals or semiconductors[4]. Atomic-scale defects have been imaged for the first time using non-contact SFM on NaCl by Bammerlin et al. [13]. Radiation induced defects have been studied on KBr [106, 92]. On the CaF_2 (111) surface, defects related to oxygen exposure have been reported [94]. Surface defects and their appearance in SFM images have also been studied theoretically [107]. However so far the identification of these defects in SFM images has been difficult because SFM images do not provide enough information: The geometry of the defect is a convolution of its shape and of the shape of the tip apex. Therefore it has been proposed to combine SFM with other techniques, e.g. local measurement of optical absorption spectra [107] in order to identify defects on ionic crystals. Another problem arises from the diffusion of atomic scale defects on ionic crystal surfaces at room temperature. This may make it difficult to image atomic-scale defects on ionic crystals at room temperature.

5.7.1 Atomic resolution image of an atomic scale defect on KBr (001)

So far we have described results on clean and defect-free KBr terraces. Now an image of an atomic-scale defect on a KBr surface (figure 5.14) will be discussed. This KBr surface has been prepared by cleaving and heating in a similar way as described in paragraph 5.2. No additional procedure that might produce defects was applied. The defect appears in the topography image as a missing minimum, while in the E_{diss} image it appears as a missing maximum. This becomes even more evident in the line sections, taken in the x and y directions through the defect.

The defect could be observed in two successive images. The apparent position of the defect relative to the image frame changed from one image to the next image. This could be due to a movement of the defect on the surface or to a tip change. As the positions of all maxima and minima are different between the two images, a tip change must have occurred between the two images. In the region marked by an arrow in the first image (image 5.14a)), additional noise is measured. This additional noise could be due to a tip instability. However as the positions of the minima and maxima above the scanlines marked by the arrow remains similar to the rest of the image 5.14, the tip change must have occurred between the two images.

The observation of an atomic-scale defect proves that interaction of the tip with the surface is dominated by the interaction of one apex ion. To evaluate this more precisely, the area altered by the defect is determined using the following procedure (figure 5.15):

[4] True atomic resolution can also be proven by imaging steps [93].

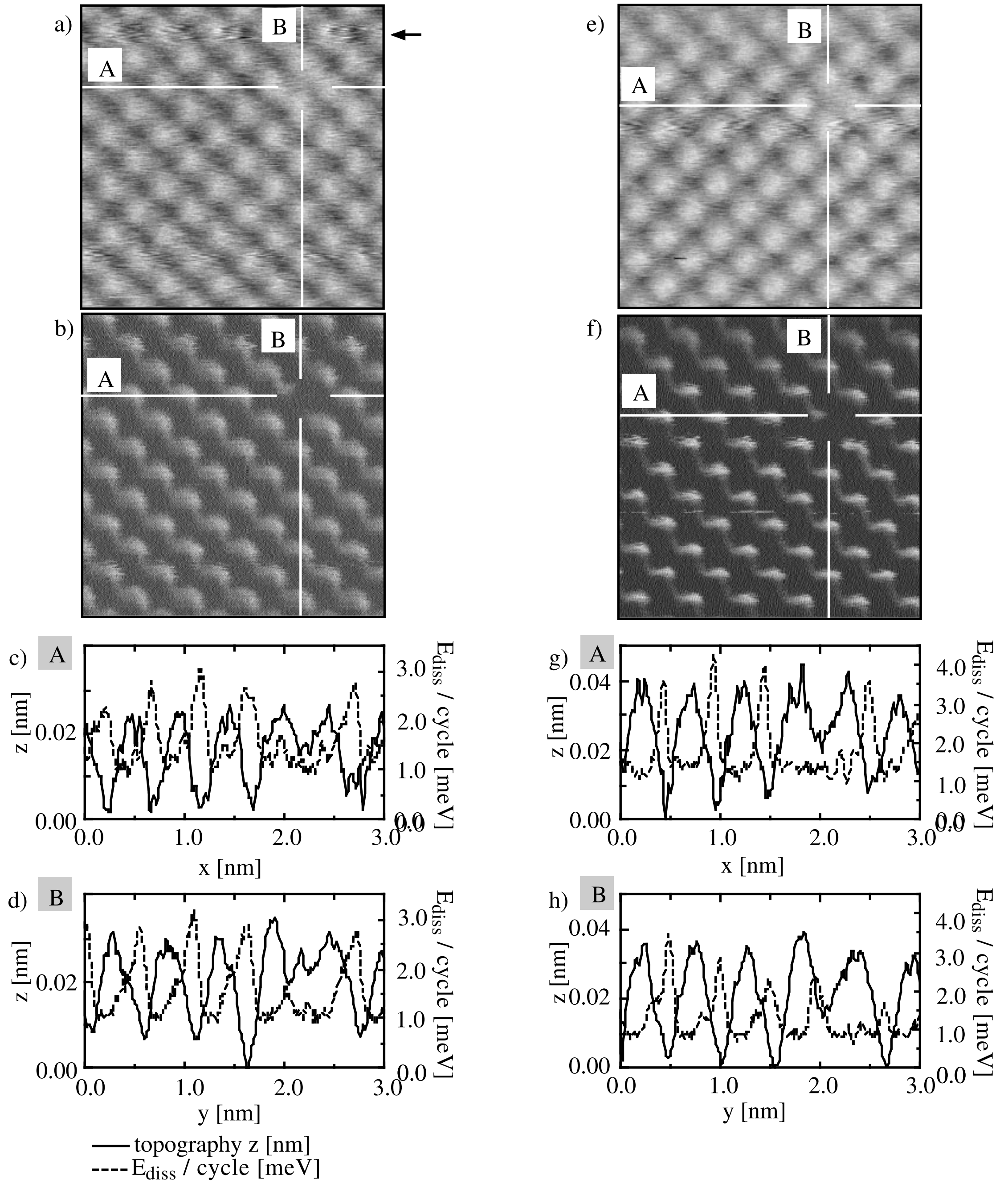

Figure 5.14: a) and e) two successive constant frequency shift images of an atomic scale defect on KBr. b) and f) simultaneously measured A_{exc} converted to dissipated energy per oscillation cycle using equation 2.11. Line profiles of the topography and E_{diss} are shown for each image, in the x direction, c) and g), and in the y direction d) and h). The arrow in image a) points to a few scanlines in which the noise is larger than in the rest of the image, probably due to a tip instability. For this measurement: $c_L = 43$ N/m, $f_0 = 175\ 722.41$ Hz, $A = 5$ nm and $Q = 258\ 000$.

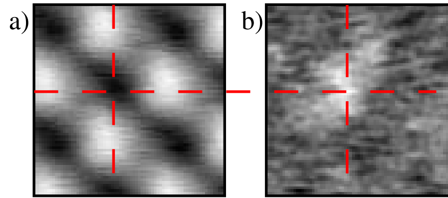

Figure 5.15: a) Averaged image of the KBr surface excluding the defect and b) difference of the averaged image and the defective unit cell.

First, an average image was calculated. An atomic resolution image usually shows repeated constant frequency shift contours of the same object, the surface unit cell. Therefore calculating an average over these repeated measurements can be used to improve the signal to noise ratio. A program has been implemented to perform this averaging procedure yielding the mean value and the standard deviation of the unit cell image. This program has been applied to the atomic resolution image 5.14 a). The average over all unit cells with the exception of those neighbouring the defect has been calculated. The mean frequency shift contour of the surface unit cell (figure 5.15a)) results from the interaction of the surface ions with the tip apex ion or possibly several tip apex ions.
Image 5.15a) was then subtracted from the altered unit cell. The resulting image (figure 5.15b)) shows the area of the defect convoluted with the tip as bright. The defect area is centred on the position of a minimum (repulsive or less attractive short-range interaction) somewhat elongated along the <110> direction of the crystal.
This procedure reveals the contribution of all tip ions to the imaging contrast. If more than one tip ion contributes considerably to the image contrast, a repeated image of the defect with a smaller intensity would be seen in the difference image. This is not the case. The contribution of the neighbouring apex ions to the defect image must therefore be negligible within the experimental noise limit.
As mentioned before, the identification of surface defects is difficult. For a charged defect, the influence of an unshielded electrostatic force on the SFM image is expected to be much stronger than what is observed in figure 5.14. On a perfect overall neutral ionic crystal surface, the periodicity of the charge leads to an exponentially decaying electrostatic force with a decay constant of the order of the lattice constant (see for example equation 2.27 for the analogous magnetic case). An unshielded charge is expected to show a long-range force decaying only proportional to the inverse of the square of the distance. Charged defects have been imaged on the InP (110) surface [108], a semiconductor, where the charge is partially shielded. On the insulator KBr, charge shielding is less effective, therefore the interaction of a charged defect with the tip should be stronger. We therefore assume that the defect is uncharged, or, if it replaces an ion, charged similarly to this ion.

5.7.2 Conclusions

An atomic scale defect has been observed on the KBr surface. Using an averaging procedure over the surface unit cell, it could be shown that the tip used in this experiment was atomically sharp and that true atomic resolution is achieved. The contribution of one tip apex ion to the image contrast is much stronger than the contribution of other ions which is negligible compared to the experimental noise. The defect is uncharged, but its nature could so far not be identified

unambiguously.

5.8 Water on KBr (001)

When KBr crystals are cleaved in air, they are exposed to moisture. It is possible that adsorbed water changes the properties of the surface. The surfaces of ionic crystals exposed to water have been studied by Miura et al. with SFM on a large scale [109]. These surfaces show large terraces with rounded steps instead of the straight cleavage steps observed on a clean surface (see for example figure 5.1). The atomic-scale arrangements of water molecules on ionic crystal surfaces and their symmetry have been analysed using diffraction techniques. One group studied NaCl surface with second harmonic generation and reported a loss of the fourfold symmetry associated with the NaCl surface while retaining a mirror symmetry after two days of exposure to air moisture [110]. This mirror symmetry was then lost after three days of exposure. The conclusion was drawn that water first polymerizes forming chain-like structures. The preferential direction of these structures was reported to have a component parallel to the (100) direction (the incident light was parallel to the (010) direction.) Another group studied the water covered NaCl surface using helium atom scattering but reported only isotropic diffraction [111]. Using LEED (low energy electron diffraction) on a 1 nm thin NaCl film on a Ge (001) substrate, a c(4x2) reconstructed structure was found [112].
Sometimes, after cleavage of KBr in air, our large scale images obtained showed large flat areas with rounded steps (figure 5.16) in contrast to the large-scale image presented in figure 5.1. No charged defects are visible on the rounded steps. All step heights are similar to the KBr unit cell height (no double steps occur). Tip crashes are without any noticeable effect for the tip or for the sample. The structures look similar to the structures observed by Miura et al. [109].
If such a surface is imaged with atomic resolution, sometimes chain like regular structures are resolved. This contrast cannot be explained by an interaction of the surface with several tip asperities because defects are visible in the structures. The corrugation is small compared to image 5.2. In the images shown above, the (100) direction of the KBr crystal is approximately parallel to the y direction.
These structures are interpreted as resulting from water absorbed on the KBr (001) surface. However to prove that the structures are related to water, a clean crystal should be exposed to water vapour and the changes should be monitored.

5.9 Conclusions

The first site-specific force versus distance measurements of the weak interaction between a sharp tip and an insulator were presented. It was possible to describe the very weak long-range force using a Hamaker like model of the van-der-Waals interaction. The atomic details of the tip apex were found to play a strong role in the contrast obtained in atomic resolution images. Switches in contrast are related to changes of the atomic structure of the tip apex.
Atomistic simulations of the tip-sample interaction of a KBr (001) tip with a KBr surface show that unlike the Si (111) surface, where covalent attractive chemical bonding forces dominate [35], on the ionic crystal KBr, short range repulsive forces arise when the ion at the tip apex faces an ion of the same sign on the sample. Assuming that the mesoscopic radius of the tip remains constant, reducing the long-range van-der-Waals force by increasing the height of the protruding

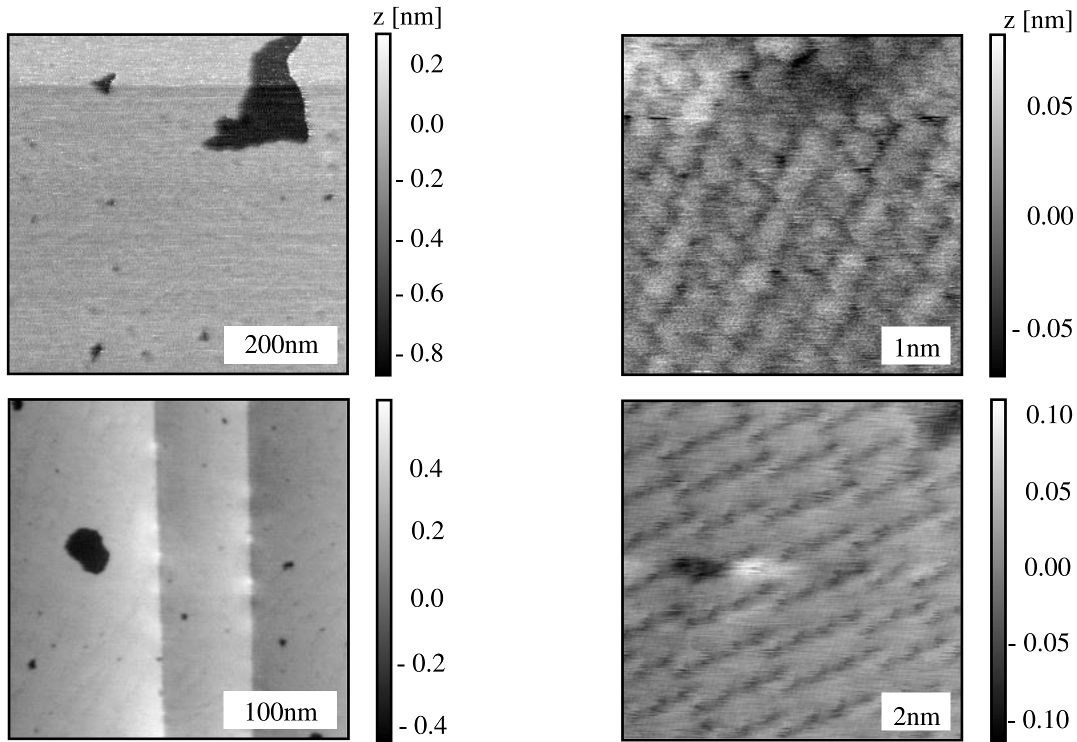

Figure 5.16: Large-scale and atomic-resolution images for a cleaved KBr crystal covered with water. Left, large-scale images, right corresponding images with atomic resolution.

nanotip does not necessarily increase the obtained corrugation. There is an optimum tip height corresponding to the largest corrugation. If the tip protrudes more, imaging is possible only with a small negative frequency shift.
The frequency shift versus distance data showed qualitative agreement with the experimental data, although the corrugation calculated at the experimental frequency shift setpoint was much larger. The chemical nature of the tip apex ion or the arrangement of the atoms located at the tip apex could be different in the experiment from the model used in the simulation.
It is possible to distinguish between a positively and a negatively terminated tip, if a force versus distance measurement above the bridge site located between two neighbouring Br^{-}-ions and two neighbouring K^{+}-ions is performed. Thus, a way of distinguishing between different tips exists, even though if all cation and anion sites are equivalent.
From the analysis of the observed monoatomic defect, it can be concluded that the tip used in this experiment is atomically sharp and that true atomic resolution is achieved. The contribution of the tip apex ion to the image contrast is much stronger than the contribution of other ions. The contribution of other ions is negligible compared to the experimental noise. This result was obtained by subtracting an average image, where the average over many defect-free unit cells was calculated. The defect is uncharged, but its nature cannot be identified.

Chapter 6

Atomic resolution imaging and frequency versus distance measurements on NiO at low temperatures

6.1 Introduction

While atomic resolution on non-magnetic systems is often obtained in scanning force microcopy, the resolution limit for imaging magnetic structures with magnetic force microscopy (MFM) is still rather high, on the order of about 40 nm. This limit arises in part from the relatively large tip-sample spacings used in MFM and the long decay of the magnetic stray field probed at these distances. It is, however expected that at smaller tip to sample distances, exchange forces may lead to atomic scale magnetic contrast. Recently, calculations have shown that these forces are expected to be of a magnitude that is measurable with scanning force microscopy (SFM, about 0.1 nN) [19, 20]. An attractive system for measuring magnetic exchange forces with SFM is NiO. This sample is appealing for several reasons: NiO is an antiferromagnetic insulator with a spin direction that has a large component perpendicular to the surface plane for part of the magnetic domains present (figure 6.1) [113]. This well defined magnetic structure should simplify the interpretation of images exhibiting atomic scale contrast resulting from exchange forces. In addition, a clean NiO surface can easily be prepared by cleaving and atomic resolution has already been achieved on cleaved NiO surfaces by SFM [114, 22] as well as scanning tunneling microscopy (STM) [115]. Inspite of these favourable properties, the attempts of several groups to measure exchange forces on NiO have not been successful so far. One possible reason for this is that the exchange forces may be relatively weak at the imaging distance and that tip and surface atom relaxation effects prevent a further approach to the surface, as proposed by simulations [116]. We therefore decided to investigate the short-range interaction between an SFM tip and a NiO sample using site-specific frequency versus distance measurements [35] and to look for signs of relaxation. In this short-range interaction regime, energy losses which vary on the atomic scale are also often observed [117]. Recently, it has been proposed that hysteretic relaxation of tip or surface ions is responsible for this energy dissipation [50]. However, hysteretic relaxation is only one of several proposed mechanisms for the observed energy dissipation. Other

hypothesis suggest that surface phonon modes [47, 48], electrical hysteresis [45, 46] or even the detection electronics [42, 43] can generate apparent or real energy losses. In this paper, we present site-specific frequency and dissipation versus distance measurements on a NiO surface. These measurements indicate that significant relaxation effects occur at small tip-sample spacings and support the hypothesis that hysteretic relaxation is at least partially responsible for the observed energy dissipation.

6.2 Antiferromagnetic materials and magnetic imaging on the atomic scale

6.2.1 Antiferromagnets

Exchange forces can in principle be measured on any ferromagnetic or antiferromagnetic sample. However, in order to prove that the measured forces are of magnetic origin, a sample of known spin structure is needed. In order to measure the atomic scale contrast due to exchange forces using a ferromagnetic tip, a sample is needed that has a surface in which the magnetic moments of neighbouring atoms alternate and where the magnetic moments are perpendicular to this surface[1]. All antiferromagnets fulfil the condition that neighbouring atomic moments alternate their direction. Magnetic ordering occurs below a certain temperature, called the Néel temperature. Above this temperature, an antiferromagnet is paramagnetic. However, the direction of the spins relative to the crystallographic axes strongly depends on the material. It cannot easily be modified for example by applying a magnetic field of a few Teslas like in the case of ferromagnets, because antiferromagnets do not emit a macroscopic magnetic field[2]. Therefore, the choice of the material is crucial for being able to measure exchange forces.

6.2.2 Overview of the literature on atomic scale imaging of antiferromagnetic samples

Candidates for exchange force measurements include antiferromagnetic metals (Cr and α-Mn) or antiferromagnetic oxides or compounds. The antiferromagnetic properties of Chromium thin films and surfaces have been studied extensively by neutron diffraction [118]. The (001) surface of thin Cr films deposited on Fe(001) have been studied by spin-polarized STM [17]. However it is difficult to obtain clean Cr(001) surfaces [119] and this surface shows no alternating magnetic moments.

Antiferromagnetic Manganese has been stabilized on a W(110) surface and the variation of the magnetic moments has been measured at the atomic scale by spin-polarized STM [18].

The (001) surfaces of the antiferromagnetic oxides NiO and CoO have been studied by STM [115]. The corrugation amplitude was larger on NiO than on CoO. The antiferromagnetic surface structure of a NiO thin film grown on MgO has been studied locally by X-ray magnetic dichroism spectroscopy [120]. From these studies, the conclusion that the magnetic moments of the thin NiO film point out of plane was drawn. The magnetic properties of a NiO thin film grown on Ag have been studied by spin-polarized photoemission spectroscopy [121]. These studies suggest

[1]The tip magnetization is assumed to be parallel to the tip i.e. perpendicular to the sample because of shape anisotropy.

[2]In some antiferromagnets the direction of the spins can be influenced by applying stress or by field cooling the sample.

that the magnetic moments of NiO lie in the surface plane. Another synchrotron radiation study using X-ray linear magnetic dichroism in photoemission microscopy suggests that cleaved crystals of NiO show bulk terminated magnetic moments while sputtered surfaces show in plane magnetic moments [122]. From LEED studies it is known that the NiO surfaces obtained by cleaving are flatter than other transition metal oxide surfaces [123].

As mentioned before, calculations have shown that exchange forces are expected to be of a measurable magnitude [19, 20]. However, in these calculations, relaxation effects were not taken into account. Calculations by Livshits et al. suggest that the imaging distance on ionic crystals is of the order of $0.3 - 0.5$ nm [124]. If the imaging distance on NiO is similar, the overlap of the wavefunctions responsible for magnetism (the d-wave function for Ni) may be too small at this distance to measure exchange forces. However, frequency versus distance measurements allow a closer approach to the surface than atomic resolution imaging [35]. Foster and Shluger calculated force versus distance data on a NiO surface using various tips including metal tips [116]. For a tip made of a reactive metal, this could be for example Fe, the force versus distance data obtained above the oxygen ion shows two instabilities: one where the oxygen ion under the tip starts to jump to the tip and one where the next nearest oxygen ions jump towards the tip. These instabilities limit the closest imaging distance to the surface. Similar instabilities have been calculated for the InP surface by Ke et al. [125] and could be related to nondestructive STM imaging at very small tip to sample distances of about $0.2 - 0.3$ nm.

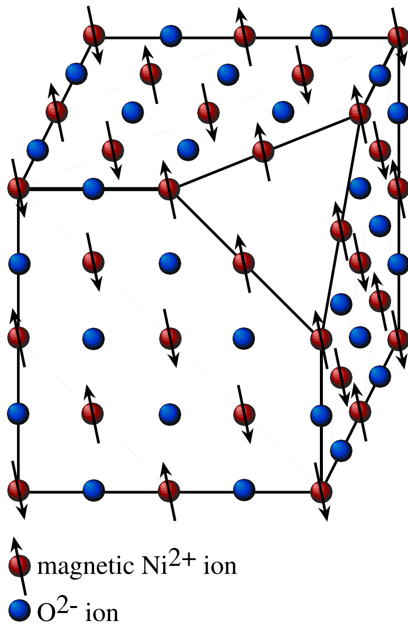

Figure 6.1: Sketch of the full magnetic unit cell of the NiO crystal.

6.2.3 The antiferromagnetic structure of NiO

In an antiferromagnet, there are two characteristic directions: the direction in which the variation of the magnetic moment takes place, and the direction in which the magnetic moments point. The first is called the $\vec{k}$ or $\vec{q}$ direction; the second is called $\vec{S}$ direction. In NiO the $\vec{k}$ direction is parallel to the crystallographic <111> direction. Therefore there are four possible domains

T-domain	$[111]$	$[\bar{1}11]$	$[1\bar{1}1]$	$[11\bar{1}]$	approximate spin direction relative to the surface
S-domain	$[\bar{2}11]$	$[211]$	$[21\bar{1}]$	$[2\bar{1}1]$	$\parallel$
	$[1\bar{2}1]$	$[12\bar{1}]$	$[121]$	$[112]$	$\parallel$
	$[11\bar{2}]$	$[1\bar{1}2]$	$[\bar{1}12]$	$[\bar{1}21]$	$\perp$

Table 6.1: Possible directions of the spins within one T-domain in NiO. In each T-domain only one third of the S domains has the desired orientation perpendicular to the surface. See for example [122].

(called T-domains) of four different $\vec{k}$ directions[3]. In one of these domains, all magnetic moments in one (111) plane have the same spin direction, in the next plane they have the opposite direction and so on (figure 6.1).
The magnetic ordering in NiO in the <111> direction is related to a structural change. Above the Néel temperature (T_N = 520 K [126]), the paramagnetic crystal is cubic face centred, whereas below the Néel temperature, the unit cell is slightly compressed in the $\vec{k}$ direction of the T-domain. This causes twinning of the single crystal when it is cooled below the Néel temperature[4]. These domains can easily be observed by diffraction techniques with local resolution, as the size of these domains is between μm and mm depending on the preparation procedure [127]. Single T-domain samples can be prepared by applying stress while cooling the sample through the Néel temperature.
The $\vec{S}$ direction in NiO is perpendicular to $\vec{k}$ and parallel to the family of <211> directions within the (111) plane. There are twenty-four equivalent [211] directions in fcc crystals, but twelve are just the opposite sense of the other twelve, and lead to the same antiferromagnetic configuration. The remaining twelve directions can be divided in four groups according to the T-domain they belong to (table 6.1). S-domains have been observed by neutron diffraction in a single T-domain sample [9]. Of all domains present in our sample, one third have the desired orientation of the spins perpendicular to the sample surface.

6.3 Tip and sample preparation

NiO crystals were purchased from Mateck, Jülich, Germany and Kelpin, Neuhausen, Germany. Atomically clean and flat surfaces were prepared by cleaving the crystals in ultrahigh vacuum. All SFM measurements were carried out in our home-built UHV low temperature SFM at about 7 K [24]. We used silicon cantilevers provided by Nanosensors, Wetzlar, Germany with a force constant of about 40 N/m and a resonance frequency of about 170 kHz. After introducing a tip into ultrahigh vacuum it was cleaned by heating to 150° C for 1 h. We therefore believe that our tips were originally covered with SiO_2. The SFM measurements were carried out in dynamic SFM mode with a constant cantilever oscillation amplitude of 5 nm.

6.4 Large scale images

A large scale image obtained on a freshly cleaved NiO surface is shown in figure 6.2 a). The surface shows cloudy structures with periodic patterns. The image resembles a large scale image shown in reference [114]. In this reference, the structures were interpreted as higher-indexed vicinal faces. A similar surface rumpling was observed by STM on annealed CoO(001) [128].

[3] Opposite directions lead to identical T-domains.
[4] This is why these domains are called T-domains, T stands for twin.

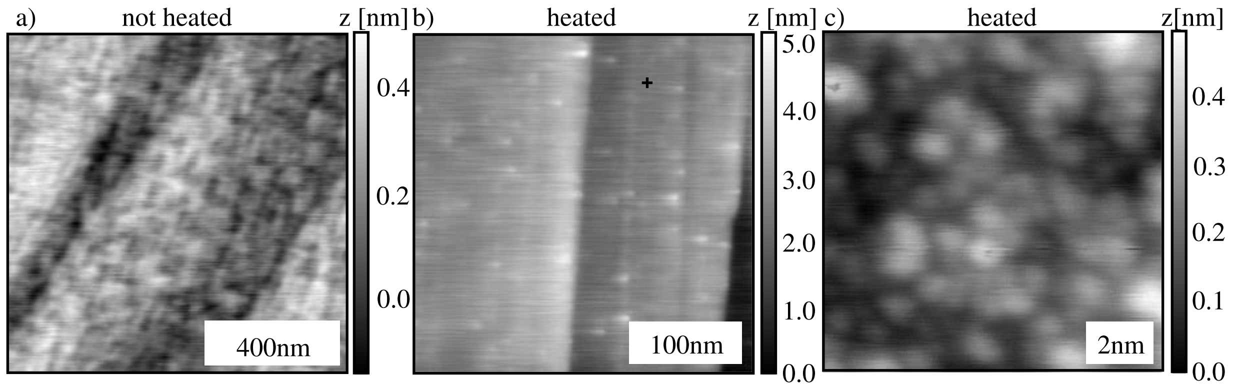

Figure 6.2: a) Large scale image of a NiO crystal that has not been annealed. b) Large scale image of an annealed NiO crystal. Image c) is a higher resolution image at the position marked by a cross in image b).

However, LEED studies of the NiO(001) surface show that the quality of the cleaving is highest on NiO compared to other antiferromagnetic oxides, and that no surface rumpling occurs [123]. Another possible explanation is that the surface structures do not result from topographical features but from localized charge on the surface. This is supported by the observation that the structures are no longer observed after heating the crystal to 200° C for 1 h (figure 6.2 b)). On heat-treated NiO straight steps and some point-like defects are observed. The large scale image shown in figure 6.2 b) resembles another large scale image shown in reference [114]. In this ref. no difference between the treatment of the two NiO surfaces is mentioned. Although the surface shown in image 6.2b) shows apparently flat terraces on a large scale, the small scale image 6.2 c) reveals that the surface is rough. It was not possible to achieve atomic resolution on such a surface. All atomic resolution measurements on NiO shown in this thesis were obtained on crystals that had not been annealed[5].

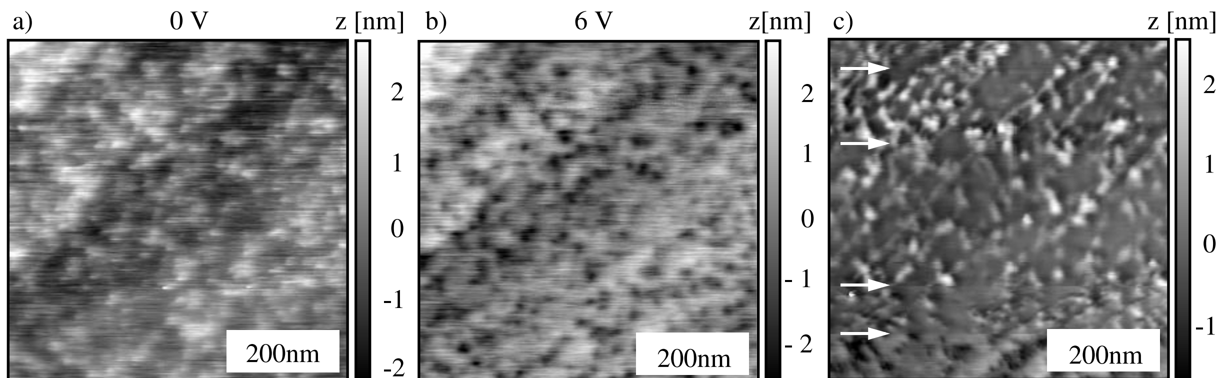

Figure 6.3: Large scale image of an annealed NiO crystal. In image a) the sample bias voltage was zero, while in image b) 6 V were applied to a Cu plate under the sample. c) Large scale image of an annealed NiO crystal with tip changes marked by arrows.

In order to further investigate the origin of the observed structures, large scale images of annealed

[5]Images of the same size as image 6.2c) showed a flat surface.

NiO surfaces have been acquired at different bias voltages applied to a copper plate mounted directly under the NiO crystals (figure 6.3 a) and b)). Changing the applied bias voltage by 6 V causes a contrast inversion of the point-like defects. A similar effect is produced by tip changes (figure 6.3 c)).

The most dramatic tip changes in NiO occur if the tip is crashed into the surface: The feed-back-system that controls the distance to the surface relies on a decrease of the cantilever resonance frequency when the sample surface is approached. As the tip approaches the surface, the frequency reaches a minimum and then increases again and the slope becomes positive. If the frequency shift setpoint value is not reached while approaching the surface, the tip approaches to the surface even further until the cantilever oscillation amplitude starts to decrease. In order to avoid a tip crash, the tip was automatically retracted, as soon as the oscillation amplitude fell below a threshold value set by the experimentalist. In order to implement this automatic retraction, the z-controller code was modified. This automatic tip retraction feature prevents significant modification of the tip during a tip crash and it is therefore possible to continue to use a tip after such an event.

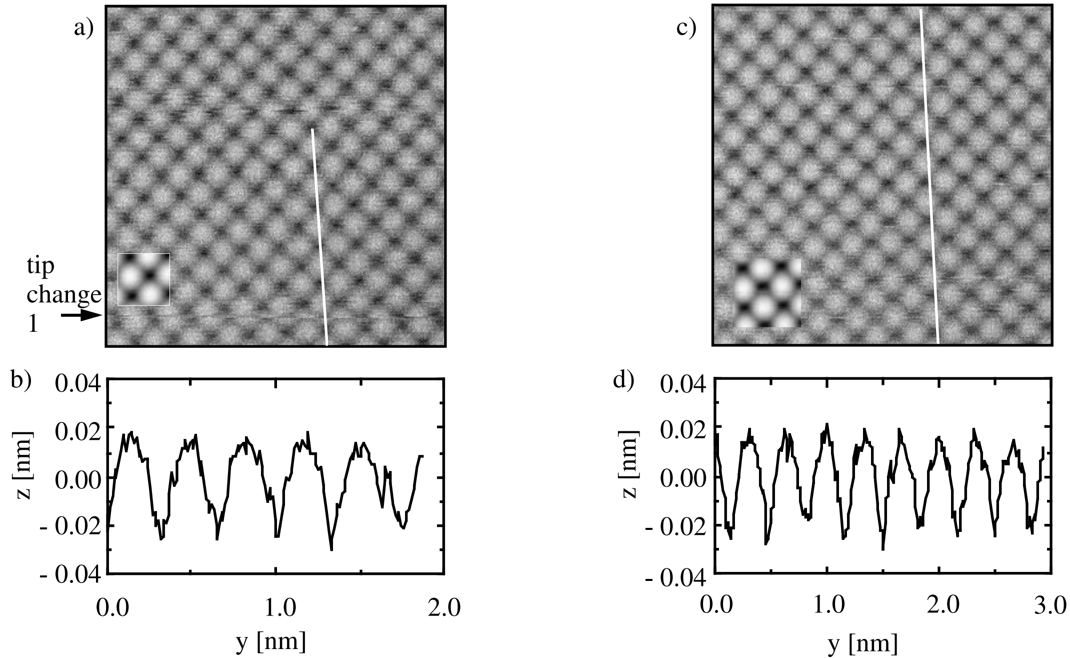

Figure 6.4: Images obtained on the NiO crystal before and after measuring frequency versus distance data. The frequency shift was -86 Hz ($\Gamma = 8.04 \cdot 10^{-15}\text{Nm}^{0.5}$) in a) and in c), the oscillation amplitude was 5 nm and the voltage applied for compensating the surface charge was 5.3 V. In each of the two images an inset shows an averaged image obtained by averaging over all unit cells as described in chapter 5.7. In b) and d) the line sections marked by white lines in images a) and c) are shown.

6.5 Atomic resolution images

Atomic resolution images were obtained on several NiO crystal surfaces. Figure 6.4 shows two such images acquired at a frequency shift of -86 Hz ($\Gamma = (\Delta f/f)c_L A^{3/2} = 8.04 \cdot 10^{-15}$ $\text{Nm}^{0.5}$). The imaging atom was picked up from the NiO sample during initial imaging of the surface

and was therefore most probably either Ni or O. The atomic scale contrast observed on the NiO surface with such a tip resembles the contrast obtained on ionic crystals such as KBr and NaCl. We observe one maximum and one minimum within the unit cell of a square lattice. The corrugation originating from the constant frequency shift contours in this case was 40 pm, significantly larger than the value of 20 pm obtained with an Fe tip in reference [22]. Unfortunately, the corrugation for a Si tip is not given quantitatively in this ref. We also note that we did not observe atomic scale magnetic contrast, a finding that is consistent with the observations of Hosoi et al. [114] and Allers et al. [22]. One possible reason for the lack of magnetic contrast in all of these experiments is the uncertain nature (i.e. chemical species, magnetic spin state, etc) of the atom at the tip apex. Another possible reason is that an instability of the tip or sample ions prevents imaging at distances close enough to measure exchange forces. This hypothesis can be investigated by analysing frequency versus distance measurements.

6.6 Tip instability

The experiment was performed in a way similar to that described in reference [35]: before and after each frequency versus distance measurement, an image was acquired to monitor tip changes. Three tip changes occurred in the course of the experiment including imaging and acquiring frequency versus distance measurements: The tip change (denoted tip change 0) which occurred before atomic resolution was obtained, has already been mentioned. During acquisition of one of the images another tip change occurred (labelled 1 in figure 6.4 a)). In this image, the maxima and minima of the corrugation appear to shift due to the tip change. After tip change 1, the tip remained stable in the new configuration and more frequency versus distance measurements were performed and SFM images acquired. The closest distance to the sample in the frequency versus distance measurements was gradually decreased until a tip change occurred during the last frequency versus distance measurement acquired above the topographic minimum (tip change 2 - see figure 6.6a)). After this event, an image of the surface was acquired (figure 6.4c)) in which the positions of the maxima are similar to that observed between tip changes 0 and 1 in the image acquired before the frequency distance experiments (lower part of figure 6.4a). We also note that small changes in the details of the contrast such as the height of the corrugation can be observed as is often the case after a tip change. It is also important to note that because tip change 2 occurred during the last frequency distance measurement, this tip change does not influence the interpretation of the frequency distance data acquired before the tip change, including the data acquired immediately before the tip change. We conclude that there must have been two or more different positions of the imaging ion on the tip which were occupied during the measurements. However, as the condition of the tip was monitored during the experiment, this observation is independent of the interpretation of the force versus distance data.

6.7 Frequency versus distance measurements

Long-range (z-range 25 nm) and short-range (z-range 2 nm) frequency versus distance experiments were performed. The acquisition time for each approach and retraction was $2 \cdot 30$ s. The parameters of the cantilever used were: resonance frequency $f_0 = 162\ 668.67$ Hz, longitudinal spring constant $c_L = 43$ N/m and oscillation amplitude $A = 5$ nm, quality factor of the oscillator $Q = 100\ 000$.

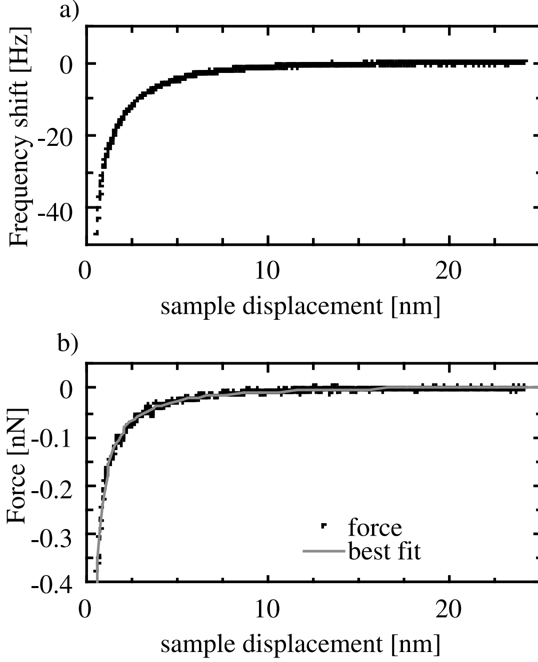

Figure 6.5: a) Frequency shift data obtained in the distance regime up to 23 nm on the NiO surface. b) Force calculated by numerical inversion and best fit.

6.7.1 Analysis of the frequency versus distance data

For both the short-range and long-range experiments the approach and retraction measurements were identical within the experimental noise limit. Repeated measurements yielded the same results. The long-range data is shifted relative to the short-range data because of the piezo-electric creep effect. This effect can be compensated by shifting the z-axis offset of the long-range data with respect to the short-range data by 0.14 nm (figure 6.5 shows the shifted data). To show the resulting match of the two sets of data, the long-range data is shown together with the short-range data in figure 6.6a).

The oscillation amplitude used here (5 nm) is large compared to the decay length of the frequency shift. In the large amplitude mode, a simple linear relationship exists between the force and the measured frequency shift and the frequency shift can be transformed into a force using the iterative method developed by Dürig [28] (see chapter 2.4.2). One iteration was enough to obtain convergence. The results are shown in figure 6.5 b and figure 6.6 b. The large frequency shift measured in the long-range regime can only be explained by a considerable capacitive force which probably results from uncompensated charge on the sample surface produced during cleaving of the sample. As the electrostatic force is in this case much larger than the van-der-Waals force, the long-range force data can be well described by a model of the long-range electrostatic force, neglecting the van-der-Waals force. We used a function that describes the electrostatic force acting between a cone with a spherical cap and a flat surface [36, 38] (see chapter 2.6.1).

$$\begin{aligned} F_{\mathrm{el}}(z) \; = \; & -\pi\varepsilon_0 \cdot (\Delta V)^2 \cdot \left[\frac{R}{z} + c^2(\alpha) \cdot \left(\ln \frac{l_{\mathrm{tip}}}{z + R_\alpha} - 1 \right) \right. \\ & \left. - \frac{R \cdot (1 - c^2(\alpha) \cos^2 \alpha / \sin \alpha)}{z + R_\alpha} \right] \end{aligned} \quad (6.1)$$

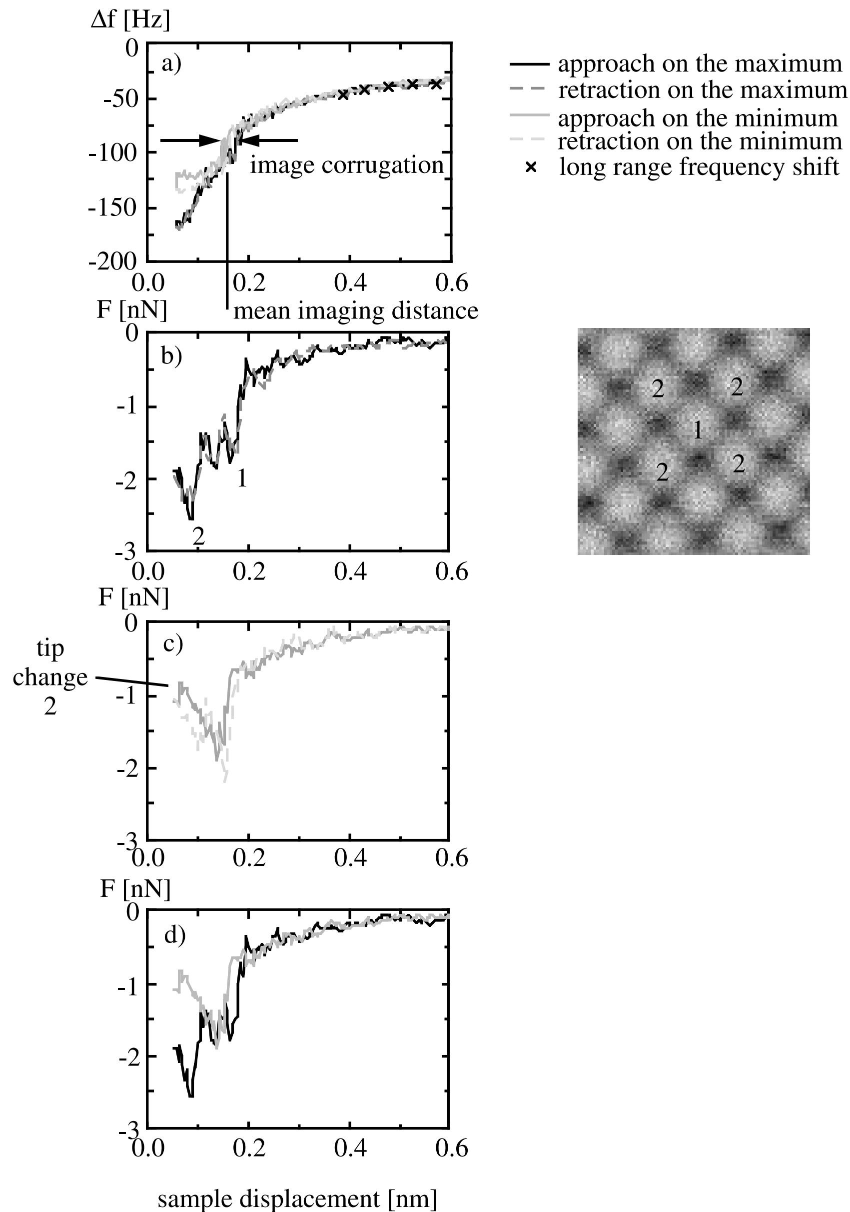

Figure 6.6: Short-range frequency (a) and force versus distance data on NiO. b) shows the force measured during approach and retraction on the maximum and c) shows the force measured during approach and retraction on the minimum. d) shows the force measured during approach to the surface on the maximum along with the force measured during approach to the surface on the minimum. On the maximum a plateau is visible that relates to interaction with not only with foremost atom at the tip apex and the atom located at the site of the maximum but also to the next nearest neighbours in either the tip and/or sample. Calculations suggest an interaction with the next nearest surface atoms labelled 2 when measuring over the maximum 1 (see text). In the retraction data acquired over the minimum, a tip change occurs, labelled tip change 2 as discussed in the text.

where ΔV is the voltage difference, R is the tip radius, α is the cone angle, $R_\alpha = R(1 - \sin\alpha)$ is the height of the spherical cap, $c(\alpha) = 1/ln(\cot(\alpha/2))$ and l_{tip} is the tip length. During fitting, α was fixed to 10° and l_{tip} was fixed to 1 μm. The best fit was obtained with $\Delta V = 0.84$ V and $R = 10.7$ nm. The tip radius obtained from the fit is in good agreement with the value given by the manufacturer $R < 10$ nm. The long-range force obtained by the inversion and the best fit are shown in figure 6.5. The agreement is excellent in the range of 0 to 10 nm.

6.7.2 Short-range forces

The short-range site-specific frequency shift data is shown in figure 6.6 a). Comparing the frequency versus distance data measured above the local topographic maximum and minimum, we see that the corrugation, i.e. the difference in sample displacement at constant frequency shift, is in agreement with the corrugation observed in figure 6.4 (0.04 nm) within the experimental noise. The approach and retraction data match exactly for the data obtained above the maximum (figure 6.6 b), while a jump occurs at the end of the data acquired during approach above the minimum (figure 6.6 c). This is tip change 2 mentioned above.

At tip-sample distances below 1 nm, the force acting on the tip results from both long-range electrostatic forces and short-range chemical bonding forces or short-range electrostatic forces (figure 6.6). After conversion of the frequency shift data to force, the long-range force obtained by fitting can be subtracted from the total force in order to reveal the short-range component. The results are shown in figure 6.6 b). The forces obtained above the maximum and the minimum are both attractive. The maximum value of the force obtained is 1.6 nN above the minimum and 2.3 nN above the maximum, about ten times larger than the forces measured on the KBr surface 5. These values can be compared with the results of calculations by Foster and Shluger [116] designed to model the short-range forces acting between a SFM tip and a NiO surface. In their calculations, Foster and Shluger have used different tips and found a large range of maximum attractive forces between 3 nN for a Pd tip and 25.6 nN for a tip made from reactive metal M*. (This could be for example Fe.). The maximal force found from our measurements of 1.6 nN on the minimum and 2.3 nN on the maximum is closer to the values obtained by Foster an Shluger with Pd tips than to the value obtained with M* tips. The force decays from the maximum value to $1/e$ within about 0.1 to 0.2 nm similar to the decay length calculated by Foster and Shluger. The distance to the surface where the image was acquired can be estimated by extrapolating the repulsive branch of the force versus distance data to the point where it crosses the zero force axis. Then, if the assumption that the imaging ion is Ni or O is correct, and the tip-sample interaction above the minimum is dominated by the interaction between a single pair of atoms in the tip and sample, the distance where the force on the tip ion is zero should correspond to the binding length of NiO (0.284 nm [126]). In figure 6.6 the data has been shifted such that the extrapolated zero crossing of the force occurs at $z = 0$. The mean imaging distance is 0.18 nm from this point giving a total average imaging distance of 0.36 nm. This value is estimated to have an error not larger than ± 0.1 nm. It is also interesting to note that the imaging distance corresponds to the position of a steep gradient in the force versus distance data (position 1 figure 6.6b).

An interesting feature of the force measured above the topographic maximum is the oscillation with a period of about 0.09 nm that is clearly observed in the force versus distance data measured above the local topographic maxima (figure 6.6b). This oscillation is also visible in the raw frequency shift data where the local minima in the force data correspond to a change in curvature

of the frequency shift data. The observation of the oscillation in the raw frequency shift data clearly indicates that the observed force oscillation is not due to an artefact of the deconvolution process. In addition, we note that the period of the oscillation is significantly larger than the sampling period of the frequency shift data, further indicating that it is not an artefact of the deconvolution process. It is also important to note that the oscillation in the force is observed at the same tip-sample spacing in both the approach and retraction curves as well as in repeated experiments above the same point, eliminating the possibility that it results from electronic or mechanical noise. A possible explanation for this feature is the increasing contribution to the measured force of nearest neighbour atoms in either or both the tip or sample as the tip-sample spacing is reduced. A similar feature has previously been predicted by Foster and Shluger [116] who modelled the interaction of various tips with a NiO surface as well as by Ke et al. [125] who modelled the interaction of a tip with a GaAs surface. The calculations by Foster show that the oscillation is due to strong relaxation of the next nearest neighbouring ions on the surface: if the tip made from reactive metal is placed above an oxygen ion of the NiO surface, its next nearest oxygen neighbours move towards the tip as the tip approaches the surface. The distance between the two steep gradients observed in our experiment is about 0.09 nm in the experiment and 0.15 nm in the simulation. The total distance to the surface of the interaction with the next nearest neighbours is larger (0.08 nm, a total tip-sample distance of 0.364 nm taking the bonding length of 0.284 nm for NiO into account) in the experiment compared to the simulation (0.23 nm). We therefore conclude that the relaxation observed experimentally is stronger than the one calculated as was also observed on the Si(111) 7×7 surface [35]. This could be due to a relatively weak binding of the NiO cluster to the SiO_2 covered tip. As mentioned, the forces calculated by Foster and Shluger are about ten times larger than the forces observed experimentally. However such strong relaxation and interaction of several atoms of the tip with the surface also occurs for forces of the order of 1 nN in the calculations by Ke et al. [125]. In these calculations, the oscillations are due to an interaction of one of the tip atoms located one layer behind the imaging atom with a neighbouring Ga atom when measuring above an As atom. Ke et al. also find a tip instability with an abrupt change in force when approaching the Si tip above an As atom. Although an abrupt change in the frequency shift as we have observed it on the minimum (tip change 2) cannot directly be compared to the tip instability calculated by Ke et al., it is striking that multiatom interactions seem to occur above on one kind of atom and tip changes are present on the other kind of atom in both the experiment and the calculations. It is important to note that multiatom interactions do not seem to play a role above the maximum at the imaging distance, and similarly it does not seem to influence the force versus distance data acquired above the minimum in both the calculations and the experiment. After the frequency versus distance data was acquired, the tip was approached further to the sample to a total frequency shift of -102.0 Hz ($\Gamma = 9.53 \cdot 10^{-15}$ Nm$^{0.5}$) and an image was acquired. The corrugation increased to about 0.05 nm before a destructive tip change occurred during image acquisition.

6.8 Energy dissipation

Several mechanisms are currently discussed as possible origins of atomic scale variations in the excitation amplitude necessary to maintain the cantilever oscillation at a constant amplitude. One of the mechanisms that could lead to energy dissipation is hysteretic movement of atoms[48, 50]. Therefore, if a movement of atoms is detected, like the strong relaxation effects discussed in the last paragraph, the question arises whether this movement is related to dissipation. In

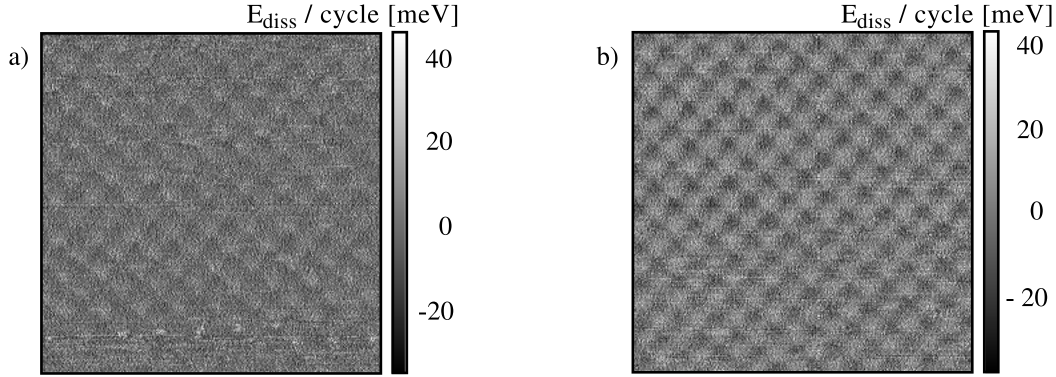

Figure 6.7: a), b) Dissipated energy per oscillation cycle acquired simultaneously to images 6.4a) and b) respectively.

the experiments described above we also record the excitation amplitude that was necessary to keep the cantilever oscillation amplitude constant during image acquisition as well as during the frequency versus distance measurements. This excitation amplitude can be converted to energy dissipated per oscillation cycle. The A_{exc} data measured during acquisition of images 6.4a) and c) was converted to energy dissipated per oscillation cycle and is shown in figure 6.7. Note that zero corresponds to the intrinsic dissipation of the free cantilever and negative values of the dissipation are due to experimental noise. Weak atomic scale contrast is observed in the data. Between images 6.4a), 6.7a) (acquired simultaneously) and images 6.4b), 6.7b) tip change 2 has taken place. The atomic scale dissipation contrast has slightly changed due to this tip change. The dissipation versus distance data acquired simultaneously to the frequency versus distance measurement presented in figure 6.6 are shown in figure 6.8 along with the corresponding frequency-distance data. The maximum energy dissipation observed during frequency versus distance measurements is about 100 times larger than the dissipation observed during imaging. At the measuring distance, almost no dissipation is observed both above the minimum and the maximum in agreement with the data acquired during imaging. Above the minimum, no dissipation is measured at all tip-sample distances that were investigated. Above the maximum a significant increase in dissipation is measured at a tip-sample distance of about 0.1 nm (a total tip-sample distance of 0.384 nm taking the bonding length of 0.284 nm for NiO into account).

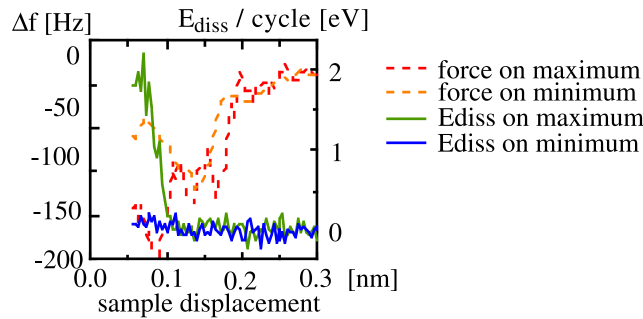

Figure 6.8: Dissipated energy per oscillation cycle versus distance measured simultaneously to the frequency versus distance data shown in figure 6.6.

This is the same distance where the slope of the frequency versus distance data obtained above the maximum becomes steep again after the plateau. This suggests that the movement of ions could become hysteretic at this distance.

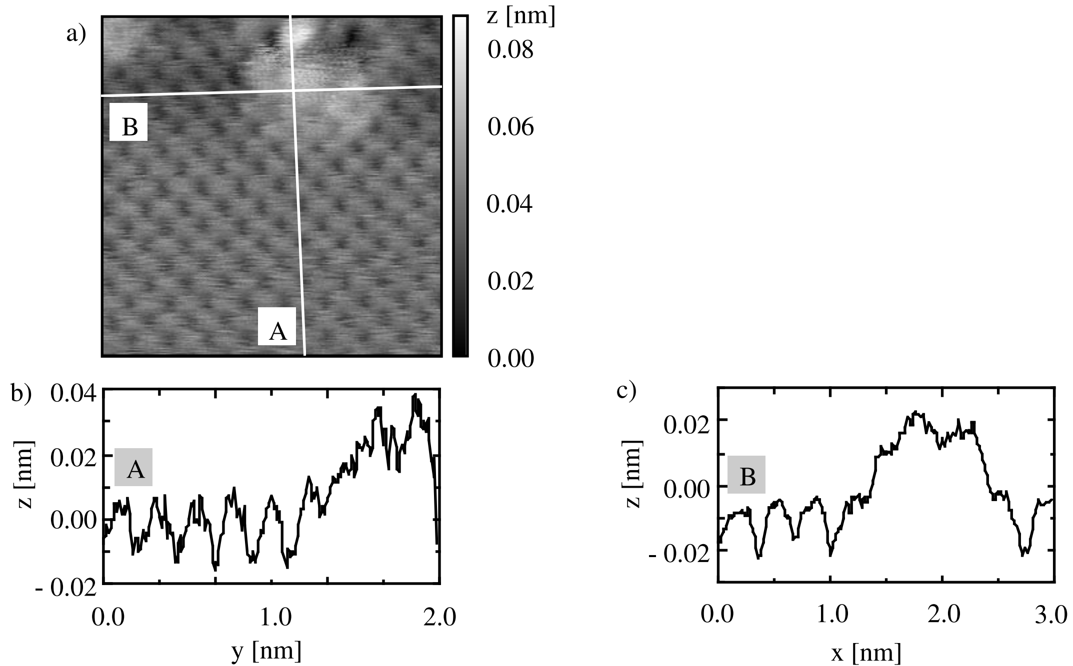

Figure 6.9: Defect observed on the NiO surface.

6.9 An atomic scale defect

An atomic scale defect was observed on the NiO surface (figure 6.9). The area it occupies is much larger than the area occupied by the defect observed on KBr (chapter 5.7). In the x direction it occupies about 5 surface unit cells and in y it occupies about 4 surface unit cells. It is asymmetric and adjacent to the image border and probably continues outside of the image. In both the x and y line profile shown, the atomic periodicity of the NiO surface is preserved even in the defect centre. Probably in this region the surface is modified by charge. Similar features have been observed on the InP surface by SFM [108] and were interpreted as single dopant atoms. The area modified by the dopant atoms is related to the screening length of the semiconductor. Near the top of the image the defect appears in only one unit cell in the x direction. This shows that the tip is atomically sharp in the x direction.

6.10 Conclusions

We have presented the first site-specific force and dissipation versus distance measurements of the interaction between a sharp tip and a NiO surface. It was possible to describe the long range force using a model of the electrostatic interaction with the surface. Large relaxation effects lead to a plateau in the force versus distance data associated with an increase in dissipation

signal. This plateau in the force versus distance data can be explained by the interaction of several tip or surface ions in agreement with previously reported calculations. At the tip-sample distances where multiatom interactions between the tip and sample becomes important, the energy dissipation also increases sharply. This suggests, that the movement of ions could become hysteretic at this distance. It also appears that such multiatom interactions between tip and surface prevent imaging at close tip-sample distances and may explain why imaging of atomic scale contrast due to exchange forces has not been observed experimentally inspite of the efforts of several groups. The observation of a defect on NiO shows that the tip is atomically sharp at the tip-sample distances used for imaging.

Chapter 7

General conclusions

7.1 MFM measurements on Ag/Fe/Ag sandwiches

In the first chapter, a magnetic sample with perpendicular magnetic anisotropy, a Ag/Fe/Ag sandwich was studied that shows a very low coercive field. The anisotropy of this sample depends on the film thickness, and changes from perpendicular for thin films to in-plane for thick films. Qiu et al. [62] had suggested the existence of magnetic domains with perpendicular magnetization near the magnetic reorientation transition of thin Ag/Fe/Ag samples. Room temperature MFM measurements confirmed this hypothesis. The domain size and shape was found to vary as a function of film thickness. The observed domain size decreases strongly with increasing film thickness in agreement with the model provided by Kaplan and Gehring [65]. The analysis of the domain size as a function of film thickness is consistent with a value of the surface anisotropy similar to that measured by Schaller et al. [68] and Heinrich et al. [76]. The domain shape variation as a function of film thickness predicted by Abanov et al. [66], from stripe domains on thin films to isotropic domains on thick films, was also confirmed by our measurements. In order to test the applicability of the Mermin-Wagner theorem on ultrathin films of Ag/Fe/Ag, it is not sufficient to confirm a reduced remanent magnetization near the reorientation transition, but it should also be shown that this reduced remanent magnetization is not simply due to the presence of magnetic domains.

7.2 Quantitative Magnetic Force Microscopy

It is important to produce magnetic tips that generate a small magnetic field of the desired magnitude in a reliable way in order to image samples like the Ag/Fe/Ag sandwich. Therefore, tips covered with very thin Fe layers and tips covered with Ni, a material with a smaller saturation magnetization than Fe, have been studied in the second chapter using quantitative magnetic force microscopy.
The field emitted by Fe coated tips scales roughly proportional to the film thickness. The tips show good imaging properties down to a film thickness of about 1.6 nm. With a film thickness of about 1.6 nm the generated field is about 0.8 mT.
Ni coated tips are not suitable for magnetic imaging, as the images show distortions that reflect either a canting of the magnetization vector relative to the tip axis or modification of the tip magnetization by the sample stray field. Other materials that could be tested as tip coating

materials are Cobalt and magnetic alloys such as FePd ($M_S = 1100$ kA/m) having a significantly lower saturation magnetization than Fe.
The question whether the MFM resolution can be increased by using ultrasharp tips was addressed. These tips have opening angles of only 10° and high aspect ratios. Although the ultrasharp tip tested was damaged either due to the heat deposited at the tip apex during evaporation of the magnetic coating or by touching the sample during imaging, it still has a smaller critical wavelength and therefore a higher resolution than Nanosensor tips. The imaging properties of ultrasharp tips can be described by a monopole model in a better way than conventional Nanosensors proving that ultrasharp tips are sharper than Nanosensor tips.
Although the resolution of MFM can be improved by using sharper tips, in order to achieve atomic scale resolution, the regime of short-range forces has to be considered. These short-range forces were studied in chapter 5.

7.3 Atomic resolution measurements on KBr

KBr is a non-magnetic ionic crystal and a suitable sample for studying short-range forces. In this chapter, the first site-specific force versus distance measurements of the weak interaction force between a sharp tip and an insulator were presented. It was possible to describe the very weak long-range force using a model of the van-der-Waals interaction with the surface. The atomic details of the tip were found to play a strong role in the corrugation obtained in atomic resolution images. Switches in contrast are related to changes of the atomic structure of the tip apex. This could be studied further by preparing atomically controlled tips for example by depositing metal on the tips or by simulating the interaction forces for different tip structures.
The interaction between a KBr covered tip and a KBr sample has been studied from a theoretical point of view using atomistic simulation techniques. Unlike the Si surface, where covalent attractive chemical bonding forces dominate in the atomic resolution range [35], on the ionic crystal KBr, short-range repulsive forces arise when the ion at the tip apex faces an ion of the same type on the sample. Assuming that the mesoscopic radius of the tip remains constant, reducing the long-range van-der-Waals force by increasing the height of the protruding nanotip does not necessarily increase the obtained corrugation. There is an optimum tip height corresponding to the largest corrugation. If the nanotip protrudes more, imaging is possible only with a very small negative frequency shift.
The frequency shift versus distance data showed qualitative agreement with the experimental data, although the corrugation calculated at the experimental frequency shift setpoint was much larger. The chemical nature of the tip apex ion or the arrangement of the atoms located at the tip apex could be different in the experiment from the model used in the simulation.
It is possible to distinguish between a positively and a negatively terminated tip, if a force versus distance measurement above the bridge site located between two neighbouring Br^--ions and two neighbouring K^+-ions is performed. Thus, a way of distinguishing between different tips exists, even though if all cation and anion sites are equivalent.
From the analysis of the observed monoatomic defect, it can be concluded that the tip used in this experiment is atomically sharp and that true atomic resolution is achieved. The contribution of the tip apex ion to the image contrast is much stronger than the contribution of other ions. The contribution of other ions is negligible compared to the experimental noise. This result was obtained by subtracting an average image, where the average over many defect-free unit cells was calculated. The defect is uncharged, but its nature cannot be identified.

7.4 Atomic resolution measurements on NiO

We have presented the first site-specific force and dissipation versus distance measurements of the interaction between a sharp tip and a NiO surface. It was possible to describe the long range force using a model of the electrostatic interaction with the surface. Large relaxation effects lead to a plateau in the force versus distance data associated with an increase in dissipation signal. This plateau in the force versus distance data can be explained by the interaction of several tip or surface ions in agreement with previously reported calculations. At the tip-sample distances where multiatom interactions between the tip and sample becomes important, the energy dissipation also increases sharply. This suggests, that the movement of ions could become hysteretic at this distance. It also appears that such multiatom interactions between tip and surface prevent imaging at close tip-sample distances and may explain why imaging of atomic scale contrast due to exchange forces has not been observed experimentally inspite of the efforts of several groups. The observation of a defect on NiO shows that the tip is atomically sharp at the tip-sample distances used for imaging.

Appendix A

Magnetic contrast formation

In this appendix, some helpful calculations related to transfer function theory that were omitted in chapter 2.7 are given (see [40, 16] and references therein). The theoretical considerations discussed in chapter 2.7.4 are unpublished [129]. Also the exponential decay of the force as a function of z used in chapter 2.7.5 is proven.

A.1 Definition of the scalar magnetic potential and related quantities

First some definitions are given to facilitate the discussion of magnetic fields. The region above the sample is current free and contains no time-varying electric fields:

$$\nabla \times \vec{H}(\vec{x}) = 0 \tag{A.1}$$

To facilitate the description, a scalar magnetic potential can be defined in analogy to the electric scalar potential, as well as the volume and surface magnetic charge functions:

$$\begin{aligned} -\nabla\Phi(\vec{x}) &:= \vec{H}(\vec{x}) \qquad \rho_M(\vec{x}) := -\nabla\vec{M}(\vec{x}) \\ \sigma_M(\vec{x}) &:= \left(\vec{M}_{\text{inside}}(\vec{x}) - \vec{M}_{\text{outside}}(\vec{x})\right) \cdot \vec{n} \end{aligned} \tag{A.2}$$

With these definitions, similar to electric charge distributions, the Laplace equation is valid:

$$\triangle\Phi = \rho_M(\vec{x}) \tag{A.3}$$

with the boundary condition at the surface:

$$\left.\frac{\partial\Phi}{\partial z}\right|_{\text{inside}} - \left.\frac{\partial\Phi}{\partial z}\right|_{\text{outside}} = \sigma_M \tag{A.4}$$

A.2 The stray field of a magnetic sample

The description of the interaction between the magnetic tip and sample is simplest in Fourier space. Here we use a two-dimensional Fourier transform. It is defined as:

$$
\begin{aligned}
\vec{f}(\vec{k}_{||}, z) &= \int_{-\infty}^{\infty} \vec{f}(\vec{x}) \cdot e^{-i\vec{k}_{\|}\vec{x}_{\|}}\, dx\, dy \\
\vec{f}(\vec{x}) &= \frac{1}{4\pi^2} \int_{-\infty}^{\infty} \vec{f}(\vec{k}_{||}, z) \cdot e^{i\vec{k}_{\|}\vec{x}_{\|}}\, dk_x\, dk_y \qquad \text{(A.5)} \\
\text{where} \quad \vec{k}_{||} &= (k_x, k_y) \quad \text{and} \quad \vec{x}_{||} = (x, y)
\end{aligned}
$$

The derivative in two-dimensional Fourier space in the x and y direction becomes $\partial/\partial x = ik_x \quad \partial/\partial y = ik_y$. The Laplace equation for two-dimensional Fourier space in the region above the sample

$$
-k_x^2 \Phi(\vec{k}_{||}, z) - k_y^2 \Phi(\vec{k}_{||}, z) + \frac{\partial^2 \Phi(\vec{k}_{||}, z)}{\partial z^2} = 0 \qquad \text{(A.6)}
$$

combined with the boundary condition $\Phi(\vec{k}_{||}, z) \to \infty \quad (z \to \infty)$ yields

$$
\Phi(\vec{k}_{||}, z) = \Phi(\vec{k}_{||}, 0) \cdot e^{-k_{\|} z} \quad \text{where} \quad k_{||} = \sqrt{k_x^2 + k_y^2} \qquad \text{(A.7)}
$$

A similar equation is valid for the components of the magnetic stray field:

$$
\vec{H}_{\text{sample}}(\vec{k}_{||}, z) = -\nabla \Phi(\vec{k}_{||}, z) = -\begin{pmatrix} ik_x \\ ik_y \\ -k_{||} \end{pmatrix} \Phi(\vec{k}_{||}, 0) \cdot e^{-k_{\|} z} \qquad \text{(A.8)}
$$

The full solution of the Laplace equation for the case of $\vec{M}(\vec{x}) = \vec{M}(\vec{x}_{||})$ has been derived in literature [40, 59, 60]:

$$
\vec{H}_{\text{sample}}(\vec{k}_{||}, z) = -\frac{\nabla}{k_{||}} \frac{\left(1 - e^{-k_{\|} d}\right) \quad e^{-k_{\|} z}}{2} \frac{1}{k_{||}} \begin{pmatrix} -ik_x \\ -ik_y \\ k_{||} \end{pmatrix} \cdot \vec{M}(\vec{k}_{||}) \qquad \text{(A.9)}
$$

A.3 The tip equivalent charge distribution

The magnetic force in direct space is given by:

$$
\begin{aligned}
\vec{F}(\vec{x}) &= -\mu_0 \int_{-\infty}^{\infty} \vec{H}_{\text{sample}}(\vec{x'}) \cdot \nabla' \vec{M}_{\text{tip}}(\vec{x'} - \vec{x})\, d^3\vec{x'} \qquad \text{(A.10)} \\
\text{where} \quad \vec{x'} &= (x', y', z') \quad \text{and} \quad \nabla' = \left(\frac{\partial}{\partial x'}, \frac{\partial}{\partial y'}, \frac{\partial}{\partial z'}\right)
\end{aligned}
$$

After deriving these properties of the sample stray field, the force can now also be evaluated in Fourier space.

$$\vec{F}(\vec{k}_{||}, z) = -\mu_0 \int_{-\infty}^{\infty} \vec{H}_{\text{sample}}(\vec{k}_{||}, z') \cdot \nabla_{\vec{k}_{||}, z'} \vec{M}^*_{\text{tip}}(\vec{k}_{||}, z' - z) dz \tag{A.11}$$

After a coordinate transformation where $z' \to z' + z$ and using equation A.8:

$$\begin{aligned} \vec{F}(\vec{k}_{||}, z) &= -\mu_0 \vec{H}_{\text{sample}}(\vec{k}_{||}, z) \cdot \int_{-\infty}^{\infty} e^{-k_{\|} z'} \nabla_{\vec{k}_{||}, z'} \vec{M}^*_{\text{tip}}(\vec{k}_{||}, z') dz' \\ &=: \mu_0 \vec{H}_{\text{sample}}(\vec{k}_{||}, z) \sigma^*_{\text{tip}}(\vec{k}_{||}) \end{aligned} \tag{A.12}$$

σ_{tip} is a surface charge distribution located in the plane touching the tip apex [16].
If there is no modification, $\sigma_{\text{tip}}(\vec{k}_{||})$ does not depend on z and an equation similar to equations A.7 and A.8 is valid for the force:

$$\vec{F}(\vec{k}_{||}, z) = -\mu_0 \sigma^*_{\text{tip}}(\vec{k}_{||}) \vec{H}_{\text{sample}}(\vec{k}_{||}, 0) \cdot e^{-k_{\|} z} = \vec{F}(\vec{k}_{||}, 0) \cdot e^{-k_{\|} z} \tag{A.13}$$

A.4 Conversion of frequency shift to force

Now we have calculated the force acting on the tip. As all MFM measurements shown here are done in dynamic mode, we have to evaluate the conversion to frequency shift. The frequency shift is given by [27]:

$$\Delta f(\vec{x}_0) = -\frac{f_0}{\pi c_L A} \int_0^{\pi} \vec{n} \vec{F}(\vec{x}(\varphi)) \cos\varphi d\varphi \quad \text{where} \quad \vec{x} = \vec{x}_0 + \vec{n} \cdot A \cos\varphi \tag{A.14}$$

Here $\vec{n}$ is the direction of the oscillation of the cantilever. To calculate the frequency shift, we use equation A.13 in real space:

$$\Delta f(\vec{x}_0) = \frac{f_0 \mu_0}{4\pi^3 c_L A} \int_0^{\pi} \vec{n} \int_{-\infty}^{\infty} \sigma^*_{\text{tip}}(\vec{k}_{||}) \vec{H}_{\text{sample}}(\vec{k}_{||}, 0) \cdot e^{-k_{\|} z} \cdot e^{i \vec{k}_{\|} \vec{x}_{\|}} \, dk_x \, dk_y \cos\varphi d\varphi \tag{A.15}$$

Taking into account that $\vec{x} = \vec{x}_0 + \vec{n} \cdot A \cos\varphi$, changing the order of integration and changing to Fourier space this equation can be transformed into the following form [129]:

$$\begin{aligned} \Delta f(\vec{k}_{||}, z_0) &= \frac{f_0 \mu_0}{2 c_L} \cdot \frac{2}{\pi A} \int_0^{\pi} \sigma^*_{\text{tip}}(\vec{k}_{||}) \vec{n} \vec{H}_{\text{sample}}(\vec{k}_{||}, 0) \cdot e^{-k_{\|} z} \cdot e^{i \vec{k}_{\|} \vec{n}_{\|} A \cos\varphi} \cos\varphi d\varphi \\ &= \frac{f_0 \mu_0}{2 c_L} \cdot \sigma^*_{\text{tip}}(\vec{k}_{||}) \vec{n} \vec{H}_{\text{sample}}(\vec{k}_{||}, 0) \cdot e^{-k_{\|} z_0} \cdot \frac{2}{A} I_1(iA(\vec{k}_{||} \vec{n}_{||} - k_{||} n_z)) \\ &= \frac{f_0 \mu_0}{2 c_L} \cdot \vec{n} \vec{F}(\vec{k}_{||}, z_0) \cdot \frac{2}{A} I_1(iA(\vec{k}_{||} \vec{n}_{||} - k_{||} n_z)) \\ \text{where} \quad I_1(z) &= \frac{1}{\pi} \int_0^{\pi} e^{-z \cos\varphi} \cos\varphi d\varphi \qquad z \in \mathbb{C} \end{aligned} \tag{A.16}$$

is the first order modified Bessel function of the first kind.

Bibliography

[1] M. Hehn, S. Padovani, K. Ounadjela and J. P. Bucher, *Nanoscale magnetic domain structures in epitaxial cobalt films*, Phys. Rev. B **54**, p. 3428–3433 (1996).

[2] V. Gehanno, A. Marty, B. Gilles and Y. Samson, *Magnetic domains in epitaxial ordered FePd(001) thin films with perpendicular magnetic anisotropy*, Phys. Rev. B **55**, p. 12552–12555 (1997).

[3] H. J. Hug, G. Bochi *et al.*, *Magnetic domain structure in ultrathin Cu/Ni/Cu/Si(001)-films*, J. Appl. Phys. **79**, p. 5609–5614 (1996).

[4] A. J. Cox, J. G. Louderback and L. A. Bloomfield, *Experimental observation of magnetism in Rhodium clusters*, Phys. Rev. Lett. **71**, p. 923–926 (1993).

[5] P. Gambardella, S. Rusponi *et al.*, *Magnetic moments and anisotropy of Co adatoms and clusters on Pt(111).*

[6] F. Bitter, *On inhomogeneities in the magnetization of ferromagnetic materials*, Phys. Rev. **38**, p. 1903–1905 (1931).

[7] R. Allenspach, M. Stampanoni and A. Bischof, *Magnetic domains in thin epitaxial Co/Au(111) films*, Phys. Rev. Lett. **65**, p. 3344–3347 (1990).

[8] R. Allenspach and A. Bischof, *Magnetization direction switching in Fe/Cu(100) epitaxial films: Temperature and thickness dependence*, Phys. Rev. Lett. **69**, p. 3385–3388 (1992).

[9] J. Baruchel, M. Schlenker, K. Kurosawa and S. Saito, *Antiferromagnetic S-domains in NiO I: Neutron magnetic topographic investigation*, J. Phys. C: Solid State Phys. **43**, p. 853–860 (1981).

[10] G. Binnig, H. Rohrer, C. Gerber and E. Weibel, *Surface studies by scanning tunneling microscopy*, Phys. Rev. Lett. **49**, p. 57–60 (1982).

[11] G. Binnig, C. F. Quate and C. Gerber, *Atomic force microscopy*, Phys. Rev. Lett. **56**, p. 930–933 (1986).

[12] F. Giessibl, *Atomic resolution of silicon (111) 7×7 by atomic force microscopy through repulsive and attractive forces*, Science **267**, p. 1451–1455 (1995).

[13] M. Bammerlin, R. Lüthi *et al.*, *True atomic resolution on the surface of an insulator via ultrahigh vacuum dynamic force microscopy*, Probe Microscopy **1**, p. 3–9 (1997).

[14] Y. Martin and H. K. Wickramasinghe, *Magnetic imaging by "force microscopy" with 1000 Å resolution*, Appl. Phys. Lett. **50**, p. 1455–1457 (1987).

[15] J. J. Saenz, N. Garcia *et al.*, *Observation of magnetic forces by the atomic force microscope*, J. Appl. Phys. **62**, p. 4293–4295 (1987).

[16] P. J. A. van Schendel, H. J. Hug *et al.*, *A method for the calibration of magnetic force microscopy tips*, J. Appl. Phys. **88**, p. 435–445 (2000).

[17] M. Kleiber, M. Bode, R. Ravlič and R. Wiesendanger, *Topology-induced spin frustrations at the Cr(001) surface studied by spin-polarized scanning tunneling spectroscopy*, Phys. Rev. Lett. **85**, p. 4606–4609 (2000).

[18] S. Heinze, M. Bode *et al.*, *Real-space imaging of two-dimensional antiferromagnetism on the atomic scale*, Science **288**, p. 1805–1808 (2000).

[19] H. Ness and F. Gautier, *Theoretical study of the interaction between a magnetic nanotip and a magnetic surface*, Phys. Rev. B **52**, p. 7352–7362 (1995).

[20] K. Nakamura, H. Hasegawa *et al.*, *First-principles calculation of the exchange interaction and the exchange force between magnetic Fe films*, Phys. Rev. B **56**, p. 3218–3221 (1997).

[21] H. Hosoi, M. Kimura *et al.*, *Non-contact atomic force microscopy of an antiferromagnetic NiO(100) surface using a ferromagnetic tip*, Appl. Phys. A **72**, p. S23–S26 (2001).

[22] W. Allers, S. Langkat and R. Wiesendanger, *Dynamic low-temperature scanning force microscopy on nickel oxide (001)*, Appl. Phys. A **72**, p. S27–S30 (2001).

[23] B. Stiefel, *Magnetic force microscopy at low temperatures and in ultra high vacuum - application on high temperature superconductors.* Ph.D. thesis, Universität Basel, 1998.

[24] H. J. Hug, B. Stiefel *et al.*, *A low temperature UHV scanning force microscope*, Rev. Sci. Instrum. **70**, p. 3625–3640 (1999).

[25] U. Rabe, K. Janser and W. Arnold, *Vibrations of free and surface-coupled atomic force microscope cantilevers: Theory and experiment*, Rev. Sci. Instrum. **67**, p. 3281–3293 (1996).

[26] E. Meyer and H. Heinzelmann, in **Scanning Tunneling Microscopy II**, Vol. 28 de **Springer Series in Surface Science**, edited by R. Wiesendanger and H.–J. Güntherodt (Springer-Verlag, Heidelberg, 1992).

[27] F. J. Giessibl, *Forces and frequency shifts in atomic-resolution dynamic-force microscopy*, Phys. Rev. B **56**, p. 16010–16015 (1997).

[28] U. Dürig, *Extracting interaction forces and complementary observables in dynamic probe microscopy*, Appl. Phys. Lett. **76**, p. 1203–1205 (2000).

[29] F. J. Giessibl, *A direct method to calculate tip-sample forces from frequency shifts in frequency-modulation atomic force microscopy*, Appl. Phys. Lett. **78**, p. 123–125 (2001).

[30] T. R. ALBRECHT, P. GRÜTTER, D. HORNE and D. RUGAR, *Frequency modulation detection using high-Q cantilevers for enhanced force microscope sensitivity*, J. Appl. Phys. **69**, p. 668–673 (1991).

[31] T. FLIESSBACH, **Mechanik** (B.I. Wissenschaftsverlag, MANNHEIM, 1991).

[32] C. LOPPACHER, *Nichtkontakt-Rasterkraftmikroskopie mit digitalem Phasenregelkreis.* Ph.D. thesis, Universität Basel, 2000.

[33] C. LOPPACHER, M. BAMMERLIN *et al.*, *Fast digital electronics for application in dynamic force microscopy using high-Q cantilevers*, Appl. Phys. A **66**, p. S215–S218 (1998).

[34] J. ISRAELACHVILI, **Intermolecular and Surface Forces** (Academic Press, LONDON, 1991).

[35] M. A. LANTZ, H. J. HUG *et al.*, *Quantitative measurement of short-range chemical bonding forces*, Science **291**, p. 2580–2583 (2001).

[36] M. GUGGISBERG, M. BAMMERLIN *et al.*, *Separation of interactions by noncontact force microscopy*, Phys. Rev. B **61**, p. 11151–11155 (2000).

[37] C. ARGENTO and R. H. FRENCH, *Parametric tip model and force-distance relation for Hamaker constant determination from atomic force microscopy*, J. Appl. Phys. **80**, p. 6081–6090 (1996).

[38] S. HUDLET, M. SAINT JEAN, C. GUTHMANN and J. BERGER, *Evaluation of the capacitive force between an atomic force microscopy tip and a metallic surface*, Eur. Phys. J. B **2**, p. 5–10 (1998).

[39] R. BENNEWITZ, *Kraftmikroskopie an CaF_2(111): Charakterisierung der reinen und der elektronenstrahlmodifizierten Oberfläche.* Ph.D. thesis, FU Berlin, 1997.

[40] P. J. A. van SCHENDEL, *Investigation of magnetization structures in ferromagnetic and superconducting samples by magnetic force microscopy.* Ph.D. thesis, Universität Basel, 1999.

[41] R. ERLANDSSON and L. OLSSON, *Force interaction in low-amplitude ac-mode atomic force microscopy: cantilever simulations and comparison with data from Si(111) 7×7*, Appl. Phys. A **66**, p. S879–S883 (1998).

[42] J. P. AIMÉ, R. BOISGARD, L. NONY and G. COUTURIER, *Nonlinear dynamic behaviour of an oscillating tip-microlever system and contrast at the atomic scale*, Phys. Rev. Lett. **82**, p. 3388–3391 (1999).

[43] M. GAUTHIER and M. TSUKADA, *Damping mechanism in dynamic force microscopy*, Phys. Rev. Lett. **85**, p. 5348–5351 (2000).

[44] C. LOPPACHER, R. BENNEWITZ *et al.*, *Experimental aspects of dissipation force microscopy*, Phys. Rev. B **62**, p. 13674–13679 (2000).

[45] W. DENK and D. W. POHL, *Local electrical dissipation imaged by scanning force microscopy*, Appl. Phys. Lett. **59**, p. 2171–2173 (1991).

[46] T. D. Stowe, T. W. Kenny, D. J. Thomson and D. Rugar, *Silicon dopant imaging by dissipation force microscopy*, Appl. Phys. Lett. **75**, p. 2785–2787 (1999).

[47] M. Gauthier and M. Tsukada, *Theory of noncontact dissipation force microscopy*, Phys. Rev. B **60**, p. 11 716–11 722 (1999).

[48] L. N. Kantorovich, *A simple non-equilibrium theory of non-contact dissipation force microscopy*, J. Phys.: Condens. Matter **13**, p. 945–958 (2001).

[49] L. N. Kantorovich, *Stochastic friction force mechanism of energy dissipation in non-contact atomic force microscopy*, Phys. Rev. B **64**, p. 245409/1–13 (2001).

[50] N. Sasaki and M. Tsukada, *Effect of microscopic nonconservative process on noncontact atomic force microscopy*, Jap. J. of Appl. Phys. **39**, p. L1334–L1337 (2000).

[51] Y. Liu, B. Ellman and P. Grütter, *Theory of magnetic dissipation imaging*, Appl. Phys. Lett. **71**, p. 1418–1420 (1997).

[52] Y. Liu, P. LeBlanc, P. Grütter and U. Dürig, *Magnetic dissipation imaging*, Appl. Phys. Lett. **81**, p. 5024 (1997).

[53] I. Schmid, *Potentiale und Grenzen der Magnetkraftmikroskopie bei Raumtemperatur*. Master's thesis, Universität Basel, 2001.

[54] A. Hubert and R. Schäfer, **Magnetic Domains. The Analysis of Magnetic Domain Structures** (Springer-Verlag, Berlin, Heidelberg, 1998).

[55] C. D. Wright and E. W. Hill, *Reciprocity in magnetic force microscopy*, Appl. Phys. Lett. **67**, p. 433–435 (1995).

[56] S. Porthun, L. Abelmann *et al.*, *Optimization of lateral resolution in magnetic force microscopy*, Appl. Phys. A **66**, p. S1185–S1189 (1998).

[57] H. J. Hug, B. Stiefel *et al.*, *Quantitative magnetic force microscopy on perpendicularly magnetized samples*, J. Appl. Phys. **83**, p. 5609–5620 (1998).

[58] C. D. Wright and E. W. Hill, *Reciprocity based transfer function analysis in magnetic force microscopy*, Appl. Phys. Lett. **68**, p. 1726–1728 (1996).

[59] C. Schönenberger and S. F. Alvarado, *Understanding magnetic force microscopy*, Z. Phys. B: Condens. Matter **80**, p. 373–383 (1990).

[60] M. Mansuripur, *Demagnetizing field computation for dynamic simulation of the magnetization reversal process*, IEEE Trans. Magn. **128**, p. 111–112 (1988).

[61] N. D. Mermin and H. Wagner, *Absence of ferromagnetism or antiferromagnetism in one- or two-dimensional isotropic Heisenberg models*, Phys. Rev. Lett. **17**, p. 1133–1136 (1966).

[62] Z. Q. Qiu, J. Pearson and S. D. Bader, *Asymmetry of the spin reorientation transition in ultrathin Fe films and wedges grown on Ag(100)*, Phys. Rev. Lett. **70**, p. 1006–1009 (1993).

[63] A. Vaterlaus, C. Stamm *et al.*, *Two-step disordering of perpendicularly magnetized ultrathin films*, Phys. Rev. Lett. **84**, p. 2247–2250 (2000).

[64] R. P. Cowburn, S. J. Gray *et al.*, *Magnetic switching and in-plane uniaxial anisotropy in ultrathin Ag/Fe/Ag(100) epitaxial films*, J. Appl. Phys. **78**, p. 7210–7219 (1995).

[65] B. Kaplan and G. Gehring, *The domain structure in ultrathin magnetic films*, J. of Magn. Magn. Mater. **128**, p. 111 (1993).

[66] A. Abanov, V. Kalatsky, V. L. Pokrovsky and W. M. Saslow, *Phase diagram of ultrathin ferromagnetic films with perpendicular anisotropy*, Phys. Rev. B **51**, p. 1023–1038 (1995).

[67] A. Berger and H. Hopster, *Nonequilibrium magnetization near the reorientation phase transition of Fe/Ag(100) films*, Phys. Rev. Lett. **76**, p. 519–522 (1996).

[68] D. M. Schaller, D. E. Bürgler *et al.*, *Spin reorientations induced by morphology changes in Fe/Ag(001)*, Phys. Rev. B **59**, p. 14 516–14 519 (1999).

[69] J. Araya-Pochet, C. A. Ballentine and J. L. Erskine, *Thickness- and temperature-dependent spin anisotropy of ultrathin epitaxial Fe films on Ag(100)*, Phys. Rev. B **38**, p. 7846–7849 (1988).

[70] M. Stampanoni, A. Vaterlaus, M. Aeschlimann and F. Meier, *Magnetism of epitaxial bcc iron on Ag(001) observed by spin-polarized photoemission*, Phys. Rev. Lett. **59**, p. 2483–2485 (1987).

[71] D. E. Bürgler, C. M. Schmidt *et al.*, *Optimized epitaxial growth of Fe on Ag(001)*, Phys. Rev. B **56**, p. 4149–4158 (1997).

[72] M. Rührig, S. Porthun and J. C. Lodder, *Magnetic force microscopy using electron-beam fabricated tips*, Rev. Sci. Instrum. **65**, p. 3225–3228 (1994).

[73] L. Abelmann, S. Porthun *et al.*, *Comparing the resolution of magnetic force microscopes using the CAMST reference sample*, J. of Magn. Magn. Mater. **190**, p. 135–147 (1998).

[74] S. Chikazumi, **Physics of Magnetism** (John Wiley & Sons Inc., New York, London, Sydney, 1964).

[75] H. H. Landolt, R. Börnstein and A. Eucken, **Zahlenwerte und Funktionen aus Physik, Chemie, Astronomie, Geophysik und Technik** (Springer-Verlag, Berlin, London, New York, 1961).

[76] B. Heinrich, K. B. Urquhart *et al.*, *Large surface anisotropies in ultrathin films of bcc and fcc Fe(001)*, J. Appl. Phys. **63**, p. 3863–3868 (1988).

[77] P. Bruno, *Dipolar magnetic surface anisotropy in ferromagnetic thin films with interfacial roughness*, J. Appl. Phys. **64**, p. 3153–3156 (1988).

[78] G. Matteucci, M. Muccini and U. Hartmann, *Flux measurements on ferromagnetic microprobes by electron holography*, Phys. Rev. B **50**, p. 6823–6828 (1994).

[79] D. G. Streblechenko, M. R. Scheinfein, M. Mankos and K. Babcock, *Quantitative magnetometry using electron holography: Field profiles near magnetic force microscope tips*, IEEE Trans. Magn. **32**, p. 4124–4129 (1996).

[80] R. P. Ferrier, S. McVitie, A. Gallagher and W. A. P. Nicholson, *Characterisation of MFM tip fields by electron tomography*, IEEE Trans. Magn. **33**, p. 4062–4064 (1997).

[81] A. Wadas and H. J. Hug, *Models for the stray field from magnetic tips used in magnetic force microscopy*, J. Appl. Phys. **72**, p. 203–206 (1992).

[82] R. Madabhushi, R. D. Gomez, E. R. Burke and I. D. Mayergoyz, *Magnetic biasing and MFM image reconstruction*, IEEE Trans. Magn. **32**, p. 4147–4149 (1996).

[83] L. Belliard, A. Thiaville *et al.*, *Investigation of the domain contrast in magnetic force microscopy*, J. Appl. Phys. **81**, p. 3849–3851 (1997).

[84] H. Saito, J. Chen and S. Ishio, *Description of magnetic force microscopy by three-dimensional tip Green's function for sample magnetic charges*, J. of Magn. Magn. Mater. **191**, p. 153–161 (1999).

[85] S. McVitie, R. P. Ferrier *et al.*, *Quantitative field measurements from magnetic force microscope tips and comparison with point and extended charge models*, J. Appl. Phys. **89**, p. 3656–3661 (2001).

[86] **American Institute of Physics Handbook**, 3rd edition, edited by D. E. Gray (McGraw-Hill Book Company, New York, 1972).

[87] G. Bochi, C. Ballentine *et al.*, *Perpendicular magnetic anisotropy, domains and misfit strain in epitaxial $Ni/Cu_{1-x}Ni_x/Si$ (001) thin films*, Phys. Rev. B **52**, p. 7311–7321 (1995).

[88] G. Bochi, H. J. Hug *et al.*, *Magnetic domain structure in ultrathin films*, Phys. Rev. Lett. **75**, p. 1839–1842 (1995).

[89] V. Barwich, *Magnetische Anisotropien von Cu/Ni/Cu-Schichtsystemen.* Master's thesis, Universität Basel, 2001.

[90] B. Zhang and W. A. Soffa, *The structure and properties of $L1_0$ ordered ferromagnets : Co-Pt, Fe-Pt, Fe-Pd, and Mn-Al*, Scripta Met. Mater. **30**, p. 683 (1994).

[91] S. Fölsch, A. Helms *et al.*, *Self-organized patterning of an insulator-on-metal system by surface faceting and selective growth: NaCl/Cu(211)*, Phys. Rev. Lett. **84**, p. 123–126 (2000).

[92] R. Bennewitz, S. Schär *et al.*, *Atomic-resolution images of radiation damage in KBr*, Surf. Sci. Lett. **474**, p. L197–L202 (2001).

[93] R. Bennewitz, A. S. Foster *et al.*, *Atomically resolved edges and kinks of NaCl islands on Cu(111): Experiment and theory*, Phys. Rev. B **62**, p. 2074–2084 (2000).

[94] M. Reichling and C. Barth, *Scanning force imaging of atomic size defects on the $CaF_2(111)$ surface*, Phys. Rev. Lett. **83**, p. 768–771 (1999).

[95] L. N. Kantorovich, A. S. Foster, A. L. Shluger and A. M. Stoneham, *Role of image forces in non-contact scanning force microscope images of ionic surfaces*, Surf. Sci. **445**, p. 283–299 (2000).

[96] J. Wollbrandt, E. Linke and U. Brückner, *Untersuchung elektrostatischer Aufladungen auf Spaltflächen von Alkalihalogenideinkristallen*, Experimentelle Technik der Physik **XXIII**, p. 65–73 (1975).

[97] M. J. L. Sangster and R. M. Atwood, *Interionic potentials for alkali halides: II completely crystal independent specification of Born-Mayer potentials*, J. Phys. C: Solid State Phys. **11**, p. 1541–1555 (1978).

[98] M. Bammerlin, R. Lüthi *et al.*, *Dynamic SFM with true atomic resolution on alkali halide surfaces*, Appl. Phys. A **66**, p. S293–S294 (1998).

[99] R. H. French, R. M. Cannon, L. K. DeNoyer and Y.-M. Chiang, *Full spectral calculation of non-retarded Hamaker constants for ceramic systems from interband transition strengths*, Solid State Ionics **75**, p. 13–33 (1995).

[100] L. N. Kantorovich and A. Foster, *Scifi v1.0 manual 1.3.2000.*

[101] A. S. Foster, C. Barth, A. L. Schluger and M. Reichling, *Unambiguous interpretation of atomically resolved force microscopy images of an insulator*, Phys. Rev. Lett. **86**, p. 2373–2376 (2001).

[102] L. N. Kantorovich, A. L. Shluger and A. M. Stoneham, *Recognition of surface species in atomic force microscopy: Optical properties of a Cr^{3+} defect at the MgO(001) surface*, Phys. Rev. B **63**, p. 184111 (2001).

[103] D. Brodbeck, D. Bürgler, R. Hofer and G. Tarrach, *Sxm shell reference manual october 1999.*

[104] H. Pick, *Struktur von Störstellen in Alkalihalogenidkristallen*, Springer Tracts of Modern Physics **38**, p. 1–83 (1965).

[105] V. Zialasek, T. Hildebrandt and M. Henzler, *Surface color centers on epitaxial NaCl films*, Phys. Rev. B **62**, p. 2912–2919 (2000).

[106] B. Such, J. Kolodziej *et al.*, *Surface topography dependent desorption of alkali halides*, Phys. Rev. Lett. **85**, p. 2621–2624 (2000).

[107] L. N. Kantorovich, A. L. Shluger and A. M. Stoneham, *Structure and spectroscopy of surface defects from scanning force microscopy: Theoretical predictions*, Phys. Rev. Lett. **85**, p. 3846–3849 (2000).

[108] A. Schwarz, W. Allers, U. D. Schwarz and R. Wiesendanger, *Detection of doping atom distibutions and individual dopants in InAs(110) by dynamic-mode scanning force microscopy in ultrahigh vacuum*, Phys. Rev. B **62**, p. 13617–13622 (2000).

[109] K. Miura, T. Yamada, M. Ishikawa and S. Okita, *Apparent contrast of molecularly thin films of water at ionic crystal surfaces*, Appl. Surf. Sci. **140**, p. 415–421 (1999).

[110] P. Tepper, J. C. Zink *et al.*, *Polarized adsorption of* H_2O *on NaCl(100) in air, observed by second harmonic generation*, J. Vac. Sci. and Technol. B **7**, p. 1212–1215 (1989).

[111] L. W. Bruch, A. Glebov, J. P. Toennies and H. Weiss, *A helium atom scattering study of water adsorption on the NaCl(100) single crystal surface*, J. Chem. Phys. **103**, p. 5109–5120 (1995).

[112] B. Wassermann, S. Mirbt *et al.*, *Clustered water adsorption on the NaCl(100) surface*, J. Chem. Phys. **98**, p. 10049–10060 (1993).

[113] W. L. Roth, *Magnetic structures of MnO, FeO, CoO, and NiO*, Phys. Rev. **110**, p. 1333–1341 (1958).

[114] H. Hosoi, K. Sueoka, K. Hayakawa and K. Mukasa, *Atomic resolved imaging of cleaved NiO(100) surfaces by NC-AFM*, Appl. Surf. Sci. **157**, p. 218–221 (2000).

[115] M. R. Castell, P. L. Wincott *et al.*, *Atomic-resolution STM of a system with strongly correlated electrons: NiO surface structure and defect sites*, Phys. Rev. B **55**, p. 7859–7863 (1997).

[116] A. S. Foster and A. L. Shluger, *Spin-contrast in non-contact SFM on oxide surfaces: theoretical modelling of NiO(001) surface*, Surf. Sci. **490**, p. 211–219 (2001).

[117] P. M. Hoffmann, A. Oral *et al.*, *Direct measurement of interatomic force gradients using an ultra-low-amplitude atomic force microscope*, Proc. R. Soc. A **457**, p. 1161–1174 (2001).

[118] H. Zabel, *Magnetism of chromium at surfaces, at interfaces and in thin films*, J. Phys. C: Solid State Phys. **11**, p. 9303–9346 (1999).

[119] M. Schmid, M. Pinczolits, W. Hebenstreit and P. Varga, *Segregation of impurities on Cr(100) studied by AES and STM*, Surf. Sci. **377–379**, p. 1023–1027 (1997).

[120] J. Stöhr, A. Scholl *et al.*, *Images of the antiferromagnetic structure of a NiO(100) surface by means of X-ray magnetic linear dichroism spectromicroscopy*, Phys. Rev. Lett. **83**, p. 1862–1865 (1999).

[121] D. Spanke, V. Solinus *et al.*, *Evidence for in-plane antiferromagnetic domains in ultra-thin NiO films*, Phys. Rev. B **58**, p. 5201–5204 (1998).

[122] F. U. Hillebrecht, H. Ohldag *et al.*, *Magnetic moments at the surface of antiferro-magnetic NiO(100)*, Phys. Rev. Lett. **86**, p. 3419–3422 (2001).

[123] V. E. Henrich and P. A. Cox, **The Surface Science of Metal Oxides** (Cambridge University Press, Cambridge, 1994).

[124] A. I. Livshits, A. L. Shluger, A. L. Rohl and A. S. Foster, *Model of noncontact scanning force microscopy on ionic surfaces*, Phys. Rev. B **59**, p. 2436–2448 (1999).

[125] S. H. Ke, T. Uda *et al.*, *First-principles investigation of tip-suface interaction on a GaAs(110) surface: Implications for atomic force and scanning tunneling microscopies*, Phys. Rev. B **60**, p. 11 631–11 644 (1999).

[126] T. Nagamiya, K. Yosida and R. Kubo, *Antiferromagnetism*, Advances in Physics **4**, p. 1–112 (1955).

[127] V. Mandel, *Twin domains in nickel-oxide type crystals*, J. Cryst. Growth **174**, p. 346–353 (1997).

[128] S. Weichel and P. J. Møller, *Annealing-induced microfaceting of the CoO(100) surface investigated by LEED and STM*, Surf. Sci. **399**, p. 219–224 (1998).

[129] P. J. A. van Schendel, private communication.

Publications

1. M. A. Lantz, H. J. Hug, P. J. A. van Schendel, R. Hoffmann, S. Martin, A. Baratoff, A. Abdurixit, H.-J. Güntherodt and Ch. E. Gerber, *Low temperature scanning force microscopy of the Si(111) 7×7 surface,* Physical Review Letters **84**, 2642-2645 (2000)

2. H. J. Hug, M. A. Lantz, A. Abdurixit, P. J. A. van Schendel, R. Hoffmann, P. Kappenberger and A. Baratoff, *Subatomic Features in Atomic Force Microscopy Images,* Science **291**(5513), 2509 (2001)

3. M. A. Lantz, H. J. Hug, R. Hoffmann, P. J. A. van Schendel, P. Kappenberger, S. Martin, A. Baratoff and H.-J. Güntherodt, *Quantitative Measurement of Short-Range Chemical Bonding Forces,* Science **291**(5513), 2580-2583 (2001)

4. P. J. A. van Schendel, H. J. Hug, R. Hoffmann, S. Martin, P. Kappenberger, M. A. Lantz and H.-J. Güntherodt, *Applications of Tip Calibration in Magnetic Force Microscopy (MFM),* NATO ASI (to be published)

5. R. Hoffmann, M. A. Lantz, H. J. Hug, P. J. A. van Schendel, P. Kappenberger, S. Martin, A. Baratoff and H.-J.Güntherodt, *Atomic resolution imaging and force versus distance measurements on KBr (001) using low temperature scanning force microscopy,* Applied Surface Science **188**, 238-244 (2002)

6. R. Hoffmann, D. E. Bürgler, P. J. A. van Schendel, H. J. Hug, S. Martin and H.-J. Güntherodt, *Perpendicular magnetic domains of a thin Ag/Fe/Ag film observed by magnetic force microscopy at room temperature,* (to be published in Journal of Magnetism and Magnetic Materials)

7. R. Hoffmann, M. A. Lantz, H. J. Hug, P. J. A. van Schendel, P. Kappenberger, S. Martin, A. Baratoff and H.-J.Güntherodt, *Atomic resolution imaging and frequency versus distance measurements on NiO (001) using low temperature scanning force microscopy,* (submitted to Physical Review B)

Curriculum Vitae

17 June 1973	Born in Karlsruhe (Germany), daughter of Sigrid Hoffmann geb. Lörcher and Hans-Jürgen Hoffmann
1979-1983	Elementary school in Karlsruhe (Germany), Mount Kisco (USA) and Mainz (Germany)
1983-1992	Gymnasium "Maria-Ward-Schule" in Mainz (Germany)
1992-1998	Study of Physics at the University of Karlsruhe (Germany) and the "Ecole Nationale Supérieure de Physique de Grenoble" in Grenoble (France)
Feb 1998	M.Sc. thesis "Propriétés magnétiques et structurales des couches minces de FePd" in the group of Dr. Bernard Dieny, Commissariat à l'Energie Atomique, Grenoble (France)
1998-2001	Ph.D. thesis at the University of Basel, Switzerland, in the group of Prof. Dr. Hans-Joachim Güntherodt

Acknowledgements

First of all, I thank Prof. Dr. H.-J. Güntherodt, head of the scanning probe group in Basel, for his continuous interest in my work and for the support he provided me in many ways. I thank Prof. Dr. H. J. Hug, my tutor for the PhD thesis, for teaching me his point of view on scanning force microscopy and on general physics. He is also responsible for building and refining the LTSFM I used for my experiments.
I thank Prof. Dr. E. Meyer for co-refereeing this thesis.
I would like to thank all past and present co-workers in the LTSFM group, whose contributions can be found in all parts of this thesis: P. Kappenberger, Dr. O. Knauff, Dr. M. A. Lantz, Dr. W. Lu, S. Martin, Dr. J. Rychen, Dr. P. J. A. van Schendel, Dr. B. Stiefel and the diploma students S. Egli and I. Schmid.
The following people from outside the Hug group or from outside the institute collaborated with me:
Ag/Fe/Ag sandwiches: Dr. D. Bürgler, Dr. F. Meisinger and Dr. D. Schaller provided the samples.
Quantitative MFM: Dr. J. Greschner provided the ultrasharp tips. I thank V. Barwich for some SEM images.
KBr: Dr. L. Kantorovich and Dr. A. Shluger helped me with using the simulation program developed in their group. I also thank Dr. A. Baratoff, Dr. R. Bennewitz and O. Pfeiffer for discussions about the interpretation of the results.

I would like to thank the following people for critically reading the manuscript: Dr. A. Baratoff, V. Barwich, Dr. R. Bennewitz, A. Bredekamp, Dr. D. Bürgler, Dr. B. Hermann, Prof. Dr. H. J. Hug, Dr. L. Kantorovich, P. Kappenberger, Dr. M. A. Lantz, O. Pfeiffer, Dr. P. J. A. van Schendel.
I would like to thank the members of the electronic workshop, of the technology group and of the mechanical workshop for their help. Especially, I would like to thank W. Roth and D. Michel for providing liquid helium and nitrogen even late in the evening.
I thank my parents, my sister Anne Hoffmann and Simon Woods for their continuous support. Especially, I would like to thank Matthias Vogel for his continuous motivation and active support.

Zusammenfassung

Magnetische und interatomare Kräfte wurden mit Tieftemperaturrasterkraftmikroskopie im dynamischen Modus untersucht, bei dem die Spitze mit einer konstanten Amplitude über der Probe oszilliert wird, und die Resonanzfrequenz des Federbalkens aufgezeichnet wird. Zunächst wurden magnetische Domänen in ultradünnen Eisenfilmen bei Zimmertemperatur untersucht. Diese nur 3.5 Atomlagen dicken Filme zeigen einen dickenabhängigen Reorientierungsübergang, wodurch die Orientierung der Magnetisierung sich von senkrecht bei dünnen Schichtdicken zu parallel zum Film bei dicken Schichtdicken ändert. Im Bereich der senkrechten Magnetisierung konnten magnetische Domänen abgebildet werden, obwohl das Koerzitivfeld der Probe kleiner war als 1 mT, das heisst in der gleichen Grössenordnung wie das von der Spitze ausgesandte Feld. Wie erwartet, variiert die Domänengrösse stark mit der Schichtdicke zwischen Werten von 580 nm und 190 nm. Die magnetische Oberflächenanisotropie K_S, die aus der Abhängigkeit der Domänengrösse von der Schichtdicke gewonnen wurde, stimmt gut mit Literaturdaten überein.

Für diese Untersuchung war es entscheidend, eine magnetische Spitze herzustellen, die ein schwaches magnetisches Feld aussendet: Im Idealfall sollte das Magnetfeld, das von der Spitze ausgesendet wird, kleiner sein als das Koerzitivfeld der Probe. Um die Magnetfelder, die von magnetischen Spitzen ausgesandt werden, und ihre Auflösung zu untersuchen, wurde eine quantitative Analyse ausgeführt. Diese Analyse basiert auf der Kalibration der magnetischen Spitze auf einer bekannten Testprobe mit senkrechter Anisotropie. Magnetische Spitzen, die mit unterschiedlich dicken Eisenfilmen beschichtet waren, wurden untersucht, und es wurde gezeigt, dass die Spitzen gute Abbildungseigenschaften oberhalb einer nominalen Schichtdicke des Eisens von 1.3 nm aufwiesen. Das von diesen Spitzen ausgesandte Feld nimmt mit zunehmender Eisenschichtdicke zu. Mit Nickel beschichtete Spitzen besitzen hingegen keine guten Abbildungseigenschaften. Die Auflösung der magnetischen Spitzen kann verbessert werden, indem ultrascharfe Spitzen statt Standardspitzen verwendet werden. Ultrascharfe Spitzen können gut mit Modellen von magnetischen Punktladungen beschrieben werden, im Gegensatz zu Standardspitzen, die nur mit Modellen von ausgedehnten Ladungen gut beschrieben werden können.

Interatomare Kräfte wurden untersucht auf einkristallinen KBr und NiO (001) Oberflächen. Die ionische KBr (001) Oberfläche ist ein Modellsystem für die Untersuchung von Wechselwirkungen zwischen Spitze und Probe, weil atomare Auflösung leicht erreicht werden kann und weil Rechnungen mit einem Schalenmodell durchgeführt werden können. Ein Programm zur Durchführung dieser Rechnungen wurde von L. Kantorovich, University College, London, entwickelt und zur Verfügung gestellt. Nachdem Bilder mit atomarer Auflösung aufgenommen wurden, wurde die Resonanzverstimmung des Federbalkens in Abhängigkeit vom Spitzen-Proben-Abstand über bestimmten Stellen der Oberfläche gemessen. Aus diesen Daten wurden Kraft-Distanz Kurven gewonnen. Die Gesamtwechselwirkung zwischen Spitze und Probe lässt sich als eine Summe aus langreichweitigen und kurzreichweitigen Komponenten ausgedrücken. Die langreichweitige

Komponente wird gut durch eine van-der-Waals Kraft zwischen einem Konus mit abschliessender Kugel und einer flachen Oberfläche beschrieben. Die kurzreichweitige Komponente wurde mit atomistischen Simulationen berechnet. Der Maximalwert der berechneten anziehenden Kraft und ihre Zerfallslänge stimmen mit unseren Experimenten gut überein. Die Korrugation wird in unseren Berechnungen überschätzt: eine Korrugation von nur 0.025 nm wurde gemessen, während unsere Berechnungen eine Korrugation von 0.2 nm voraussagen. Eine mögliche Erklärung hierfür ist, dass das atomistische Modell des Spitzenendes möglicherweise nicht mit der im Experiment verwendeten Spitze übereinstimmt, zum Beispiel weil im Experiment weitere Atome mit der Oberfläche wechselwirken könnten. Die experimentelle Beobachtung eines Defektes zeigt aber, dass Wechselwirkungen mit mehreren Atomen bei der Distanz, die während der Aufnahme der Bilder zwischen Spitze und Probe herrschte, vernachlässigbar ist. Bei geringeren Abständen zwischen Spitze und Probe können diese Wechselwirkungen jedoch erheblich werden. Schliesslich wurde die durch Wasser verunreinigte KBr (001) Oberfläche untersucht. Es wurden Bilder mit atomarer Auflösung einer geordneten Phase aufgenommen.
NiO ist ein antiferromagnetischer Isolator, der von mehreren Gruppen untersucht wurde, um kurzreichweitige magnetische Austauschkräfte zu messen. Die NiO (001) Oberfläche wurde mit atomarer Auflösung mit einer nichtmagnetischen Spitze abgebildet. Die Oberflächenkräfte wurden über spezifischen Stellen der Oberfläche mit Hilfe von Frequenz-Distanz-Kurven untersucht. Die langreichweitigen Kräfte werden mit einer kapazitiven Kraft im Abstandsbereich zwischen 0.5 und 20 nm gut beschrieben. Diese kapazitiven Kräfte entstehen durch elektrische Ladungen, die auf der isolierenden Oberfläche lokalisiert sind. Wechselwirkungen zwischen mehreren Atomen der Spitze und/ oder der Oberfläche spielen bei geringen Abständen zwischen Spitze und Probe eine Rolle in Übereinstimmung mit Simulationen und verursachen eine Oszillation in der Frequenz-Distanz-Kurve. Wie Simulationen zeigen, sind solche Wechselwirkungen zwischen mehreren Atomen möglich infolge der starken Relaxationseffekte. Diese Relaxationseffekte verhindern leider Abbildungen der Oberfläche bei kleinem Spitzen-Proben-Abstand, bei denen erwartet wird, dass kurzreichweitige magnetische Wechselwirkungen messbar werden. Ausserdem steigt die pro Oszillationszyklus dissipierte Energie scharf an bei dem Spitzen-Proben-Abstand, bei dem die Wechselwirkung zwischen mehreren Atomen auf der Spitze und auf der Probe einsetzen. Das ist ein Anzeichen dafür, dass die induzierten Bewegungen der Spitzen- und Probenatome bei diesem Spitzen-Proben-Abstand hysteretisch werden. Die Beobachtung eines Punktdefekts auf der NiO Oberfläche zeigt, dass die Spitze atomar scharf ist bei den Spitzen-Proben-Abständen, bei denen stabil abgebildet werden kann.

Abstract

Magnetic and interatomic forces have been investigated using low temperature scanning force microscopy (LTSFM) in a dynamic mode where the probing tip at the end of a microlever is oscillated with a constant amplitude above the sample and the resonance frequency of the lever is tracked. First, magnetic domains in ultrathin Fe films sandwiched between Ag layers have been investigated at room temperature. These films only 3.5 atomic layers thick show a thickness dependent reorientation transition whereby the orientation of the magnetization changes from perpendicular at small thicknesses to parallel to the film at large film thicknesses. In the perpendicular regime, magnetic domains could be imaged although the coercive field of the sample was less than 1 mT, i.e. of the same order of magnitude as the field generated by the magnetic tip. As expected, the domain size varies strongly with film thickness, namely between 580 nm and 190 nm. The value of the magnetic surface anisotropy parameter K_S obtained from the domain size variation agrees well with literature values.

For this study, it was essential to prepare a magnetic tip that generates a weak magnetic field: Ideally the magnetic field generated by the tip should be smaller than the coercive field of the sample. In order to investigate the magnetic fields generated by magnetic tips and in order to analyse their resolution, a quantitative analysis has been carried out. This analysis relies on the calibration of the magnetic tip using a known test sample with perpendicular anisotropy. Magnetic tips coated with different film thicknesses of Fe were studied, showing that above a nominal Fe thickness of 1.3 nm the tip has good imaging properties and that the field generated by the tip increases with growing Fe thickness. Ni coated tips do not have good imaging properties. The resolution of magnetic tips can be improved using ultrasharp tips instead of standard ones. Ultrasharp tips are well described using a monopole model, in contrast to standard tips, where an extended charge model is necessary.

Interatomic forces have been studied on single crystalline KBr and NiO (001) surfaces. The ionic crystalline KBr (001) surface is a model system for the study of interaction forces, as atomic resolution images are easily obtained and calculations can be performed using a shell-model and a dedicated program developed by L. Kantorovich, University College, London. After obtaining atomic resolution, the frequency shift was measured as a function of tip-sample distance above characteristic surface sites. The obtained data was converted to force versus distance data. The total interaction force is expressed as a sum of long-range and short-range force components. The long-range force is well described by a van-der-Waals force between a conical tip with spherical cap and a flat surface. The short-range interaction was computed using atomistic simulations. The maximum value of the calculated attractive force and its decay length are in good agreement with our experiments. The corrugation is overestimated in the calculations: a corrugation of only 0.025 nm was measured, while the calculations predict a corrugation of 0.2 nm. One possible reason is that the atomistic tip apex model assumed for the calculations may not represent the

experimental tip well, for example due to multiatom interactions. The experimental observation of an atomic scale defect shows that multiatom interactions are negligible at the mean imaging distance, but at closer tip to sample distances, these interactions can become important. Finally the water contaminated KBr (001) surface has been studied. Atomic resolution images of an ordered phase have been obtained.

NiO is an antiferromagnetic insulator studied by several SFM groups in order to measure short-range magnetic exchange interactions. Atomic resolution was obtained on the NiO (001) surface using a non-magnetic tip. The surface forces have been studied with site-specific frequency versus distance measurements. The long-range force-distance data are well modelled with a capacitive force in the distance range of 0.5 to 20 nm. These capacitive forces arise from electric charges localized on the insulating surface. Multiatom interactions become important at close tip-sample distances in agreement with calculations and lead to an oscillation in the frequency versus distance. As shown by calculations, such multiatom interactions are possible because of large relaxation effects. These relaxation effects prevent unfortunately imaging at close tip-sample distances, where short-range magnetic interactions are expected to be of a measurable magnitude. Furthermore, the dissipated energy per oscillation cycle increases sharply at the tip-sample distance where the interaction between several atoms on the tip and on the surface becomes important. This is an indication that the induced displacements of tip and surface atoms becomes hysteretic at this tip-sample distance. The observation of a point defect on the NiO surface shows that the tip is atomically sharp at the tip-sample distances where stable images could be obtained.